UNIVERSITY OF CAMBRIDGE

Department of Engineering

FOLDING OF BISTABLE COMPOSITE TAPE-SPRINGS

CUED/D-STRUCT/TR.252

January 2019

Bing Wang, Keith A Seffen, Simon D Guest

ISSN: 0309-7447

Trumpington Street, Cambridge, CB2 1PZ, UK

Abstract

Bistable composite tape-spring technologies have great potential in application to aircraft landing gears, in order to reduce weight, complexity and maintenance compared to the conventional lock-link assemblies. To investigate their implementation, the first area of interest is the ‘‘ploy’’ region, which corresponds to the transitional state between the folded and the extended configurations. We devise a simple ‘‘free’’ bending system with minimal constraints to study the folding nature of tape-spring structures in general. A finite element (FE) model is also established and calibrated using experimental data; a theoretical model is developed to provide further insights. The typical folding process consists of linear bending, torsional buckling, localisation and then folding; the shape of the central fold is developable; the ploy region is dominated by axial strains and transverse curvature changes. Here, we achieve a good agreement between experiments, simulation and theoretical analysis.

ACKNOWLEDGEMENTS

The authors would like to thank the financial support from Innovate UK on project ‘‘Large Landing Gear of the Future: Bistable Composite Technologies’’ (Grant No. 113077, RG82506), in partnership with SAFRAN Landing Systems Ltd., UK. Technical supports from the Structures Laboratory, Department of Engineering are also gratefully acknowledged.

LIST OF CONTENTS

LIST OF FIGURES

LIST OF TABLES

ABBREVIATIONS

CFRP	Carbon fibre reinforced polymer
CLT	Classic lamination theory
CTS	Composite tape-spring
ESB	Equal-sense bending
FE	Finite element
GF	Glass fibre
H-S	Hashin-Shtrikman bounds
ITS	Isotropic tape-spring
LDPE	Low density polyethylene
OSB	Opposite-sense bending
PP	Polypropylene
SA	Subtended angle
STEM	Storable tubular extendible member
UD	Unidirectional
V-R	Voigt-Reuss bounds

SYMBOLS

b	Width of a tape-spring, mm
c	Curvature
d	Displacement, mm
k	Decay parameter
t	Thickness, mm
v	Poisson's ratio
x	Longitudinal direction
y	Transverse direction
z	Thickness direction
D	Flexural rigidity, $Et^3/12(1-v^2/\beta)$
E	Young's modulus, GPa
F	Force, N
G	Shear modulus, GPa
K	Bulk modulus, GPa
L	Length, mm
M_x	Longitudinal bending moment, N·mm
M_y	Transverse bending moment, N·mm
M_{xy}	Twisting moment, N·mm
Q_{ij}	Elements of reduced stiffness matrix
R	Radius, mm
R_Ω	Strain gauge resistance
S_{ij}	Elements of the compliance matrix
U	Total strain energy
U_B	Bending strain energy density
U_S	Stretching strain energy density
V_f	Fibre volume fraction
W	Width, mm
α	Orthotropic torsional rigidity
β	Modulus ratio, E_y/E_x

θ	Fibre angle, °
ξ	Subtended angle, °
δ	Displacement, mm
σ	Stress, MPa
ϵ	In-plane strain
κ_0	Initial curvature
κ_x	Longitudinal curvature
κ_y	Transverse curvature
κ_{xy}	Twisting curvature
χ_x	Change in longitudinal curvature
χ_y	Change in transverse curvature
χ_{xy}	Change in twisting curvature
2φ	Subtended angle of the circular folded region
2ψ	Folded angle of a tape-spring

Section 1

INTRODUCTION

1.1 INTRODUCTION

The use of composite laminated structures in aerospace engineering can reduce weight, complexity, improve aerodynamic efficiency and shape adaptivity [1] because of their high strength-to-weight ratio and stiffness-to-weight ratio [2]. Morphing composite structures, in particular, are proposed extensively for multistable and energy harvesting applications [3]. Bistable composite structures are a proven technology, and are enabled by means of thermal residual stress [5], geometrical curvature effects [6], piezoelectric actuation [7], and prestress induced from either elasticity [8] or viscoelasticity [9]. Their potential applications include aircraft aerofoils [4,5], automobile structures [6], and wind turbine blades [1], *etc*.

A bistable composite ‘‘tape-spring’’ is a thin-walled, open slit composite tube, with stable extended and coiled configurations. This inherent behaviour has similarities with the lock-stay or side-stay folding assemblies of an aircraft landing gear: these extend and retract with the gear but remain in a fixed position when the gear is stowed in the bay or locked in the ‘‘down’’ position. Using a composite material reduces weight, complexity and maintenance compared to conventional lock link assemblies [7].

We are concerned with the manufacture and folding response of composite tape-springs, and we use ordinary isotropic springs for guidance in extending well-known methodologies. The bending response is complex and nonlinear, and controlled by material orthotropy and geometrical nonlinearity. Analysis becomes increasingly detailed and complex: linear elasticity accords first material synthesis and the orthotropic specification; moderate displacements enable us to think about the torsional buckling that is observed during folding and how to formulate the resulting folded shape; and large displacement folding is served by simple inextensible shell models of uniform curvature changes. From a design perspective, we want to quantify the stowed shape of the tapes, the structural limitations of folding, and the influence of material orthotropy.

This section is a prelude to the report. Section 1.2 summarises the research progress in bistable composite technologies, and the development of composite tape-springs. Section 1.3 gives the

aim and objectives of this research, and Section 1.4 provides an overview of the sections which follow in the report.

1.2 LITERATURE REVIEW

1.2.1 Bistable composite technology

Bistable composite laminate structures can snap from one stable configuration to the other under external loads. To date, it has been reported that their bistability can be produced by means of thermal residual stress [8], piezoelectric actuation [9], elastic prestress [10], viscoelastic prestress [11] and curvature (geometry) effects [12]: Figure 1-1 shows some examples.

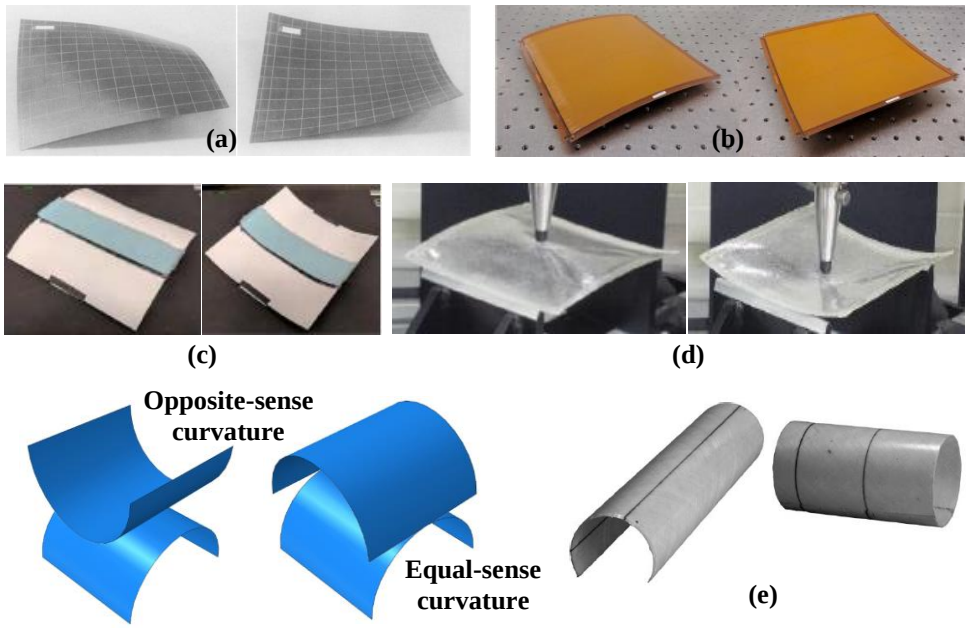

Figure 1-1 Examples of bistable composite structures using (a) thermal residual stress [13], (b) piezoelectric actuation [9], (c) elastic prestress [14], (d) viscoelastic prestress [11], (e) curvature effects [12].

Bistable structures can be split into two categories (Figure 1-1): ‘‘opposite-sense’’ bistable shells have two stable cylindrical shapes, where each centre of cylindrical curvature lies on opposite sides of the structure above and below; while ‘‘equal-sense’’ shells have stable

curvatures on the same side. In application to aircraft landing gear, an equal-sense tape is utilised because it can be folded reliably without damage. We call this our bistable composite tape-spring (CTS).

1.2.2 Bistable composite tape-spring

The bistable CTS was invented by Daton-Lovett in 1996 [15]. An anti-symmetric composite lay-up was selected to eliminate coupling between bending and twisting for a less complex response. To date, there have been various approaches in terms of experimental, analytical and simulation models to predict and characterise their bistability and deployment behaviour.

Iqbal and Pellegrino [16] developed a simple analytical model to calculate the strain energy of the CTS in terms of the transverse and longitudinal curvatures, which was able to capture the main features of the coiling process. Based on the assumption that the longitudinal deformation is uniform, Galletly and Guest further developed a beam model [17], and later a shell model [18], to predict the equilibrium configurations of the CTS structures with varying transverse shapes. The validation of the analytical model was performed for different materials including antisymmetric laminate, symmetric laminae and isotropic tapes, and results correlated fairly well with the published data. Guest and Pellegrino [12] simplified the analytical model with inextensional deformations, and successfully predicted the stability of the cylindrical shell for different constitutive relations.

In folding of CTS structures, Yee *et al.* [19] investigated the moment-rotation relationship of carbon-fibre reinforced polymeric (CFRP) tape-springs. Similar to isotropic (metallic) tape-springs [20], the behaviour is linear-elastic for small rotations before buckling into a folded configuration, which has a constant moment under large rotations in both equal- and opposite-sense bending; a finite element analysis was established to study the maximum strain values in bending. Later they studied the folding of a self-deploying composite tube hinge made by cutting three parallel slots in a thin-walled cylindrical tube [21]. The strains before failure in tension, compression and bending of the hinge were characterised for one-ply and two-ply woven composites using large-displacement buckling tests, analytical and FE models [22]. Mallikarachchi and Pellegrino [23] then investigated the folding and deployment of a composite tube hinge with two slots.

In addition to using a CTS as a single structure or a tube hinge design, Murphey *et al.* [24] proposed several CTS concepts to construct deployable booms, for use as gravity gradient stabilisation devices, optical and other sensing devices. Xiong *et al.* [25] studied the experimental deployment of a deployable composite structure of three tape-springs, whereas Costantine *et al.* [26] developed a deployable dipole antenna structure using CTS components with embedded copper alloy conductors for CubeSat applications; Wu and Viquerat [27] examined the natural frequency of a deployable solar array of bistable reeled composite slit tubes, and Mao *et al.* [28] constructed a self-deployable boom assembly of four 1 m long bistable CTS components.

Deployable structures are often stowed for some time during launch and then subjected to multiple thermal cycles in orbit [29]. In recent years, there have been growing demands for understanding the natural viscoelastic behaviour of the CTS structure, in order to precisely control the deployment and stowage of the associated deployable structures. This can be achieved experimentally (by creep or stress relaxation tests) or by characterising the viscoelastic constitutive relations of the viscoelastic solids, usually via a Prony series expressing the matrix material, which is integrated into the time-dependent relaxation modulus equations [29–33].

For example, Kwok and Pellegrino [29] investigated the shape recovery behaviour of a simple beam and a tape-spring structure made of pure LDPE. They characterised the reaction force, deformed shapes and curvature through experiments, theoretical modelling, and simulations. Birnkmeyer *et al.* [30] studied the effects of long-term stowage on the deployment of bistable tape-springs. Their analytical model showed that the deployment time increased predictably with stowage time and temperature in line with experimental observations. Kwok and Pellegrino [34] also developed a viscoelastic model for a single-ply CTS structure, in order to investigate the effects of stowage periods on its deployment; the constitutive behaviour of materials were homogenised by considering the linear elastic fibres within a linear viscoelastic matrix. Khan *et al.* [32] examined the effects of matrix viscoelasticity on energy dissipation of a three-layer CFRP composite during the stowage state. Borowski *et al.* [33] built an experimental setup to study the influences of stress relaxation during stowage on the deployment dynamics of a polymeric CTS structure; a finite element model with a user-defined material subroutine was created, and showed good agreement with experiments.

CTS structures can also be manufactured to be neutrally stable, in order to avoid spontaneous deployment upon releasing the constraints of transportation, which cause extra vibration and instability. Murphey and Pellegrino [35] fabricated a neutrally stable tape-spring by manipulating the prestressed plies and stacking sequences, which had non-zero strain energy in both the extended and coiled configurations. Schultz *et al.* [36] used a low stiffness epoxy resin to produce a stress-free neutrally stable tape-spring structure whose deployment could be controlled at any point thermally using a shape memory alloy. Table 1-1 summarises previous research in chronological order on CTS and related structures.

Table 1-1 Summary of research on CTS and related structures. UD stands for the ''unidirectional''; *R* is the natural transverse radius; *L* is the axial length; *t* is the thickness; SA is the ''subtended angle''.

Year	Investigator	Materials	Geometry	Main content
1996	Daton-Lovett [15]	UD glass fibre reinforced polypropylene	--	Invented and patented the bistable composite tape-spring structure.
2000	Iqbal and Pellegrino [16]	UD glass fibre reinforced polypropylene	*R*: 25 mm *L*: 90 mm *t*: 1.1 mm SA: 180˚	Developed an FE model to include twist to simulate coiling. Main features captured by the model with limited accuracy.
2004	Murphey and Pellegrino [35]	UD graphite T300 fibre reinforced epoxy prepreg	*R*: 32 mm *t*: 0.13 mm	Neutrally stable tape spring fabricated by manipulating material orthotropy and prestress. Analytical model able to predict neutral stability for prestressed laminates.
2004	Galletly and Guest [17]	Analytical model		Developed a beam model to predict the equilibrium shapes of a composite slit tube of any longitudinal shape with the cross-section as a circular arc of varying radius.
2004	Galletly and Guest [18]	Analytical model		Developed a shell model to be able to predict equilibrium shapes of a composite slit tube with any cross-sectional shape.
2004	Yee *et al.* [19]	Plain-weave T300 carbon fibre reinforced epoxy resin	*R*: 15-20 mm *L*: 150 mm *t*: 0.13-0.26 mm SA: variable	Investigated the moment-rotation relation of a carbon fibre reinforced plastic tape-springs.
2005	Yee and Pellegrino [21]	Woven T300 carbon fibre reinforced epoxy resin	Tube hinge with three slots	Performed large-displacement buckling tests for woven composite structures. The failure strains in tension, compression and bending characterised for one-ply and two-ply woven composites.
2005	Yee and Pellegrino [22]	Woven T300 carbon fibre reinforced epoxy resin	Tube hinge *R*: 6.5 mm *L*: 50 mm *t*: 0.27-0.47 mm SA: 70˚	Folding of one-ply and two-ply composite tube hinges made by cutting three parallel slots in a thin-walled cylindrical tube. Analytical and FE models developed.
2006	Guest and Pellegrino [12]	Analytical model		Developed an inextensional model to predict the stability of the cylindrical shells based on minimal strain energy.
2008	Schultz *et al.* [36]	Plain-weave T300 carbon	*R*: 32 mm	Neutrally stable tape-spring fabricated through selection of fibre angles,

		fabric reinforced epoxy resin		manufacturing tool, and matrix material. Deployment could be started and stopped at any point.
2010	Murphey *et al.* [24]	Glass or carbon fabric reinforced epoxy resin	*R*: 6.35 mm *t*: 0.127 mm SA: 180˚	Utilised CTS components to construct deployable booms for spacecraft.
2010	Kwok and Pellegrino [29]	LDPE	*R*: 38 mm *L*: 340 mm *t*: 0.7 mm *W*: 75 mm	Investigated the shape recovery behaviour of a simple beam and a tape-spring structure made of isotropic LDPE. Characterised the reaction force, deformed shapes and curvature through experiments, theoretical model, as well as simulations.
2011	Mallikarachchi and Pellegrino [23]	Plain-weave T300 carbon fabric reinforced epoxy resin	Composite tube hinge with two slots *R*=38 mm *L*=140 mm *t*: 0.2 mm *W*=25 mm	Investigated the folding and deployment of a composite tube hinge with two slots. Moment-rotation profile studied experimentally, and numerically during deployment.
2011	Xiong *et al.* [25]	Plain-weave carbon and glass fabric reinforced epoxy resin	*R*: 20 mm *L*: 120 mm *t*: 0.48-0.64 mm SA: 70-90˚	Experimentally studied a deployable composite structure with three tape-springs. Maximum strain values during deployment characterised using strain gauges.
2012	Costantine *et al.* [26]	Glass fiber reinforced epoxy with embedded copper alloy	*R*: 6.5 mm *L*: 560 mm SA: 180˚	Deployable dipole antenna structure was designed, simulated and experimentally investigated for CubeSat applications.
2016	Birnkmeyer *et al.* [30]	UD T800 carbon fibre prepreg	*R*: 16.6 mm *L*: 1253 mm *t*: 0.18 mm SA: 132˚	Studied the effects of long-term stowage on the deployment of bistable tape-springs. Analytical model showed good agreement with experiments. Deployment failed after stowage at 100˚C for 3 hours.
2017	Wu and Viquerat [27]	Braided carbon fibre reinforced epoxy resin	*R*: 38 mm *L*: 5100 mm *t*: 0.368 mm SA: 345˚	Developed a deployable solar array with bistable reeled composite slit tubes. Examined the natural frequency and coiled diameter of the solar array with respect to braided angle (15-75˚).
2017	Kwok and Pellegrino [34]	Plain-weave T300-1k carbon fibre reinforced epoxy resin	*R*: 19 mm *L*: 596 mm *t*: 0.125 mm SA: 180˚	Viscoelastic model developed to predict the deployment of composite thin shells stowed for an arbitrarily long period of time. Good agreement with experimental results.
2017	Khan *et al.* [32]	Plain weave and UD carbon fabric reinforced epoxy resin	*R*: 41.32 *L*: 152.4 mm *t*: 0.65 mm SA: 35.8˚	Effects of matrix viscoelasticity on energy dissipation of a three-layer CFRP composite examined during the stowage state. Time-dependent implicit finite element model simulated the viscoelastic behaviour of the orthotropic type laminate.
2017	Mao *et al.* [28]	Plain-weave glass fabric reinforced epoxy resin	*R*: 7.2 mm *L*: 1000 mm *t*: 0.4 mm SA: 180˚	Deployable boom assembly of four 1 m long bistable GF tape springs investigated for deployment dynamics and reliability after long-term stowage. Analytical model developed.
2018	Borowski *et al.* [33]	Plain-weave carbon fabric reinforced epoxy resin prepreg	*R*: 50.8 mm *L*: 305 mm *t*: 0.48 mm SA: 29˚	Developed an experimental setup and FE model to study the effects of stress relaxation during stowage of a CTS structure. Prony series of the matrix material determined through stress relaxation tests.

1.3 AIMS AND OBJECTIVES

The aim of this research is to understand the ploy region of a bistable composite tape-spring structure and its effects on folding. These objectives are:

(i) Experimental investigation into the folding nature of tape-spring structures, for both isotropic and orthotropic composite materials, in order to define differences.

(ii) Finite element analysis of the folding behaviour, in order to complement the experimental study and to provide further insight into folding.

(iii) Mathematical analysis to characterise the folding and ploy shape of tape-springs.

1.4 OVERVIEW OF REPORT

This section gives an overview of the main content in each section, to provide a quick index for specific interest. To facilitate reading, each section is ‘‘self-contained’’.

Section 2 – Composite manufacture and characterisation

Section 2 provides detailed information on the manufacturing and characterisation of the CTS samples: a theoretical background from micromechanics to macromechanics of composites is also covered. The best layup within the framework of glass fabric reinforced polypropylene composite is also selected for further investigation; its mechanical properties are experimentally characterised using embedded strain gauges. These data provide a basis for the finite element analysis.

Section 3 – Folding of tape-springs

Section 3 evaluates the folding nature of tape-springs made from both isotropic and orthotropic materials, which exhibit torsional buckling and unstable behaviour. A finite element model is also constructed to study the folding behaviour, and the effects from various factors. The model

provides good agreement with experimental results and implies further insight into the folding nature.

Section 4 – Structural behaviour

Section 4 develops the theoretical analysis for the folding observations presented in Section 3. The theoretical model is able to predict the critical buckling force for isotropic tapes under small rotations. It can also predict the minimum force for isotropic tapes under large displacements; limited effectiveness is however obtained for composite tapes with a large subtended angle.

Section 5 – Shape of ploy region

Section 5 characterises the static folded shape. We highlight the more interesting shape parameters of our folded tapes, such as the exponential decay and ploy length in the ploy region. These govern the ability of the tape to be folded and stowed, as well as provide essential guidance to the design and implementation of bistable composite tubes.

Section 2

COMPOSITE MANUFACTURE AND CHARACTERISATION

2.1 INTRODUCTION

For decades, tape-springs made from metallic materials have been used as deployable structures in space due to their compact stowed volume and good structural characteristics when deployed [37]. Metallic tape springs are only stable in the deployed state, and a robust containment solution is required to keep them locked; moreover, during deployment, a control scheme is sometimes necessary to prevent dynamic ‘‘blooming’’ where the tape unravels internally and prematurely [24]. These aspects pose issues on the overall mass budget, reliability and complexity for such mechanisms.

Bistable CTS structures provide an alternative solution. They are stable in both extended and coiled configurations, which can lead to weight savings, less control complexity, and hence increase their reliability [38]. The mechanism of its bistability is well-understood; see for example [12]: other previous studies focus on their deployment behaviour as a single structure or integrated within other deployable structures [25,28,30,39], as well as modelling their natural viscoelastic constitutive behaviour [32,34,40]. These have been reviewed in Section 1.2.2.

In this section, we provide the details and experiences learned, in order to manufacture the CTS samples: previous research on bistable composite structures by the Advanced Structures Group in Cambridge provide a basis [12]. To further understand the folding and shape-changing behaviour in the ploy region of CTS, the glass fibre (GF) plain-weave woven reinforced polypropylene (PP) composite was selected as the material system for investigation. To facilitate a technical understanding, theoretical background topics from micromechanics to macromechanics of composites are covered. The fundamentals of using strain gauges are also explained. Within the framework of GF/PP composite systems, various raw GF fabrics, PP sheets and composite layups are used to produce the CTS samples. From many trials, they imply useful guidelines and experiences for their manufacture. The composite layup with the best performance is selected for further investigation. Subsequently, its mechanical properties are characterised with embedded strain gauges. The cross-sectional structure of the composite is also evaluated through optical microscopy to provide a better understanding of its mechanical performance.

2.2 THEORATICAL BACKGROUND

2.2.1 Micromechanics of composites

Various micromechanical models are used to determine the mechanical properties of composite materials [41–45]. The most well-known is the classical rule-of-mixtures, also known as the Voigt-Reuss (V-R) bounds. Although the rule-of-mixtures predict the longitudinal modulus of UD laminates well enough, it is not suitable for the transverse modulus, which is based on the iso-stress assumption (Section 2.2.1.1). This is unrealistic because the phase with the higher elastic modulus usually undergoes higher stress, leading to debonding from the fibres [46]. Another widely accepted model is the Hashin-Shtrikman (H-S) bounds, which gives a good estimation when the ratio of modulus values between different phases is not too large.

2.2.1.1 Voigt-Reuss bounds

The V-R bounds use elasticity theory [47] to predict the mechanical properties of the unidirectional (UD) laminates, considering the matrix and the fibres to be both isotropic. The Voigt upper bound assumes the fibre reinforcement and matrix are arranged in parallel and subject to the same stress; this is known as the iso-strain rule of mixtures. In the Reuss lower bound, the applied stress is perpendicular to the fibres and the constituents of the composite undergo the same stress; this is known as the iso-stress rule of mixtures. They can be expressed by the following:

$$E_{\mathrm{VR}}^{1} = E_{xf}V_{\mathrm{f}} + E_{\mathrm{m}}(1 - V_{\mathrm{f}}) \tag{2-1}$$

$$E_{\mathrm{VR}}^{2} = \frac{E_{\mathrm{m}}E_{yf}}{E_{yf}(1 - V_{\mathrm{f}}) + V_{\mathrm{f}}E_{\mathrm{m}}} \tag{2-2}$$

$$G_{xy} = \frac{G_{\mathrm{m}}G_{\mathrm{f}}}{G_{\mathrm{f}}(1 - V_{\mathrm{f}}) + V_{\mathrm{f}}G_{\mathrm{m}}} \tag{2-3}$$

$$G_{\mathrm{f}} = \frac{E_{xf}}{2(1 + \upsilon_{\mathrm{f}})} \tag{2-4}$$

$$G_{\mathrm{m}} = \frac{E_{\mathrm{m}}}{2(1 + \upsilon_{\mathrm{m}})} \tag{2-5}$$

$$\upsilon_{xy} = \upsilon_{\mathrm{f}}V_{\mathrm{f}} + \upsilon_{\mathrm{m}}(1 - V_{\mathrm{f}}) \tag{2-6}$$

where E_{xf} and E_{yf} are the Young's moduli of fibres in longitudinal 'x' and transverse 'y' directions, respectively; V_{f} is the fibre volume fraction; G_{f} is the shear modulus of the fibre.

2.2.1.2 Hashin-Shtrikman bounds

The H-S bounds are based on minimum potential energy and minimum complementary energy. The upper and lower bounds of the bulk modulus *K* and shear modulus *G* follow [41,44]:

$$K_{\mathrm{HS}}^{x} = K_{\mathrm{f}} + \frac{V_{\mathrm{m}}}{\frac{1}{(K_{\mathrm{m}} - K_{\mathrm{f}})} + \frac{3V_{\mathrm{f}}}{(3K_{\mathrm{f}} + 4G_{\mathrm{f}})}} \tag{2-7}$$

$$K_{\mathrm{HS}}^{y} = K_{\mathrm{m}} + \frac{V_{\mathrm{f}}}{\frac{1}{(K_{\mathrm{f}} - K_{\mathrm{m}})} + \frac{3V_{m}}{(3K_{\mathrm{m}} + 4G_{\mathrm{m}})}} \tag{2-8}$$

$$G_{\mathrm{HS}}^{x} = G_{\mathrm{f}} + \frac{V_{\mathrm{m}}}{\frac{1}{(G_{\mathrm{m}} - G_{\mathrm{f}})} + \frac{6V_{\mathrm{f}}(K_{\mathrm{f}} + 2G_{\mathrm{f}})}{5G_{\mathrm{f}}(3K_{\mathrm{f}} + 4G_{\mathrm{f}})}} \tag{2-9}$$

$$G_{\mathrm{HS}}^{y} = G_{\mathrm{m}} + \frac{V_{\mathrm{f}}}{\frac{1}{(G_{\mathrm{f}} - G_{\mathrm{m}})} + \frac{6V_{\mathrm{m}}(K_{m} + 2G_{\mathrm{m}})}{5G_{\mathrm{m}}(3K_{\mathrm{m}} + 4G_{\mathrm{m}})}} \tag{2-10}$$

The H-S upper and lower bounds for the effective modulus lie within the V-R bounds within a narrower range, and:

$$E_{\mathrm{HS}}^{x} = E_{\mathrm{f}}\frac{5E_{\mathrm{m}} + 3V_{\mathrm{f}}(E_{\mathrm{f}} - E_{\mathrm{m}})}{5E_{\mathrm{f}} - 2V_{\mathrm{f}}(E_{\mathrm{f}} - E_{\mathrm{m}})} \tag{2-11}$$

$$E_{\mathrm{HS}}^{y} = E_{\mathrm{m}}\frac{3E_{\mathrm{m}} + 2E_{\mathrm{f}} + 3V_{\mathrm{f}}(E_{\mathrm{f}} - E_{\mathrm{m}})}{3E_{\mathrm{m}} + 2E_{\mathrm{f}} - 2V_{\mathrm{f}}(E_{\mathrm{f}} - E_{\mathrm{m}})} \tag{2-12}$$

$$G_{\mathrm{HS}}^{xy} = G_{m}\frac{G_{\mathrm{m}}(1 - V_{f}) + G_{\mathrm{f}}(1 + V_{f})}{G_{\mathrm{m}}(1 + V_{f}) + G_{\mathrm{f}}(1 - V_{f})} \tag{2-13}$$

$$v_{\mathrm{HS}}^{xy} = v_{f}V_{\mathrm{f}} + v_{m}(1 - V_{\mathrm{f}}) + \frac{4(v_{f} - v_{m})(\frac{1}{K_{m}} - \frac{1}{K_{f}})(1 - V_{f})V_{f}}{\frac{1 - V_{f}}{K_{f}} + \frac{V_{f}}{K_{m}} + 1/G_{m}} \tag{2-14}$$

where E_{HS}^{x} and E_{HS}^{y} are the H-S upper and lower bounds of the effective modulus, respectively.

2.2.2 Macromechanics of composites

Macromechanics of thin laminate theory is based on the classic lamination theory (CLT) to characterise the stress and strain with the following assumptions [48]: the displacement components are continuous throughout the laminates; each ply is thin and under plane stress;

the Kirchhoff-Love hypothesis is valid; the material of the plate is linear elastic with no slip between the lamina interfaces.

2.2.2.1 Stress and strain in a lamina

A UD lamina is considered as an orthotropic material. If a lamina is thin and there is no transverse loading, the plate is assumed to be in plane stress, which reduces the three-dimensional stress-strain equations to two-dimensional planar equations:

$$\begin{bmatrix} \varepsilon_1 \\ \varepsilon_2 \\ \gamma_{12} \end{bmatrix} = \begin{bmatrix} S_{11} & S_{12} & 0 \\ S_{12} & S_{22} & 0 \\ 0 & 0 & S_{66} \end{bmatrix} \begin{bmatrix} \sigma_1 \\ \sigma_2 \\ \tau_{12} \end{bmatrix} \tag{2-15}$$

where S_{ij} are the elements of the compliance matrix. Hence, the stress-strain relationship is given by inverting the above:

$$\begin{bmatrix} \sigma_1 \\ \sigma_2 \\ \tau_{12} \end{bmatrix} = \begin{bmatrix} Q_{11} & Q_{12} & 0 \\ Q_{12} & Q_{22} & 0 \\ 0 & 0 & Q_{66} \end{bmatrix} \begin{bmatrix} \varepsilon_1 \\ \varepsilon_2 \\ \gamma_{12} \end{bmatrix} \tag{2-16}$$

where Q_{ij} are the reduced stiffness coefficients, and related to the S_{ij} coefficients by:

$$Q_{11} = \frac{S_{22}}{S_{11}S_{22} - S_{12}^2} \tag{2-17}$$

$$Q_{12} = \frac{S_{12}}{S_{11}S_{22} - S_{12}^2} \tag{2-18}$$

$$Q_{22} = \frac{S_{11}}{S_{11}S_{22} - S_{12}^2} \tag{2-19}$$

$$Q_{66} = \frac{1}{S_{66}} \tag{2-20}$$

The compliance and reduced stiffness coefficients are related to the engineering elastic constants for a UD lamina by:

$$S_{11} = \frac{1}{E_1} \qquad Q_{11} = \frac{E_1}{1 - v_{12}v_{21}} \tag{2-21}$$

$$S_{12} = -\frac{v_{12}}{E_1} \qquad Q_{12} = \frac{v_{12}E_2}{1 - v_{12}v_{21}} \tag{2-22}$$

$$S_{22} = \frac{1}{E_2} \qquad Q_{22} = \frac{E_2}{1 - v_{12}v_{21}} \tag{2-23}$$

$$S_{66} = \frac{1}{G_{12}} \qquad Q_{66} = G_{12} \tag{2-24}$$

According to the symmetry condition of the stress tensor, $Q_{12} = Q_{21}$, the Young's modulus and Poisson's ratios should fulfil the following relations:

$$E_1 v_{21} = E_2 v_{12} \tag{2-25}$$

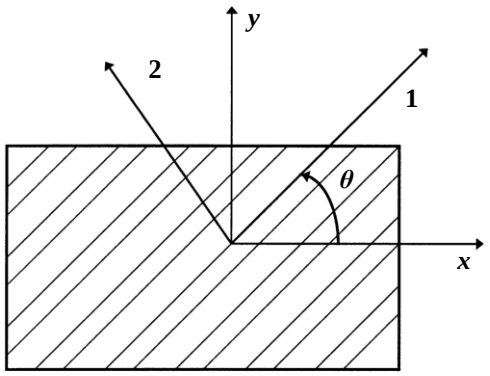

Figure 2-1 Local and global coordinate system of an fibre-angle lamina: '1' denotes the local fibre direction; '2' is the direction perpendicular to fibre; '*x*' is along the length and '*y*' is transverse; θ is the fibre angle.

Fibres in individual plies of a laminate are usually arranged at different angles to reinforce the material. For the lamina in Figure 2-1, the stress-strain relationship should be transformed from the local 1-2 coordinate system to the global *x*-*y* system. The global and local stresses in this inclined fibre-angle lamina are related to each other by a transformation matrix in terms of fibre angle, θ, *i.e.*:

$$\begin{bmatrix} \sigma_x \\ \sigma_y \\ \tau_{xy} \end{bmatrix} = [T]^{-1} \begin{bmatrix} \sigma_1 \\ \sigma_2 \\ \tau_{12} \end{bmatrix} \tag{2-26}$$

where $[T]$ is the transformation matrix:

$$[T] = \begin{bmatrix} c^2 & s^2 & 2sc \\ s^2 & c^2 & -2sc \\ -sc & sc & c^2 - s^2 \end{bmatrix} \tag{2-27}$$

and its inverse:

$$[T]^{-1} = \begin{bmatrix} c^2 & s^2 & -2sc \\ s^2 & c^2 & 2sc \\ sc & -sc & c^2 - s^2 \end{bmatrix} \tag{2-28}$$

with $c = \cos\theta$ and $s = \sin\theta$.

From the local constitutive laws in Eq. 2-16:

$$\begin{bmatrix} \sigma_x \\ \sigma_y \\ \tau_{xy} \end{bmatrix} = [T]^{-1}[Q] \begin{bmatrix} \varepsilon_1 \\ \varepsilon_2 \\ \gamma_{12} \end{bmatrix} \tag{2-29}$$

The global and local strain are also related through the transformation matrix:

$$\begin{bmatrix} \varepsilon_1 \\ \varepsilon_2 \\ \gamma_{12}/2 \end{bmatrix} = [T] \begin{bmatrix} \varepsilon_x \\ \varepsilon_y \\ \gamma_{xy}/2 \end{bmatrix} \tag{2-30}$$

and

$$\begin{bmatrix} \varepsilon_1 \\ \varepsilon_2 \\ \gamma_{12} \end{bmatrix} = [R][T] \begin{bmatrix} \varepsilon_x \\ \varepsilon_y \\ \gamma_{xy} \end{bmatrix} \tag{2-31}$$

where $[R]$ is the Reuter matrix and defined as:

$$[R] = \begin{bmatrix} 1 & 0 & 0 \\ 0 & 1 & 0 \\ 0 & 0 & 2 \end{bmatrix} \tag{2-32}$$

Thus

$$\begin{bmatrix} \sigma_x \\ \sigma_y \\ \tau_{xy} \end{bmatrix} = [T]^{-1}[Q][R][T] \begin{bmatrix} \varepsilon_x \\ \varepsilon_y \\ \gamma_{xy} \end{bmatrix} \tag{2-33}$$

Defining $[\bar{Q}]$ as the transformed reduced stiffness matrix, then:

$$[\bar{Q}] = [T]^{-1}[Q][R][T] \tag{2-34}$$

which results in:

$$\begin{bmatrix}\sigma_x\\ \sigma_y\\ \tau_{xy}\end{bmatrix}=\begin{bmatrix}\bar{Q}_{11} & \bar{Q}_{12} & \bar{Q}_{16}\\ \bar{Q}_{12} & \bar{Q}_{22} & \bar{Q}_{26}\\ \bar{Q}_{16} & \bar{Q}_{26} & \bar{Q}_{66}\end{bmatrix}\begin{bmatrix}\varepsilon_x\\ \varepsilon_y\\ \gamma_{xy}\end{bmatrix} \tag{2-35}$$

with the elements given by:

$$\bar{Q}_{11}=Q_{11}c^4+2(Q_{12}+2Q_{66})c^2s^2+Q_{22}s^4 \tag{2-36}$$

$$\bar{Q}_{12}=(Q_{11}+Q_{22}-4Q_{66})c^2s^2+Q_{12}(c^4+s^4) \tag{2-37}$$

$$\bar{Q}_{22}=Q_{11}s^4+2(Q_{12}+2Q_{66})c^2s^2+Q_{22}c^4 \tag{2-38}$$

$$\bar{Q}_{16}=(Q_{11}-Q_{12}-2Q_{66})c^3s+(Q_{12}-Q_{22}+2Q_{66})cs^3 \tag{2-39}$$

$$\bar{Q}_{26}=(Q_{11}-Q_{12}-2Q_{66})cs^3+(Q_{12}-Q_{22}+2Q_{66})c^3s \tag{2-40}$$

$$\bar{Q}_{66}=(Q_{11}+Q_{22}-2Q_{12}-2Q_{66})c^2s^2+Q_{66}(c^4+s^4) \tag{2-41}$$

2.2.2.2 Constitutive equations of UD laminate

Using the above, the constitutive equations of the *k*-th UD ply for a UD laminate with *n* plies, can be written as:

$$\begin{bmatrix}\sigma_x\\ \sigma_y\\ \tau_{xy}\end{bmatrix}_k=\begin{bmatrix}\bar{Q}_{11} & \bar{Q}_{12} & \bar{Q}_{16}\\ \bar{Q}_{12} & \bar{Q}_{22} & \bar{Q}_{26}\\ \bar{Q}_{16} & \bar{Q}_{26} & \bar{Q}_{66}\end{bmatrix}_k\begin{bmatrix}\varepsilon_x\\ \varepsilon_y\\ \gamma_{xy}\end{bmatrix}_k=\begin{bmatrix}\bar{Q}_{11} & \bar{Q}_{12} & \bar{Q}_{16}\\ \bar{Q}_{12} & \bar{Q}_{22} & \bar{Q}_{26}\\ \bar{Q}_{16} & \bar{Q}_{26} & \bar{Q}_{66}\end{bmatrix}_k\left\{\begin{bmatrix}\varepsilon_x^0\\ \varepsilon_y^0\\ \gamma_{xy}^0\end{bmatrix}+z\begin{bmatrix}\kappa_x\\ \kappa_y\\ \kappa_{xy}\end{bmatrix}\right\} \tag{2-42}$$

The reduced transformed stiffness matrix, $[\bar{Q}]$, corresponds to the ply along the thickness of the laminate, and a strain with superscript 0 denotes the strain of the mid-plane of the laminate: the curvatures in the *x*- and *y*-directions are κ_x and κ_y, with κ_{xy} as the twisting curvature.

The stresses in each lamina can be integrated through the laminate thickness to give stress resultants of force and moment:

$$\begin{bmatrix}N_x\\ N_y\\ N_{xy}\end{bmatrix}=\sum_{k=1}^{n}\int_{h_{k-1}}^{h_k}\begin{bmatrix}\sigma_x\\ \sigma_y\\ \tau_{xy}\end{bmatrix}_k\mathrm{d}z=\sum_{k=1}^{n}\int_{h_{k-1}}^{h_k}\begin{bmatrix}\bar{Q}_{11} & \bar{Q}_{12} & \bar{Q}_{16}\\ \bar{Q}_{12} & \bar{Q}_{22} & \bar{Q}_{26}\\ \bar{Q}_{16} & \bar{Q}_{26} & \bar{Q}_{66}\end{bmatrix}_k\begin{bmatrix}\varepsilon_x^0\\ \varepsilon_y^0\\ \gamma_{xy}^0\end{bmatrix}\mathrm{d}z+\sum_{k=1}^{n}\int_{h_{k-1}}^{h_k}\begin{bmatrix}\bar{Q}_{11} & \bar{Q}_{12} & \bar{Q}_{16}\\ \bar{Q}_{12} & \bar{Q}_{22} & \bar{Q}_{26}\\ \bar{Q}_{16} & \bar{Q}_{26} & \bar{Q}_{66}\end{bmatrix}_k\begin{bmatrix}\kappa_x\\ \kappa_y\\ \kappa_{xy}\end{bmatrix}z\mathrm{d}z \tag{2-43}$$

$$\begin{bmatrix}M_x\\ M_y\\ M_{xy}\end{bmatrix}=\sum_{k=1}^{n}\int_{h_{k-1}}^{h_k}\begin{bmatrix}\sigma_x\\ \sigma_y\\ \tau_{xy}\end{bmatrix}_k z\mathrm{d}z=\sum_{k=1}^{n}\int_{h_{k-1}}^{h_k}\begin{bmatrix}\bar{Q}_{11} & \bar{Q}_{12} & \bar{Q}_{16}\\ \bar{Q}_{12} & \bar{Q}_{22} & \bar{Q}_{26}\\ \bar{Q}_{16} & \bar{Q}_{26} & \bar{Q}_{66}\end{bmatrix}_k\begin{bmatrix}\varepsilon_x^0\\ \varepsilon_y^0\\ \gamma_{xy}^0\end{bmatrix}z\mathrm{d}z+\sum_{k=1}^{n}\int_{h_{k-1}}^{h_k}\begin{bmatrix}\bar{Q}_{11} & \bar{Q}_{12} & \bar{Q}_{16}\\ \bar{Q}_{12} & \bar{Q}_{22} & \bar{Q}_{26}\\ \bar{Q}_{16} & \bar{Q}_{26} & \bar{Q}_{66}\end{bmatrix}_k\begin{bmatrix}\kappa_x\\ \kappa_y\\ \kappa_{xy}\end{bmatrix}z^2\mathrm{d}z \tag{2-44}$$

Using the following definitions:

$$\boldsymbol{A}_{ij} = \sum_{k=1}^{n} \left(\bar{Q}_{ij}\right)_k (h_k - h_{k-1}), \qquad i,j = 1,2,6 \tag{2-45}$$

$$\boldsymbol{B}_{ij} = \frac{1}{2}\sum_{k=1}^{n} \left(\bar{Q}_{ij}\right)_k (h_k^2 - h_{k-1}^2), \qquad i,j = 1,2,6 \tag{2-46}$$

$$\boldsymbol{D}_{ij} = \frac{1}{3}\sum_{k=1}^{n} \left(\bar{Q}_{ij}\right)_k (h_k^3 - h_{k-1}^3), \qquad i,j = 1,2,6 \tag{2-47}$$

the [**A**], [**B**], and [**D**] matrices thus correspond to the extensional, strain-curvature coupling, and bending stiffness matrices, respectively. The constitutive equation of a laminate is:

$$\begin{Bmatrix} N_x \\ N_y \\ N_{xy} \\ M_x \\ M_y \\ M_{xy} \end{Bmatrix} = \begin{bmatrix} A_{11} & A_{12} & A_{16} & B_{11} & B_{12} & B_{16} \\ A_{12} & A_{22} & A_{26} & B_{12} & B_{22} & B_{26} \\ A_{16} & A_{26} & A_{66} & B_{16} & B_{26} & B_{66} \\ B_{11} & B_{12} & B_{16} & D_{11} & D_{12} & D_{16} \\ B_{12} & B_{22} & B_{26} & D_{12} & D_{22} & D_{26} \\ B_{16} & B_{26} & B_{66} & D_{16} & D_{26} & D_{66} \end{bmatrix} \begin{Bmatrix} \varepsilon_x^0 \\ \varepsilon_y^0 \\ \gamma_{xy}^0 \\ \kappa_x \\ \kappa_y \\ \kappa_{xy} \end{Bmatrix} \tag{2-48}$$

or

$$\begin{Bmatrix} N_i \\ M_i \end{Bmatrix} = \begin{bmatrix} \boldsymbol{A}_{ij} & \boldsymbol{B}_{ij} \\ \boldsymbol{B}_{ij} & \boldsymbol{D}_{ij} \end{bmatrix} \begin{Bmatrix} \varepsilon_j \\ \kappa_j \end{Bmatrix} \qquad i,j = 1,2,6 \tag{2-49}$$

2.2.2.3 Constitutive equations of woven laminate

For a woven laminate, there have been several models to study the in-plane elastic properties of various fabric weaves. Based on the CLT, Naik and Shembekar [49,50] developed a 2D model to predict in-plane elastic properties, which consider undulation of the strands, actual strand cross-section and weave geometry, and the strand fibre volume fraction. The in-plane stiffness constants follow:

$$\begin{aligned} \boldsymbol{A}_{ij}(x,y) = {} & Q_{ij}^{M}[hx_3(x,y) + h - hx_2(x,y)] + Q_{ij}^{W}(x,y)[hx_2(x,y) - hx_1(x,y)] \\ & + Q_{ij}^{F}(x,y)[hx_1(x,y) - hx_3(x,y)] \end{aligned} \tag{2-50}$$

$$\boldsymbol{B}_{ij}(x,y) = \frac{1}{2}Q_{ij}^{M}[hx_3(x,y)^2 - hx_2(x,y)^2] + \frac{1}{2}Q_{ij}^{W}(x,y)[hx_2(x,y)^2 - hx_1(x,y)^2] + \frac{1}{2}Q_{ij}^{F}(x,y)[hx_1(x,y)^2 - hx_3(x,y)^2] \tag{2-51}$$

$$\boldsymbol{D}_{ij}(x,y) = \frac{1}{3}Q_{ij}^{M}\left[hx_3(x,y)^3 - \frac{h^3}{8} - hx_2(x,y)^3\right] + \frac{1}{3}Q_{ij}^{W}(x,y)[hx_2(x,y)^3 - hx_1(x,y)^3] + \frac{1}{3}Q_{ij}^{F}(x,y)[hx_1(x,y)^3 - hx_3(x,y)^3] \tag{2-52}$$

Based on the 2D woven model above, Lamers *et al.* [51] developed it further by considering the yarn shape, with:

$$\boldsymbol{A}_{ij}^{e}(x,y) = Q_{ij}^{R}[h_{Wt}^{e}(x,y) - h_{t}^{e}(x,y) + h_{Ft}^{e}(x,y) - h_{Wb}^{e}(x,y) + h_{b}^{e}(x,y) - h_{Fb}^{e}(x,y)] + Q_{ij}^{W}(\theta_x)[h_{Wb}^{e}(x,y) - h_{Wt}^{e}(x,y)] + Q_{ij}^{F}(\theta_y)[h_{Fb}^{e}(x,y) - h_{Ft}^{e}(x,y)] \tag{2-53}$$

$$\boldsymbol{B}_{ij}^{e}(x,y) = Q_{ij}^{R}[h_{Wt}^{e}(x,y)^2 - h_{t}^{e}(x,y)^2 + h_{Ft}^{e}(x,y)^2 - h_{Wb}^{e}(x,y)^2 + h_{b}^{e}(x,y)^2 - h_{Fb}^{e}(x,y)^2] + Q_{ij}^{W}(\theta_x)[h_{Wb}^{e}(x,y)^2 - h_{Wt}^{e}(x,y)^2] + Q_{ij}^{F}(\theta_y)[h_{Fb}^{e}(x,y)^2 - h_{Ft}^{e}(x,y)^2] \tag{2-54}$$

$$\boldsymbol{D}_{ij}^{e}(x,y) = Q_{ij}^{R}[h_{Wt}^{e}(x,y)^3 - h_{t}^{e}(x,y)^3 + h_{Ft}^{e}(x,y)^3 - h_{Wb}^{e}(x,y)^3 + h_{b}^{e}(x,y)^3 - h_{Fb}^{e}(x,y)^3] + Q_{ij}^{W}(\theta_x)[h_{Wb}^{e}(x,y)^3 - h_{Wt}^{e}(x,y)^3] + Q_{ij}^{F}(\theta_y)[h_{Fb}^{e}(x,y)^3 - h_{Ft}^{e}(x,y)^3] \tag{2-55}$$

or

$$\begin{Bmatrix} N_i \\ M_i \end{Bmatrix} = \begin{bmatrix} \boldsymbol{A}_{ij}^{e}(x,y) & \boldsymbol{B}_{ij}^{e}(x,y) \\ \boldsymbol{B}_{ij}^{e}(x,y) & \boldsymbol{D}_{ij}^{e}(x,y) \end{bmatrix} \begin{Bmatrix} \varepsilon_j \\ \kappa_j \end{Bmatrix} \qquad i,j = 1,2,6 \tag{2-56}$$

2.2.3 Constitutive specification

The tape-spring material involved in this report is either isotropic or orthotropic which does not require that level of generality as shown above. The composite layup is effectively symmetrical, and there is no bending-stretching coupling. Thus, for the sake of simpler notation, the orthotropic behaviour is captured by four independent parameters: E, ν, ρ, β.

A theoretical analysis follows the plane-stress assumption, with in-plane stress σ, and in-plane strain ϵ. The coordinate system follows Figure 2-1 with z in the through-thickness direction. Define a modular ratio, $\beta = E_y/E_x$: the corresponding Possion's ratios obey the Reciprocal Theorem according to $\upsilon_{xy}/E_x = \upsilon_{yx}/E_y$. Thus, the engineering constants become:

$$E_x = E, \qquad E_y = \beta E, \qquad G = \rho E, \qquad v_{yx} = v, \qquad v_{xy} = v/\beta \tag{2-57}$$

The shear modulus is G with $\rho = 1/2(1+v)$ for isotropic material ($\beta = 1$). The constitutive relations for in-plane strains are then written:

$$\epsilon_x = \frac{\sigma_x}{E} - \frac{v\sigma_y}{\beta E}, \qquad \epsilon_y = -\frac{v\sigma_x}{\beta E} + \frac{\sigma_y}{\beta E}, \qquad \gamma_{xy} = \frac{\tau_{xy}}{\rho E} \tag{2-58}$$

The stresses follow, again, from inverting the above:

$$\sigma_x = \frac{E}{1 - v^2/\beta}(\epsilon_x + v\epsilon_y), \qquad \sigma_y = \frac{E\beta}{1 - v^2/\beta}(\epsilon_y + \frac{v\epsilon_x}{\beta}), \qquad \tau_{xy} = \gamma_{xy}\rho E \tag{2-59}$$

Bending and stretching of any tape-spring is expressed by the deformation of its internal middle surface. When the in-plane behaviour correlates to the above stresses and strains, the corresponding stretching strain energy density per unit surface area can be written as:

$$U_S = \frac{t}{2}\left(\sigma_x\epsilon_x + \sigma_y\epsilon_y + \tau_{xy}\gamma_{xy}\right) = \frac{t}{2E}\left(\sigma_x^2 + \frac{\sigma_y^2}{\beta} - \frac{2v\sigma_x\sigma_y}{\beta} + \frac{\tau_{xy}^2}{\rho}\right) \tag{2-60}$$

When there are changes in curvature of the middle surface, the strains vary linearly with material height z through the thickness from Kirchoff's hypothesis [52], and $\epsilon_x = z\chi_x$, $\epsilon_y = z\chi_y$, and $\gamma_{xy} = 2z\chi_{xy}$. The bending moment stress resultants per unit in-plane length are:

$$M_x = \frac{Et^3}{12(1 - v^2/\beta)}(\chi_x + v\chi_y), \qquad M_y = \frac{Et^3}{12(1 - v^2/\beta)}(\chi_y + \frac{v\chi_x}{\beta}), \qquad M_{xy} = \frac{Et^3\rho}{6}\chi_{xy} \tag{2-61}$$

The corresponding strain energy density in bending is:

$$U_B = \frac{D}{2}\left(\chi_x^2 + \beta\chi_y^2 + 2v\chi_x\chi_y + 2\alpha\chi_{xy}^2\right) \tag{2-62}$$

with flexural rigidity, $D = Et^3/12(1 - v^2/\beta)$, and dimensionless torsional rigidity, $\alpha = 4(1 - v^2/\beta)/\rho$. For isotropic materials, $\alpha = 1 - v$; for our composite tapes, $\alpha \approx 1.11$ [53].

2.2.4 Strain gauge measurement

Strain gauges are employed to ensure reliable strain measurements compared to the machine crosshead motion method [54]. Following Naik's model [55], the plain woven composite is also considered as an orthotropic material. For a strain gauge subjected to a biaxial-strain field at constant temperature as shown in Figure 2-2-a, the change in gauge resistance is [56]:

$$\frac{\Delta R_\Omega}{R_\Omega} = f_a \varepsilon_a + f_t \varepsilon_t \tag{2-63}$$

R_Ω is the original gauge resistance; ΔR_Ω is the change in gauge resistance; f_a and f_t are the gauge factors of strain gauge in the axial and transverse directions, respectively; ε_a and ε_t are the corresponding surfaces strains. The transverse sensitivity coefficient, K_t, is defined as: $K_t = F_t/F_a$, whence:

$$\frac{\Delta R_\Omega}{R_\Omega} = f_a(\varepsilon_a + K_t \varepsilon_t) \tag{2-64}$$

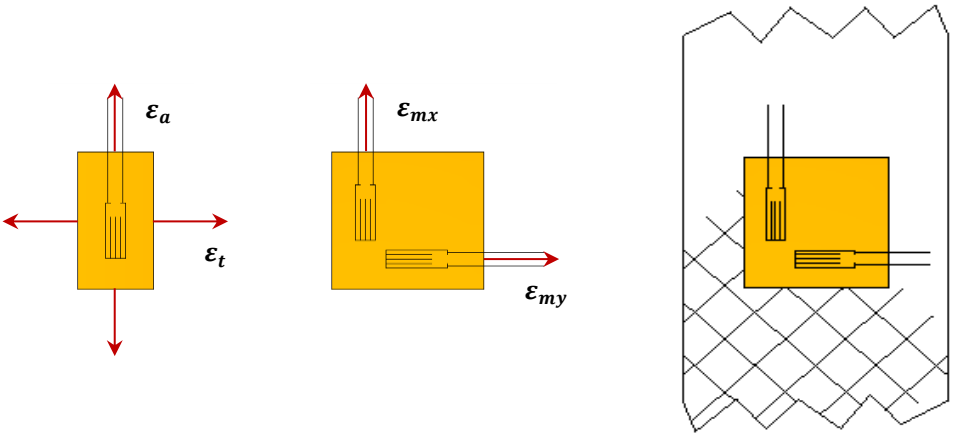

(a) **(b)** **(c)**

Figure 2-2 Arrangement of strain gauges: (a) single strain gauge; (b) a biaxial strain gauge rosette; (c) composite sample with bonded strain gauge rosette.

When subjected to a uniaxial stress field with the strain gauge parallel to the stress, the transverse strain experienced by the gauge is:

$$\varepsilon_t = -v\varepsilon_a \tag{2-65}$$

where v is the Poisson's ratio of the standard calibration material used by the supplier (normally steel with $v = 0.3$). In this loading condition,

$$\frac{\Delta R_\Omega}{R_\Omega} = f_a(1 - K_t v)\, \varepsilon_a \tag{2-66}$$

The manufacturer's gauge factor (MGF) is defined as:

$$MGF = f_a(1 - Kv) \tag{2-67}$$

Therefore, the strain measure, ε_m, follows:

$$\varepsilon_m = \varepsilon_a = \frac{f_a(1 - K_t v)\, \varepsilon_a}{MGF} \tag{2-68}$$

For non-uniaxial loading, the measured strain must be corrected for transverse-sensitivity effects, where at least two orthogonal strain measurements are required for correction [57]. A biaxial strain gauge rosette is shown schematically in Figure 2-2-b, with two strain gauges to measure two orthogonal normal strains, denoted by ε_{mx} and ε_{my}. By considering the transverse-sensitivity corrections, the true strain in *x*- and *y*-direction, ε_x and ε_y, are:

$$\varepsilon_x = \frac{(1 - K_t v)(\varepsilon_{mx} - K_t \varepsilon_{my})}{1 - K^2} \tag{2-69}$$

$$\varepsilon_y = \frac{(1 - K_t v)(\varepsilon_{my} - K_t \varepsilon_{mx})}{1 - {K_t}^2} \tag{2-70}$$

The error in the measured strain due to the transverse sensitivity is thus:

$$\text{Error} = \frac{K_t(\frac{\varepsilon_t}{\varepsilon_a} + v)}{1 - K_t v} \tag{2-71}$$

The in-plane shear strain can be determined using strain gauges following the testing standard ASTM D3518 on plain-weave ±45˚ laminates [58] as shown in Figure 2-2-c. The shear stress on the principal material plane is the same for each lamina in the laminate, and equals to half

of the axial stress [58]; the shear strain is also the same in each lamina. The difference in indicated strains from two gauges with their axes 90˚ apart is equal to the shear strain along the bisector of those axes [57], *i.e.*:

$$\gamma_{12} = \varepsilon_x - \varepsilon_y \tag{2-72}$$

A common method of gauge alignment when mounting strain gauges to conventional materials is to first burnish alignment marks on the specimen surface; however, it is not practical with composite materials [56]. The weave pattern left by the scrim cloth can also be misleading since it may not necessarily reflect the true fibre direction. Thus, a strain measurement error occurs when a strain gauge is misaligned with respect to the intended axis of strain measurement [59]; and a small misalignment error produces a much larger error in measured strain for composites than for the isotropic systems [57]. Assuming the gauge is mounted by θ degree, with a gauge misalignment angle of θ' as shown in Figure 2-3, the actual axial and transverse strains may be determined as [48]:

$$\begin{Bmatrix} \varepsilon_x{}' \\ \varepsilon_y{}' \\ \gamma_{xy}{}'/2 \end{Bmatrix} = \begin{bmatrix} m^2 & n^2 & 2mn \\ n^2 & m^2 & -2mn \\ -mn & mn & m^2 - n^2 \end{bmatrix} \begin{Bmatrix} \varepsilon_x \\ \varepsilon_y \\ \gamma_{xy}/2 \end{Bmatrix} \tag{2-73}$$

where, $m = \cos\theta'$; $n = \sin\theta'$.

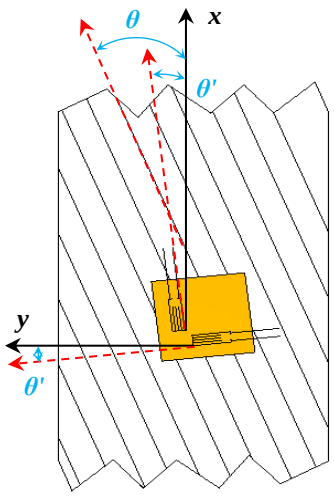

Figure 2-3 Schematic illustration of gauge misalignment.

2.3 EXPERIMENTAL

2.3.1 Materials

The plain weave GF fabric gives well-balanced properties for laminates other than UD fabrics. The GF fabrics were supplied by MB Fibreglass Ltd, UK; the PP sheets were supplied by GoodFellow Cambridge Ltd, UK. Table 2-1 shows the materials properties, and Figure 2-4 shows the sample appearance.

Table 2-1 Materials properties of GF fabrics and PP sheets.

Materials	GF fabric [60]			PP sheet [61]	
Density	81 g/m^2	175 g/m^2	200 g/m^2	0.9 g/cm^3	0.9 g/cm^3
Thickness (mm)	0.09	0.24	0.20	0.5	1.0
Construction warp×weft (th/cm)	12.6×11.1	6.6×6.2	7.4×7.4	--	--
Type of yarn	EC9 34×2	EC9 136×2	EC9 68×2	--	--
Poisson's ratio	0.2			0.42	
Elastic modulus (GPa)	72.4			1.53	
Shear modulus (GPa)	30			0.54	
Thermal expansion coefficient (μm/m°C)	5.0			84.8	

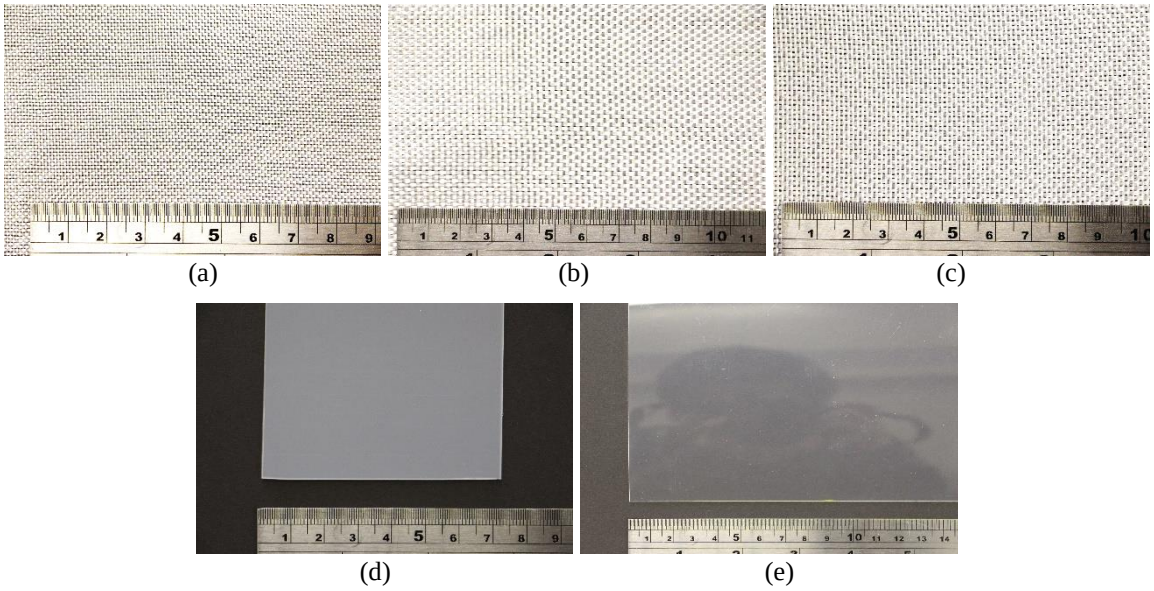

(a) (b) (c)

(d) (e)

Figure 2-4 Materials used: (a) 81 gsm GF woven; (b) 175 gsm GF woven; (c) 200 gsm GF woven; (d) 1.0 mm PP sheet; (e) 0.5 mm PP sheet.

2.3.2 Production of composite tape-springs

A simple manufacturing process for fabricating the CTS was followed. Briefly, a specific composite layup consisted of different layers of GF fabric and PP sheet (as in Table 2-1). The composite layup was placed between two PTFE coated glass fabric papers, and gradually wrapped and tightened on a cylindrical mould (Ø25 × 300 mm) by using a heat shrink tape. A jubilee clip was employed to lock the whole layup at the end. A fan-assisted oven was preheated to a designated temperature before the wrapped mould was placed inside for heating. Following heat treatment, the shrink tape and PTFE paper were released, and the composite sample was manually cut to the correct size before testing.

2.3.3 Mechanical testing

To evaluate the composite mechanical properties, flat samples were produced with embedded strain gauges. Production of flat samples is similar to Section 2.3.2, using a flat steel plate of size (320 × 50 × 3 mm) for a mould, with strain gauges placed on the outer surface of the composite layup. This arrangement ensured direct contact between the strain gauges and samples to minimise effects from using adhesives, as well as keeping minimal effects to the mechanical performance of composites. Mechanical tests were carried out using an Instron 4483 universal tensile machine with a 30 kN load cell at room temperature. Figure 2-5 shows a typical experimental setup where a constant crosshead speed of 2 mm/min was adopted for all tests. The embedded strain gauge was soldered to a lead pad, and connected to a National Instrument PXIe-1071 series transducer; strain data were monitored and recorded at 2 Hz. A sample dimension of 250 × 30 × 0.65 mm was employed with a testing span of 190 mm. A 6 mm strain gauge with 120 Ω was supplied by Tokyo Sokki Kenkyujo Co. Ltd., with a thermal expansion coefficient of 11 μm/(m·˚C), and transverse sensitivity (K_t) of 0.1%.

Elastic properties in fibre direction were determined by testing samples with warp fibres in the longitudinal and transverse directions following ASTM D3039 [62], the layups being designated as $[0F/90F]_3$ and $[90F/0F]_3$ separately. Shear properties of the composite were derived from tests of in-plane shear responses according to ASTM D3518 [58] with warp fibres oriented at 45˚, and the layup denoted as $[\pm 45F]_3$. Three samples for each test were conducted

to evaluate repeatability. The stress was calculated by dividing the tensile force at each data point by the original cross-sectional area of each sample.

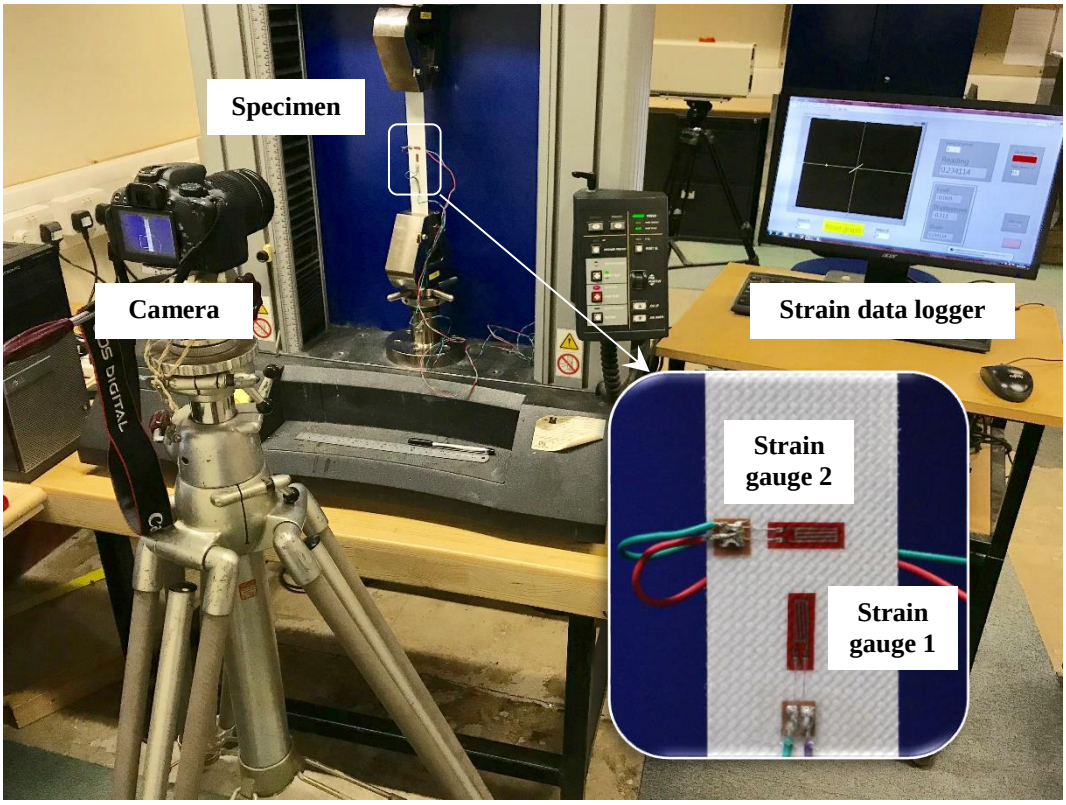

Figure 2-5 Experimental setup for the tensile testing of flat composite samples with embedded strain gauges (inset).

2.3.4 Optical microscopy

Though the plain-weave GF fabric used have the same warp and weft yarn count as in Table 2-1, the mechanical properties of woven composite are also dependent on the yarn bundle geometry [55]. Thus, the cross-section of the selected composite layup was evaluated by using optical microscope to determine detailed fabric geometry. Flat woven composite samples were embedded into an epoxy matrix and, following resin curing, the specimen was progressively ground and polished prior to microscopy work.

2.4 RESULTS AND DISCUSSION

2.4.1 Selection of raw materials and layup

Though bistability is not necessary for a landing gear folding hinge design, it was used to examine the quality of CTS samples, since any misalignment of fabric would cause the sample to become skewed when coiled. Thus, multiple combinations of GF fabrics and PP sheets were used to produce bistable tubes. Initial trials utilised 175 gsm GF woven and 1.0 mm PP sheet, but none of the samples worked well; however, these give some guidance and insight for further improvement: in particular, with 1.0 mm PP sheet, the composite tubes were too stiff to be bistable, and a poor fibre-matrix interface was observed. Thus, we decided to use 81 gsm GF woven and 0.5 mm PP sheet. The results were encouraging, and some of the layups used are listed in Table 2-2. The first time we obtained bistability was with tube No 6, and the moulding conditions were 195 ˚C for 1.5 h. Though the sample is bistable, there is clear delamination throughout the sample when coiled, as shown in Figure 2-6-a. More samples were therefore produced to improve the bonding of fibre-matrix interfaces. By increasing the moulding temperature and time, it was found that delamination could be improved but hardly avoided. Tube No 8 was the best as presented in Figure 2-6-b. Increasing the moulding temperature was not considered due to a higher risk of ageing and damage to the glass fibres.

Table 2-2 Experimental trials of different layups to produce bistable tubes.

Tube	Length (mm)	Mould (mm)	Circumference (mm)	Subtended angle (˚)	Moulding conditions (˚C)	V_f (%)	Layup
6	200	25	70	321	195 ˚C-1.5 h	11.31	81 GF/0.5 PP/81 GF
7	200	31	90	333	225 ˚C-1.5 h	11.31	81 GF/0.5 PP/81 GF
8	200	31	90	333	225 ˚C-3.0 h	11.31	81 GF/0.5 PP/81 GF
10	200	31	90	333	225 ˚C-3.0 h	11.31	2×81 GF/0.5 PP
11	200	31	90	333	225 ˚C-3.0 h	11.31	0.5 PP/2×81 GF
13	200	31	90	333	225 ˚C-3.0 h	6.01	0.5 PP/2×81 GF/0.5 PP
14	200	31	90	333	225 ˚C-3.0 h	11.31	0.5 PP/4×81 GF/0.5 PP
15	200	31	90	333	225 ˚C-3.0 h	16.06	0.5 PP/6×81 GF/0.5 PP
16	200	31	90	333	225 ˚C-3.0 h	20.33	0.5 PP/8×81 GF/0.5 PP
17	200	31	90	333	225 ˚C-3.0 h	24.18	0.5 PP/10×81 GF/0.5 PP

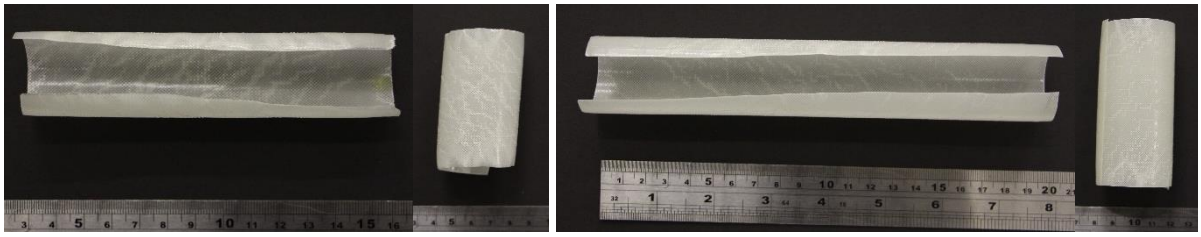

(a) **(b)**

Figure 2-6 Bistable CTS samples produced at (a) 195 ˚C for 1.5 h and (b) 225 ˚C for 3 h. Delamination is clear in both cases.

Based on the success of the above bistability, we altered the layers and kept the same volume fraction as per tubes 10 and 11. By putting the two GF layers together, the delamination problem, Figure 2-6, was resolved but new issues occurred. Since the thermal expansion coefficient of PP is around 20 times higher than GF, the PP sheet was placed inside the mould for tube 10, but ended up with much smaller dimeter than the mould. However, with PP bonded outside of the GF, sample No 11 was quite flat, ending up with longitudinal curvature. To solve the issues caused by the mismatch of the thermal expansion coefficient of fabric and matrix, further samples were made with two PP layers placed on the top and bottom of the GF woven layers to balance the shrinkage of the PP matrix. Tubes 13-17 were made with different volume fractions, as listed in Table 2-2, in order to evaluate its effects on bistability. Though there is no delamination for samples 13-15, tubes 13 and 14 were not bistable, and tube 15 was just bistable. Samples 16 and 17 had good bistability, but it was observed that because of too many layers of GF fabrics, the PP could not penetrate through all of the layers, and the resin was not evenly distributed.

Table 2-3 Experimental trials of different layups to produce bistable CTS samples.

Tube	Length (mm)	Mould (mm)	Circumference (mm)	Subtended angle (˚)	Moulding conditions (˚C)	V_f	Layups (outside to inside)
B4	130	31	57	333	225 ˚C-3.0 h	13.31	0.5 PP/200 GF
B5	200	31	70	333	225 ˚C-3.0 h	23.49	0.5 PP/2×200 GF
B6-a	200	31	90	333	225 ˚C-3.0 h	31.54	0.5 PP/3×200 GF
B6-b	200	31	90	333	225 ˚C-4.0 h	31.54	0.5 PP/3×200 GF
B7	200	31	90	333	225 ˚C-3.0 h	38.05	0.5 PP/4×200 GF
B8	200	31	90	333	225 ˚C-3.0 h	31.54	0.5 PP/6×200 GF/0.5 PP
B10	200	31	90	333	225 ˚C-3.0 h	23.49	0.5 PP/2×200 GF/0.5 PP/2×200 GF

It is concluded that to produce a bistable CTS sample: (i) a minimum value of V_f is needed to generate the bistability; (ii) layers of GF fabric need to be placed together to avoid premature delamination during the coiling process; (iii) the GF woven with space between warp/weft yarn was preferred for better penetration of the matrix resin.

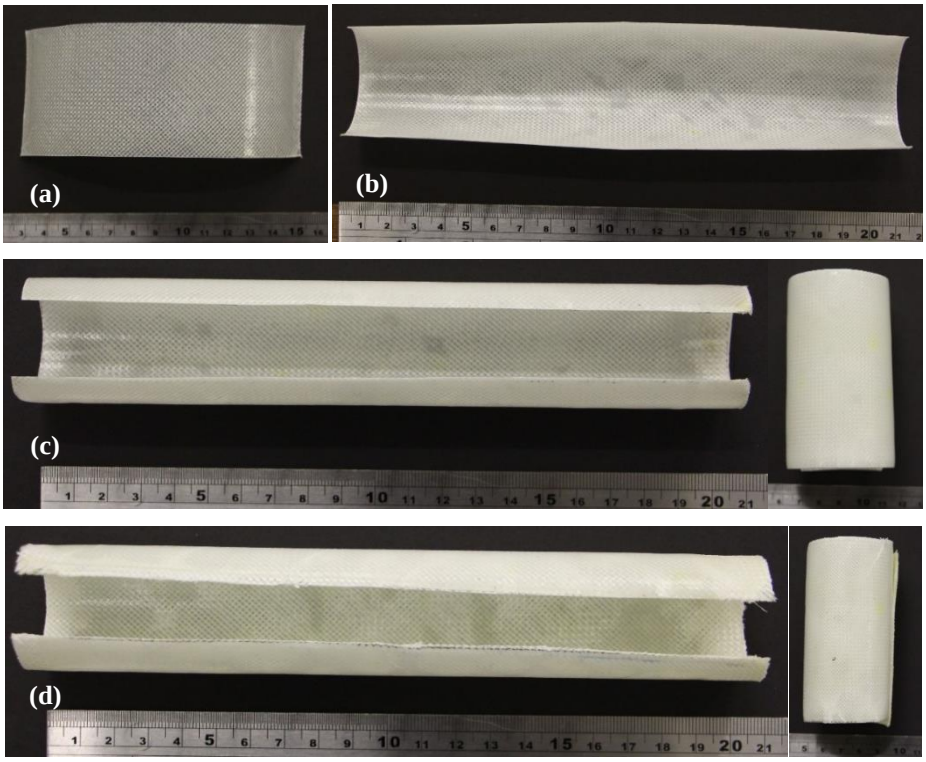

Figure 2-7 Composite tubes produced following layups showed in Table 2-3: (a) sample B4; (b) sample B5; (c) sample B6-a; (d) sample B7.

From these experiences, the fabric material was changed to 200 gsm woven GF. Unlike the 175 gsm woven GF, it has more space between the warp and weft fibre tows, as shown in Figure 2-4, which would benefit the penetration of matrix resin. Samples were made following the layups in Table 2-3, and Figure 2-7 gives their appearances. Similar to previous findings using a lower V_f, by placing the PP sheet outside of the GF layers there is expansion in the diameter of the sample due to a higher thermal expansion coefficient of the matrix. For sample B4, a longitudinal curvature was developed upon releasing the mould (Figure 2-7-a); there is a very clear expansion of sample B5 as well (Figure 2-7-b). By employing more GF layers, the expansion problem was significantly reduced in samples B6-a (Figure 2-7-c) and B7 (Figure 2-7-d), and both samples behave with bistability. Again, the fibre-matrix bonding in some regions of sample B7 are poor, which would affect the composite properties significantly. The composite layup of B6-a, i.e. $[\pm 45F]_3$, was therefore selected for further investigation. A better

sample quality was achieved by increasing the period of heat treatment to 4 hours, *i.e.* sample B6-b, which was adopted for subsequent research. The average thickness of the selected composite layup was measured using digital callipers and was typically 0.65 mm.

2.4.2 Tensile properties

The mechanical properties of the selected composite layup were evaluated with embedded strain gauges, and Table 2-4 shows the results for tensile behaviour. Figure 2-8 shows a typical tensile stress-strain curve for a three-layered woven composite. It is noticed that the strain gauges start to detach from the sample surface at strains around 0.0025, see Figure 2-8: thus, the modulus could be determined using the strain values from both the strain gauges and crosshead motion; while the strain at failure was only determined from the crosshead movement. The composite sample was linear elastic until failure, where the tensile strength in warp (σ_1^{WC}) and weft (σ_2^{WC}) directions are 215 MPa and 198 MPa, respectively, corresponding to failure strains of $\varepsilon_{1f}^{PW} = 3.46\%$ and $\varepsilon_{2f}^{PW} = 2.34\%$ [63].

Table 2-4 Tensile test results of flat composite samples with embedded strain gauges. SE is the ''standard error''.

Sample No	Tensile strength (MPa)	Strain at failure (%)	Modulus (GPa)		Poisson's ratio
			Strain gauge	Crosshead motion	
$[0/90]_3$	σ_1^{WC}	ε_{1f}^{WC}	E_1^{WC}		ν_{12}
1	206.68	3.55	12.79	8.39	0.11
2	206.52	3.56	12.27	6.11	0.12
3	233.08	3.26	13.90	10.10	0.11
Mean ± SE	215.43 ± 8.83	3.46 ± 0.10	12.99 ± 0.48	8.20 ± 1.16	0.11 ± 0.01
$[90/0]_3$	σ_2^{WC}	ε_{2f}^{WC}	E_2^{WC}		ν_{21}
1	196.29	2.33	15.52	11.01	0.13
2	203.05	2.34	18.69	8.66	0.16
3	194.8695	2.34	13.98	8.46	0.21
Mean ± SE	198.07 ± 2.52	2.34 ± 0.01	16.06 ± 1.39	9.38 ± 0.82	0.17 ± 0.03

The modulus values derived from different strain data have a large variance, highlighted by the inset, Figure 2-8; the strain gauge data give more accurate strain measurements. In addition, the transverse-sensitivity effects have been corrected following Section 2.2.3. Any discrepancy from the crosshead motion may be attributed to a lack of sensitivity of the sample deformation near the grips and to transverse sensitivity effects. Thus, the elastic moduli of composite were determined to be $E_1^{WC} = 12.99$ GPa, and $E_2^{WC} = 16.06$ GPa. As the woven composite was

fabricated with same fibre counts in both directions, the Young's modulus in the warp direction was found to be slightly lower than in the weft direction. A similar variance was obtained for Poisson's ratio, with v_{12}=0.11 compared to v_{21}=0.17, which may be caused by the differences of fibre tow geometry in the warp and weft directions [55]; this is further addressed in Section 2.4.4.

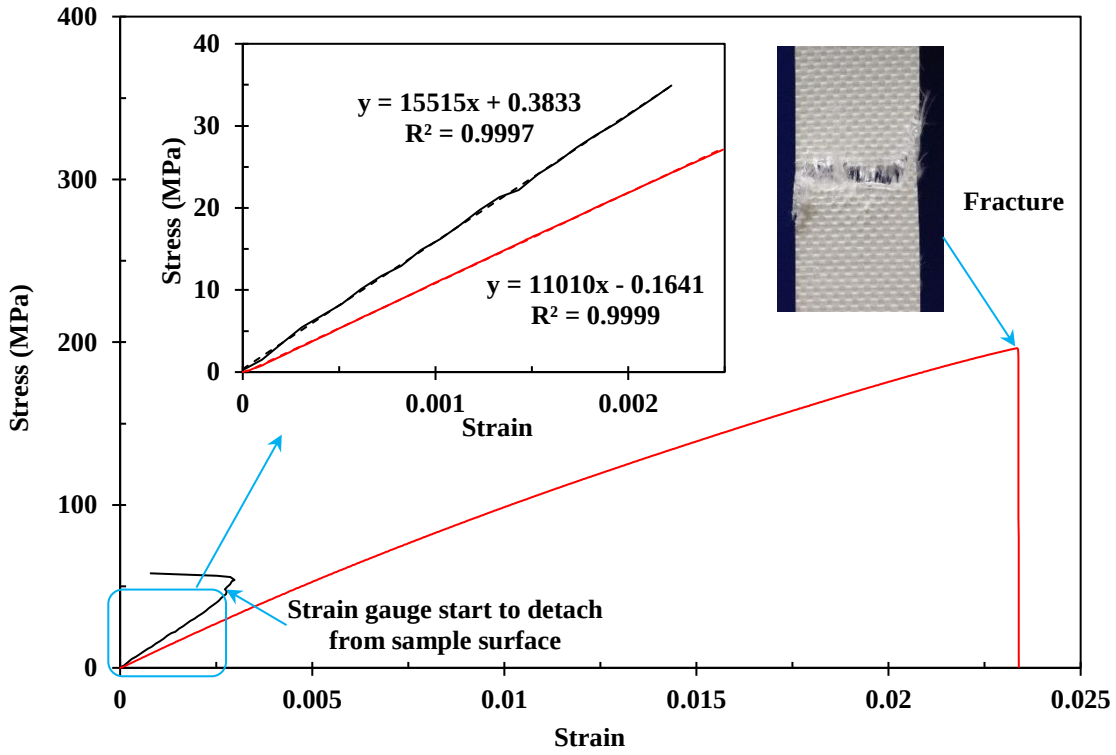

Figure 2-8 Tensile stress-strain curve of a flat composite sample, showing the stress-strain curves derived from both strain gauges (black) and crosshead movement (red).

The H-S bounds based micromechanical model (Section 2.2.1.2) can be applied to predict the engineering constants of the GF/PP woven composite. With 30% V_f, it gives $E_1^{WC} = E_2^{WC}$=13.70 GPa, and $v_{12} = v_{21} = 0.10$. Despite the experimental system error, these agree well with the mean measured modulus value of 14.53 GPa and Poisson's ratio of 0.14.

2.4.3 Shear properties

A typical shear stress-strain curve of the composite is shown in Figure 2-9, and Table 2-5 shows the shear properties of a flat $[\pm 45F]_3$ composite sample with embedded strain gauges. Again, the strain gauges detach at a strain value around 0.008, as highlighted, and a linear elastic shear modulus was observed until a strain level of 1%. It then becomes nonlinear, followed by a

second almost linear response, with a lateral shear modulus $G_{12}^{WC*} = 80$ MPa before fully fracturing. The shear strength and shear strain at failure were 42 MPa and 27%, respectively. The shear modulus calculated from embedded strain gauges agrees well with predictions from the micromechanical model, *i.e.* 824 MPa against 978 MPa; whilst the shear modulus determined from the crosshead movement gives a larger modulus value of 1249 MPa because transverse sensitivity effects are not corrected.

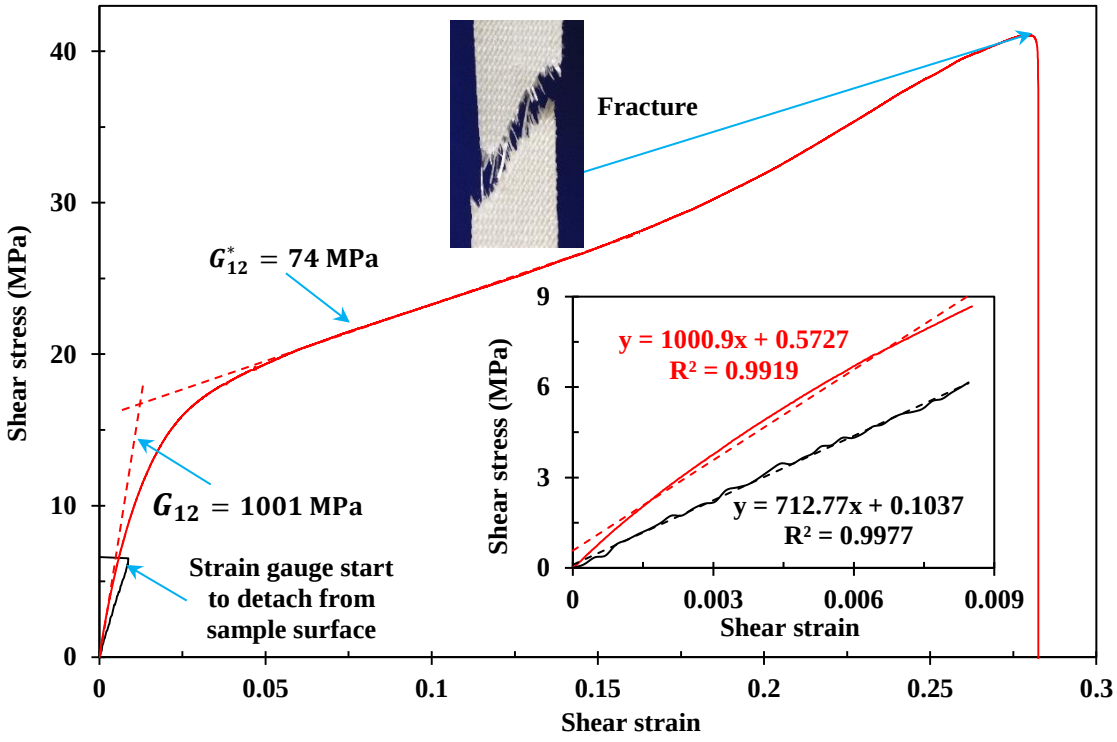

Figure 2-9 **Shear stress-strain curve of a [±45F]$_3$ composite sample, showing the shear stress-strain curves derived from both strain gauges (black) and crosshead movement (red).**

Table 2-5 **Shear properties of [±45F]$_3$ composite samples with strain gauges. SE is the ''standard error''.**

Sample	Shear modulus (MPa)			Shear strength (MPa)	Shear strain at failure (%)
	Strain gauge	Crosshead motion			
	G_{12}^{WC}	G_{12}^{WC}	G_{12}^{WC*}	τ_{12}^{WC}	γ_{12f}^{WC}
1	713	1001	74	41.06	27.99
2	847	1292	82	43.09	25.58
3	912	1453	84	42.74	27.19
Mean ± SE	824 ± 59	1249 ± 132	80 ± 3	42.30 ± 0.63	26.92 ± 0.71

2.4.4 Cross-section of composite layup

The cross-sectional content of GF/PP composite was evaluated from optical microscopy in both the warp and weft directions. Typical results are shown in Figure 2-10. Though the fibre count is the same in both directions, the tow geometry was found to be different. Table 2-6 gives the tow geometry of a single ply as measured by using FIJI [64], where a single woven lamina thickness was determined to be 0.205 mm.

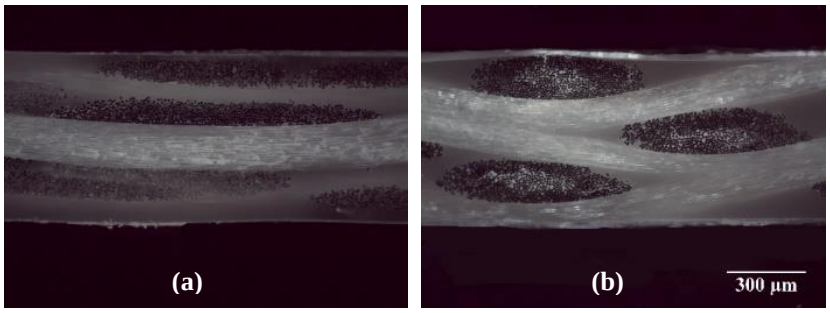

Figure 2-10 Cross-sectional area of composite layup in (a) warp and (b) weft directions.

Table 2-6 Tow geometry of the plain-weave GF in warp and weft directions.

Direction	Tow width (mm)	Tow height (mm)	Tow spacing (mm)
Warp	1.285	0.092	1.332
Weft	0.669	0.153	1.332

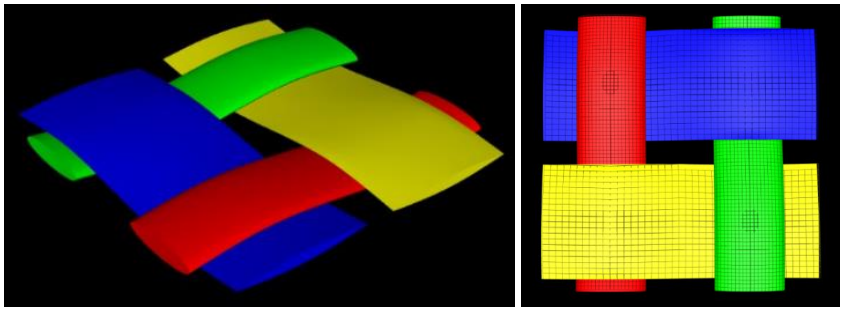

Figure 2-11 Unit cell model of plain-weave woven lamina reconstructed using TexGen [65], showing clearly the difference in tow geometry in warp and weft directions.

To clearly define the differences in tow geometry, a unit cell model of plain-weave woven lamina was established using TexGen [65], see Figure 2-11. The fibre tow in the warp direction is two times wider and around 70% smaller in thickness compared to weft fibre tow. For the

same fibre counts, the cross-sectional area of a single warp fibre tow is 20% smaller than the weft fibre tow. This is in accordance with the 24% difference in measured modulus values, and we can expect a more effective and collective response of fibres in the weft direction [66]. Thus, the tensile strength in weft direction is lower than warp direction, recall Table 2-4, and the discrepancy in modulus and Poisson's ratio in warp and weft directions from Section 2.4.2 are induced by different fibre tow geometries.

2.5 CONCLUSIONS

In this section, we have provided detailed studies on manufacturing the GF/PP based composite tape-spring samples. Trials on different composite layups provided useful guidelines and experiences for manufacturing, and the best performing sample had a layup of $[\pm 45F]_3$. Its mechanical properties were then characterised with embedded strain gauges, which gave reliable strain data after corrections of the transverse-sensitivity, compared to the crosshead motion. Though the fibre tows of the GF fabric in the warp and weft directions have a similar filament count, the tow geometry is found to be different, resulting in the discrepancy between moduli and Poisson's ratio values. These data provide a basic understanding of the composite material, and facilitate construction of the finite element model for composite tape-spring analysis in Section 3.

Section 3

FOLDING OF TAPE-SPRINGS

3.1 INTRODUCTION

Thin isotropic tape-spring (ITS) structures have been used, for example, to construct storable tubular extendible members (STEMs) [37] for space exploration. The most common ITS is made of steel, *i.e.* a tape-measure, or thin beryllium copper for spacecraft applications, which can be age-hardened using a heated cylindrical former [67].

Recall that every undeformed tape-spring is characterised by its transverse curvature $1/R$, uniform thickness t, subtended angle ξ and length L: the arc-length, b, is $R\xi$, see Figure 3-1-a. For a tape-spring with/without initial longitudinal curvature, bending to generate positive Gaussian curvature is recognised as equal-sense bending (ESB), Figure 3-1-b, whist negative Gaussian curvature corresponds to opposite-sense bending (OSB), Figure 3-1-c. During ESB, compressive stresses are induced along the tape edges, leading to flexural-torsional buckling and a series of edge kinks, which then coalesce into a single elastic fold. In OSB, tensile edge stresses are produced with higher deformation levels than ESB, before snapping through to form a fold. Once the elastic fold is well-developed, the bending moment is approximately constant in both cases [20].

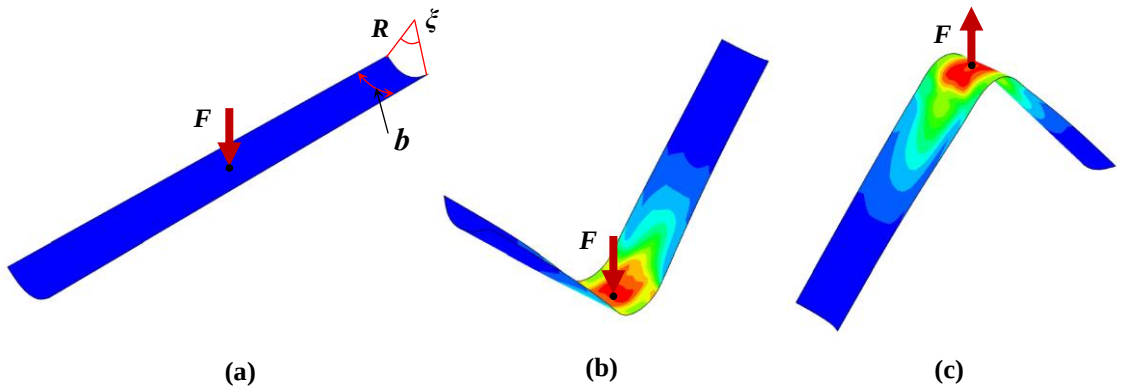

Figure 3-1 Schematic representation of a tape-spring structure: (a) geometry definition; (b) subject to equal-sense bending; (c) opposite-sense bending.

The analytical moment-rotation relationships for symmetrical tape bending have been well-understood [67]. Performing a similar practical experiment necessitates a bespoke and, hence, expensive bending rig, able to apply precise uniform bending moments and end rotations.

Because the ends must be securely held, the scope for torsional buckling during ESB, manifestly apparent during manual bending of a lengthy tape, is clearly reduced. Instead, we used a simpler three-point bending arrangement, schematically shown in Figure 3-2-a. Following the approximation as illustrated in Figure 3-2-b and c, the folded angle of a tape is approximately $2\psi = \sin^{-1}(2\delta/L)$.

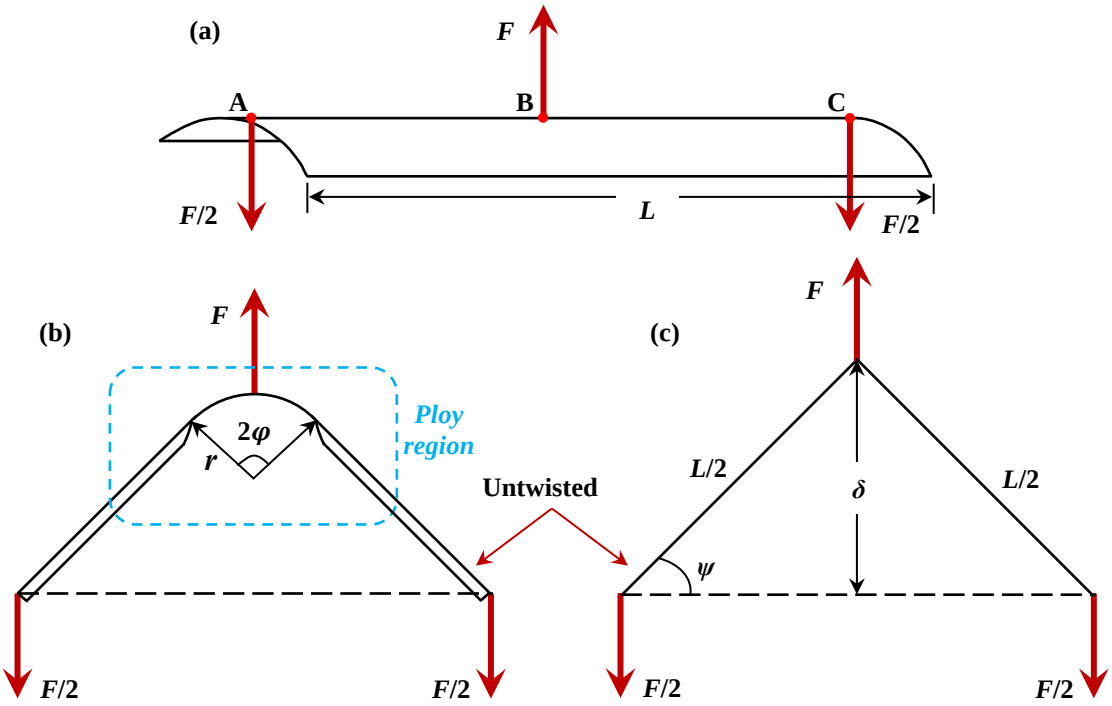

Figure 3-2 Schematic equal-sense bending of a tape-spring structure: (a) evaluation setup; (b) a typical shape in folding; (c) approximated shape to determine the folded angle.

In this section, we evaluate the folding behaviour of tape-springs. Unlike normal three-point bending, we establish a ‘‘free’’ bending setup with minimal end constraints, in order to promote torsional buckling more readily; folding of CTS samples is however investigated in terms of ESB only, since OSB causes damage and delamination to the composite material. For ITS, folding is studied in both ESB and OSB processes. FE models are also constructed using ABAQUS/Explicit [68] for both types of tape-springs, and compared to experiments.

3.2 EXPERIMENTAL FOLDING

CTS samples with different lengths and subtended angles, were fabricated following Section 2.3.2: Figure 3-3 shows some of the samples. ITS samples with different lengths were cut from a normal steel tape-measure.

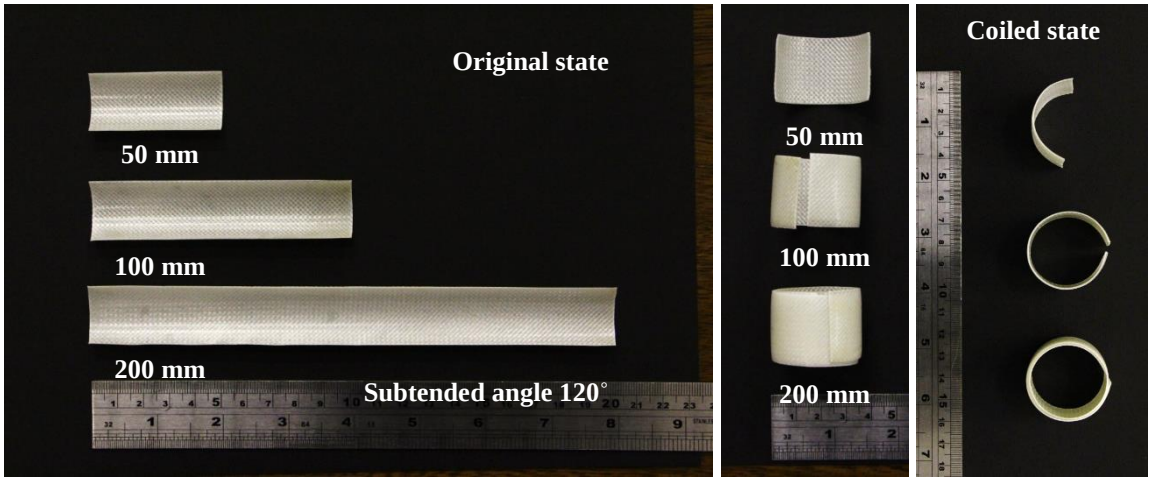

Figure 3-3 CTS samples with different initial geometry in their extended and coiled shapes.

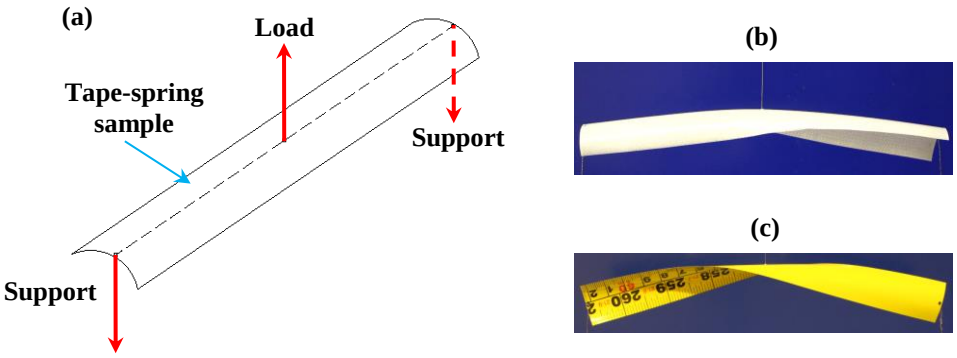

Figure 3-4 (a) Experimental setup for the folding tests of the tape-springs; (b) folding a CTS sample; (c) folding an ITS sample.

Figure 3-4 shows the schematic experimental setup, including the folded shapes of both CTS and ITS. Briefly, tape samples were connected to an Instron Serious 5564 materials testing machine using inextensible steel wires through centre-line longitudinal holes located at the ends and in the middle. During ESB, the outer two wires are anchored downwards, and the middle wired pulled upwards. The tape gradually deforms into a cylindrical central fold, connected by ‘‘ploy’’ regions to the two tape ends, which maintain with natural radius R. The applied force

is F, and the mid-point displacement is δ when the folded angle is 2ψ. Test data was recorded by a 100 N load cell as the cross-head moved at 60 mm/min. Both loading and unloading processes were monitored and each test cycle was performed three times, in order to evaluate repeatability.

3.3 FINITE ELEMENT MODEL

3.3.1 FE model for CTS

3.3.1.1 Micromechanics

There have been many attempts to model woven composites, documented well by Ansar *et al*. [69]. Their performances for specific purposes have been simulated through idealisation of geometric parameters and their weave architectures at a micro-structural level. However, their capabilities as geometrical models are limited to estimating the actual proportion of fibres in three, mutually orthogonal directions [69]. Lamers *et al*. [51] developed a macro-mechanical model for the **ABD** stiffness matrix of a woven laminate by considering the real tow geometry. It is complicated however by discretising the unit cell into elements and slices, which involves substantial computation; development of new mechanics and modelling methods are time-consuming and beyond the scope of this project.

Our woven composite is thus implemented using the modified Naik's model [55], where a woven composite ply has one isotropic matrix layer and two UD laminates, see Figure 3-5. We therefore capture layered information, which allows an investigation into the effects of the fibre angle.

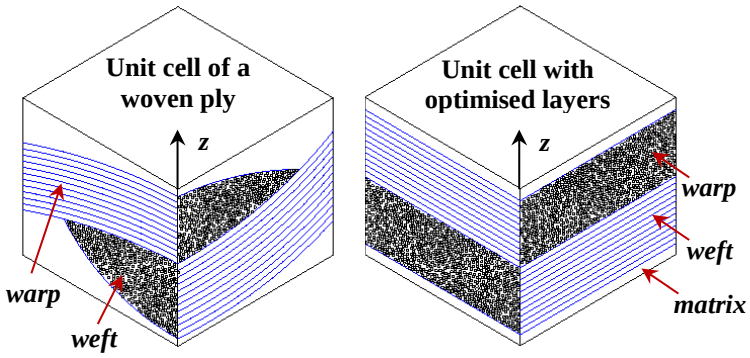

Figure 3-5 Schematic representation of the Naik's model [55], showing that one plain weave composite ply can be represented as one matrix layer and two unidirectional laminae.

Properties of the UD laminate were determined by mechanical tests and by the micromechanical model, from Section 2.2.1. The micromechanical model based on Hashin-Shtrikman (H-S) bounds [41] provides the theoretical basis; for plain weave lamina, its mechanical properties also depend on the yarn bundle geometry [55].

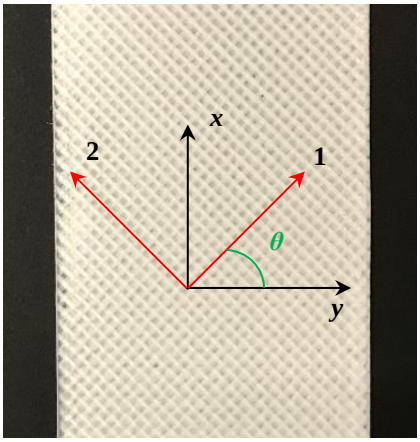

Figure 3-6 Coordinate system and fibre directions of the GF/PP woven composite: '1' denotes the fibre in warp direction; '2' is the fibre in weft direction; 'x' is along the sample length and 'y' is transverse; θ is the fibre angle of the woven composite, defined as $+\theta$ in warp and $-\theta$ in weft fibre.

Figure 3-6 shows the coordinate system and fibre directions of the GF/PP woven composite. In order to construct the FE model, the effects of fibre weaves and crimps are idealised, and the modulus values cannot be adopted directly from tests. Assuming instead that the longitudinal and transverse stiffness of a woven composite follow $E_{11}^{WC}: E_{22}^{WC} = a: b$, which can be measured experimentally, then:

$$E_{11}^{WC} = \frac{a}{b} E_{22}^{WC} = \frac{a}{(a+b)} (E_{\mathrm{HS}}^{1} + E_{HS}^{2}) \tag{3-1}$$

The modulus of the UD laminate in the warp (E_{11}^{warp}) and weft (E_{11}^{weft}) direction are then:

$$E_{11}^{warp} = \frac{a}{b} E_{11}^{weft} = \frac{a}{(a+b)} E_{\mathrm{HS}}^{1} \tag{3-2}$$

$$E_{22}^{warp} = \frac{a}{b} E_{22}^{weft} = \frac{a}{(a+b)} E_{\mathrm{HS}}^{2} \tag{3-3}$$

3.3.1.2 Viscoelasticity

The time-dependent viscoelasticity of the GF/PP composite also needs to be considered, which can be achieved by integrating the time-dependent relaxation modulus into the micromechanical model. The glass fibres are normally considered as elastic and isotropic, and viscoelastic effects are dominated by the fibres [30]. Considering a semi-crystalline polymer as a two-phase material, the instantaneous response to an external mechanical loading, as well as its load-bearing ability, is mainly determined by the crystalline response; while the time-dependent viscoelastic effects are developed in the amorphous regions [70]. The time-dependent viscoelasticity of polymers can be integrated using the experimentally determined stress relaxation modulus $\dot{E}_{\mathrm{m}}(t)$ at time *t*, which is usually described by a Prony series [30]:

$$\dot{E}_{\mathrm{m}}(t) = E_{\mathrm{m}} \left[1 - \sum_{i=1}^{N} k_{\mathrm{i}} (1 - e^{-t/\tau_{\mathrm{i}}}) \right] \tag{3-4}$$

k_{i} is the tensile relaxation coefficient; τ_{i} is the characteristic time; and *N* is the number of series terms. The corresponding relaxation shear modulus $\dot{G}_m(t)$ becomes:

$$\dot{G}_m(t) = \frac{E_{\mathrm{m}}}{2(1+v_m)} \left[1 - \sum_{\mathrm{i}=1}^{N} k_{\mathrm{i}} (1 - e^{-t/\tau_{\mathrm{i}}}) \right] \tag{3-5}$$

3.3.1.3 Construction of the FE model

The FE model was constructed using ABAQUS/Explicit [68] following Naik's idealisation [55]. The woven composite layup $[\pm 45\mathrm{F}]_3$ was simplified into a UD laminate with stacking

sequence [m/(45/-45)$_3$/m], where the m-ply was the pure PP matrix layer; the ply stack is shown in Figure 3-7-a. To determine the real thickness of each ply, optical microscopy was used to examine the cross-sectional area of a composite sample, Section 2.4.4. The thickness of the optimised UD layer was determined to be 0.1 mm, and the matrix layer was 0.025 mm. Properties of the UD laminae in the warp and weft directions were informed by tests and by the micromechanical model. Viscoelastic effects within a UD layer can also be optimised since its properties are dominated by fibres [30]: correspondingly, the Prony series for the matrix layer, Table 3-1, is implemented in ABAQUS using the results from Tscharnuter *et al.* [71].

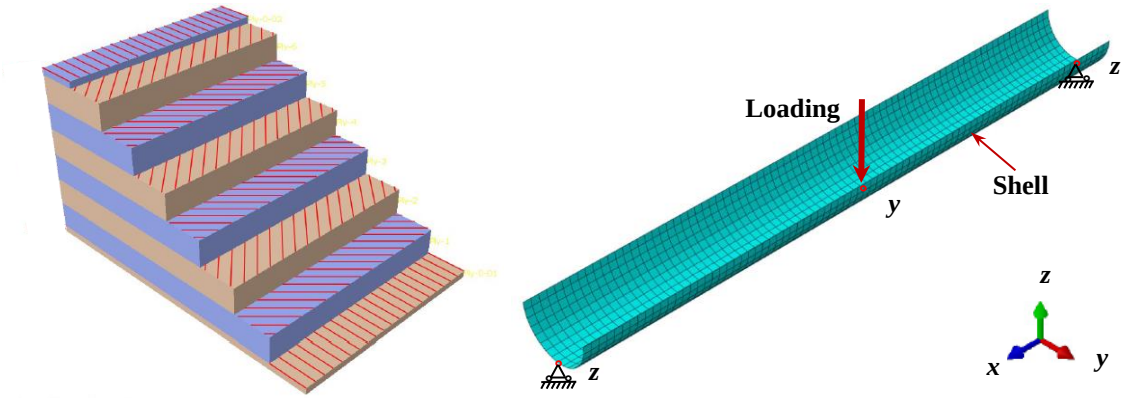

Figure 3-7 **Construction of the FE model: (a) composite layup adopted in the FE model; (b) boundary conditions applied in the model without the constraints of end rotations.**

Table 3-1 **Prony series coefficients of the PP matrix as adapted from Tscharnuter *et al.* [71].**

N	k_i	τ_i
1	3.26E-6	0.1
2	3.19E-5	1
3	6.39E-5	10
4	1.65E-4	100
5	2.79E-4	1000
6	5.03E-5	10000
7	2.19E-3	100000

The model used S4R reduced integration, four-noded shell elements coupled to hourglass control, finite membrane strains and a geometrically nonlinear analysis. The 'stabilize' function minimised instabilities according to a damping factor of 1×10^{-6}. Convergence studies on the mesh size were carried out to determine the acceptable accuracy of the model: an element edge size of 2 mm and around 2000 elements in total were found to be successful. Figure 3-7-b shows the constrained translational degrees of freedom in the model. Displacement restrictions

in the *z*-direction were applied to two nodes at the centre of cross-section at both ends; one node is able to move towards the other along the *x*-direction and a displacement restriction was also applied to the central node in the *y*-direction; no rotational constraints were applied. Folding is then achieved by displacing the central node of the shell in the *z*-direction.

3.3.2 FE model for ITS

The construction of an isotropic FE model is more straightforward. The properties of a typical steel tape-measure [12] are listed in Table 3-2. To determine the shell geometry, an image of the cross-section was loaded into DraftSight software [72] and scaled to the real size, Figure 3-8, which show that the sides of the tape-spring are flat. The effects of a polymer coating layer on the outside of the tape-spring were neglected in experiments since its modulus is several orders lower than steel; the coating was nonetheless removed by heat treatment in a fan-assisted oven to reveal the actual thickness of steel as 0.09 mm.

Table 3-2 Material properties of a steel tape-measure.

Materials	Steel tape-spring
Elastic modulus (GPa)	210
Poisson's ratio	0.3
Thickness (mm)	0.09

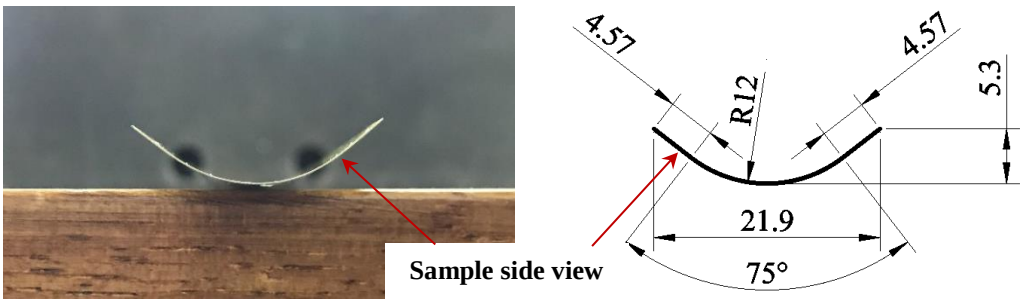

Figure 3-8 Model geometry for the FE analysis determined by measuring the real sample: (a) edge of a steel tape-spring sample; (b) dimensions (in mm) of shell for the FE model.

For a thin isotropic shell structure, transverse shear stress effects are negligible [73]. Thus, a 3-node triangular mesh, S3R element, was used rather than the S4R element for a CTS. A convergence study shows that an element size of 2.5 mm is appropriate for the analysis, and boundary conditions and solution process *etc*. as in Section 3.3.1.3 were also adopted.

3.4 FOLDING OF COMPOSITE TAPE-SPRINGS

3.4.1 Folding behaviour

Experiments were conducted on different CTS samples to evaluate their folding nature and the effects from geometry. Three sample lengths of 50 mm, 100 mm and 200 mm, with ξ equal to 120˚, 180˚ and 320˚, were considered. All samples were folded to an angle, 2ψ, of around 90˚, corresponding to a maximum loading displacement of 15 mm for samples 50 mm long, 30 mm for 100 mm long, and 70 mm for the 200 mm samples.

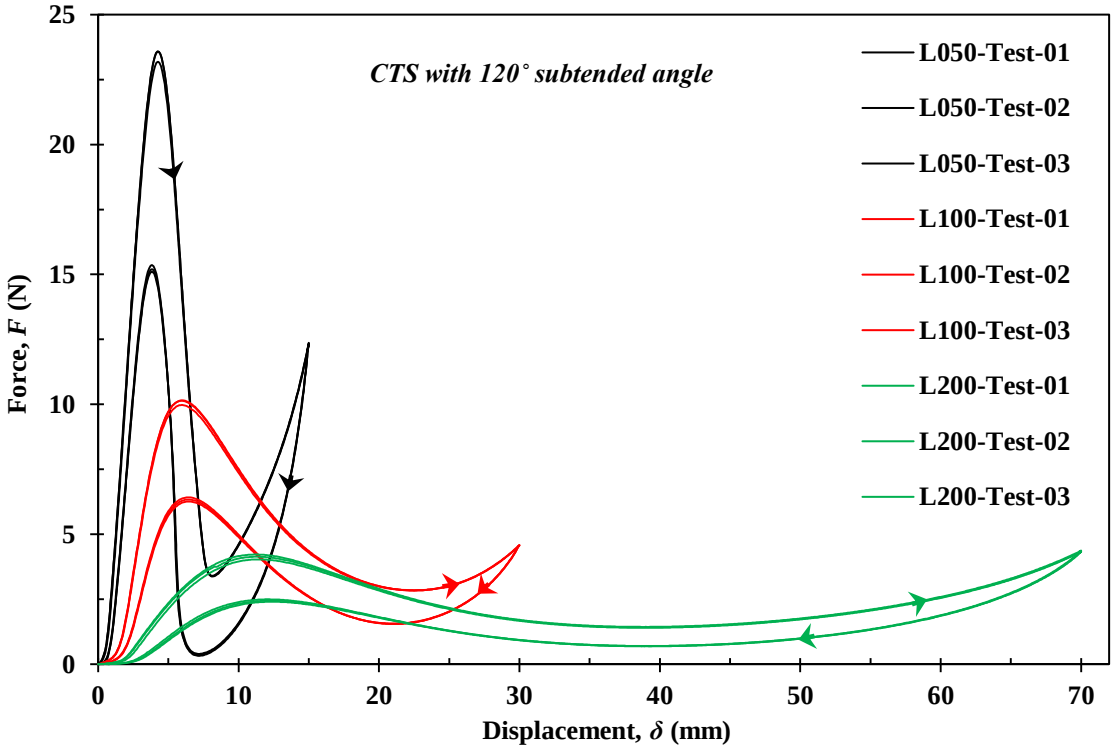

Figure 3-9 Force versus displacement during free bending of different length CTS samples.

Figure 3-9 shows the force-displacement relationship of a CTS sample with ξ = 120˚. Clearly, the peak force is larger for shorter samples, and is higher during loading than unloading in all cases. Such hysteresis may be due to the viscoelasticity of the GF/PP composite. It is observed also that bending is accompanied by torsional buckling, but the precise initiation point is not clear from the curves.

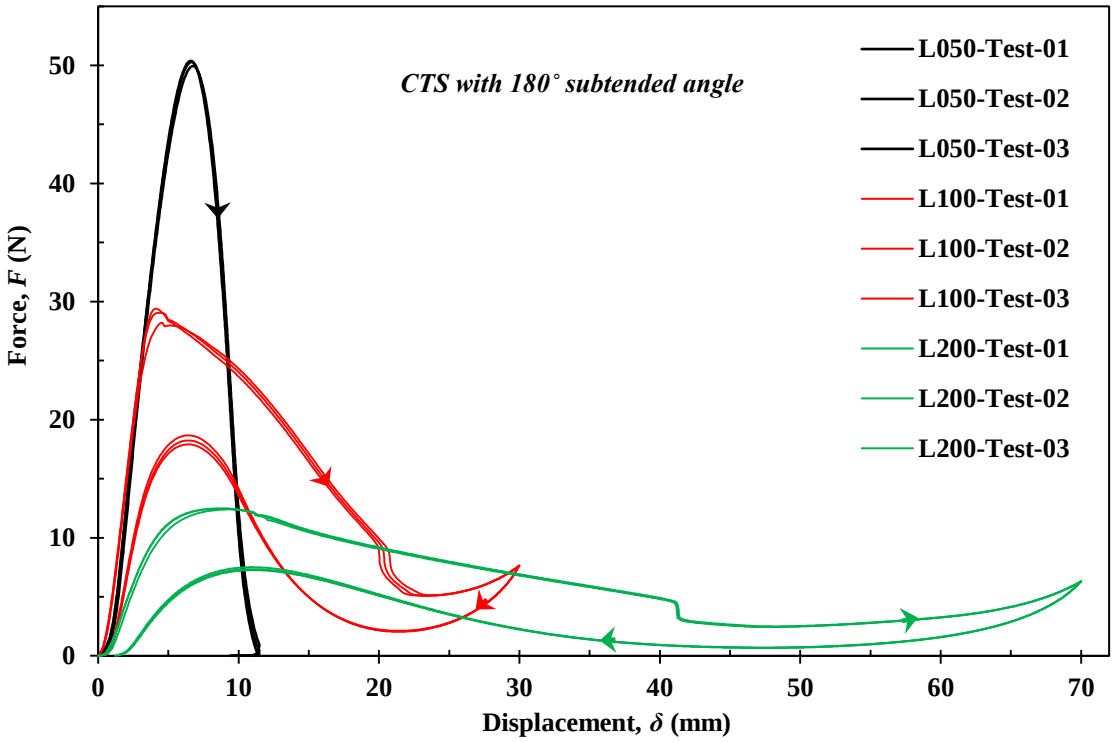

Figure 3-10 Force versus displacement during folding of different length CTS samples with a large ξ of 180˚ compared to Figure 3-8.

As similar behaviour is also observed for a CTS with ξ=180˚, in Figure 3-10. The applied load magnitudes all increase, and the 50 mm sample shows bistable folding. Experiments were also carried out for a CTS with ξ=320˚, but some were compromised by the steel wires falling at the support holes because the applied forces there were much larger. Table 3-3 summarises the experimental data on the peaks and valleys (first point of minimum force after the peak force) of different CTS samples; note that each test shows high repeatability.

Table 3-3 Experimental peaks and valleys in folding of CTS samples. SE is the standard error.

ξ (°)	L (mm)	Peak		Valley	
		F_{max} (N)	δ (mm)	F_{min} (N)	δ (mm)
120	50	23.19	4.26	3.40	8.16
		23.58	4.21	3.37	8.17
		23.59	4.24	3.39	8.14
	Mean ± SE	23.45 ± 0.13	4.24 ± 0.01	3.39 ± 0.01	8.16 ± 0.01
	100	10.15	6.00	2.69	22.50
		10.14	6.00	2.68	22.50
		9.97	5.97	2.68	22.37
	Mean ± SE	10.01 ± 0.06	5.99 ± 0.01	2.68 ± 0.01	22.46 ± 0.04
	200	4.22	11.20	1.43	38.70
		4.13	11.20	1.41	38.80
		4.03	11.43	1.40	38.93
	Mean ± SE	4.13 ± 0.05	11.27 ± 0.08	1.41 ± 0.01	38.81 ± 0.07
180	50	49.79	6.71	--	--
		50.17	6.59	--	--
		50.22	6.60	--	--
	Mean ± SE	50.01 ± 0.14	6.64 ± 0.04	--	--
	100	28.20	4.51	5.13	23.81
		29.05	4.40	5.09	23.46
		29.40	4.07	5.09	23.40
	Mean ± SE	28.88 ± 0.36	4.33 ± 0.13	5.10 ± 0.01	23.55 ± 0.13
	200	12.39	9.31	3.10	41.62
		12.48	8.97	3.24	41.42
		12.47	8.57	3.16	41.52
	Mean ± SE	12.45 ± 0.03	8.95 ± 0.21	3.17 ± 0.04	41.52 ± 0.06
320	200	35.02	24.68	18.65	51.81
		33.36	24.62	17.90	50.43
		30.71	24.61	16.79	50.48
	Mean ± SE	33.03 ± 1.26	24.64 ± 0.02	17.78 ± 0.54	50.91 ± 0.45

3.4.2 Validation of FE model

The FE model from Section 3.3.1 was used to offer further insights. Experimental data from Figure 3-10 were used to calibrate the model: though the viscoelasticity of matrix layer was considered, it is observed that the integration of Prony parameters of PP matrix in the model has marginal effects on the load profiles. The viscoelastic behaviour of the composite should have substantial effects during unloading, but the Prony series for a typical GF/PP system cannot be found in literature. Thus, only forward folding is simulated using the FE model. Figure 3-11 compares to experimental data, where there is clearly good agreement between the trends, but a major difference is the sharp peak from the simulation at the onset of initial

bending. This is due to a pronounced bifurcation when torsional buckling occurs, as highlighted by the insets. The torsional buckling also occurs in the experiments but this is more gradual owing to the presence of initial imperfections. Conversely, if the perfectly symmetrical boundary conditions are relaxed in the FE analysis, this peak is reduced in height and becomes rounder, as per experiments [63].

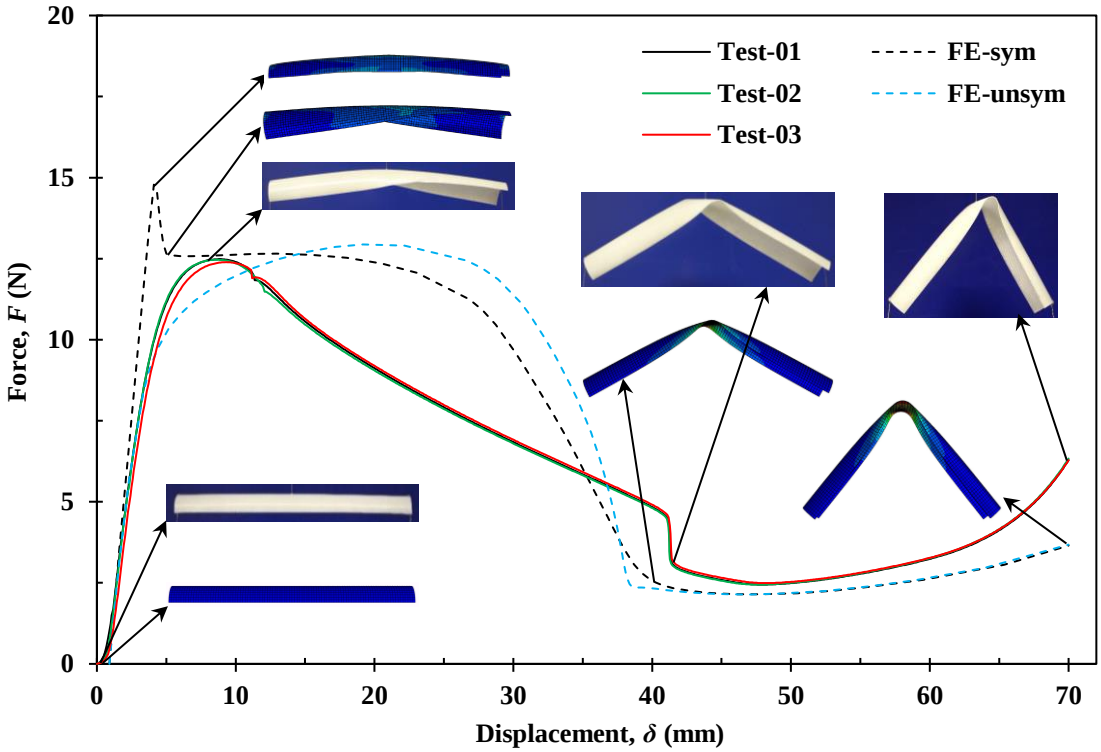

Figure 3-11 Force-displacement curves of the bistable CTS samples. Insets show the shapes at different stages from experiments and FE simulations (with/without symmetric boundaries).

Figure 3-12 shows further evidence of torsional buckling from the FE model by plotting the curvature changes of the central node of the tape shell against the displacement. Initially, there is pure bending in both *x*- and *y*-directions. The torsional coupling peak is clearly demonstrated by the sharp peak in transverse curvature change, χ_y, at around 3 mm. The tape then twists given by the increase in twisting curvature, χ_{xy}. Twisting reaches a maximum value at a displacement of 30 mm, then decreases. A minimum force is observed when the central fold region becomes transversely flattened as $\chi_{xy} \approx 1/R$, where twisting deformation is fully recovered.

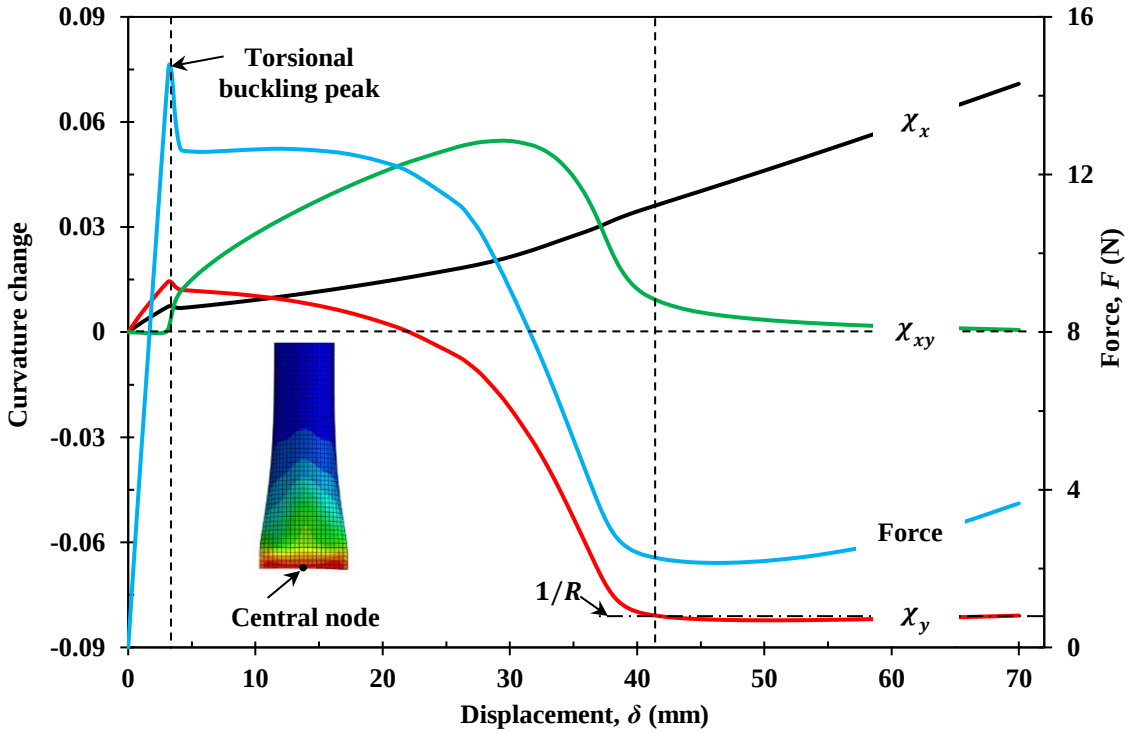

Figure 3-12 Curvature changes of the central node in longitudinal (χ_x), transverse (χ_y) and twisting (χ_{xy}) directions during the folding process.

3.4.3 Effect of tape length

Effects due to sample length are further evaluated from the theoretical analysis and FE model. Figure 3-13 shows the force-displacement curves from the FE model compared to the experimental data from Figure 3-10. Table 3-4 also compares the data at peaks and valleys from the FE model to the experimental data from Table 3-3. Generally, the FE model shows good agreement with experimental results in terms of force magnitude, while the corresponding peak positions are shifted by experimental imperfections, as discussed in Section 3.4.2.

Table 3-4 FE data on peaks and valleys during folding of CTS samples with different lengths, compared to experimental data in Table 3-3.

Subtended angle (˚)	Length (mm)	Peak		Valley	
		F_{max} ± SE (N)	δ ± SE (mm)	F_{min} ± SE (N)	δ ± SE (mm)
180	50	50.01 ± 0.14	6.64 ± 0.04	BEHAVES AS BISTABLE, VALLEY IS NOT FOUND	
	FE	51.67	4.10		
	100	28.88 ± 0.36	4.33 ± 0.13	5.10 ± 0.01	23.55 ± 0.13
	FE	29.77	2.59	4.17	17.64
	200	12.45 ± 0.03	8.95 ± 0.21	3.17 ± 0.04	41.52 ± 0.06
	FE	14.78	4.11	2.43	40.75

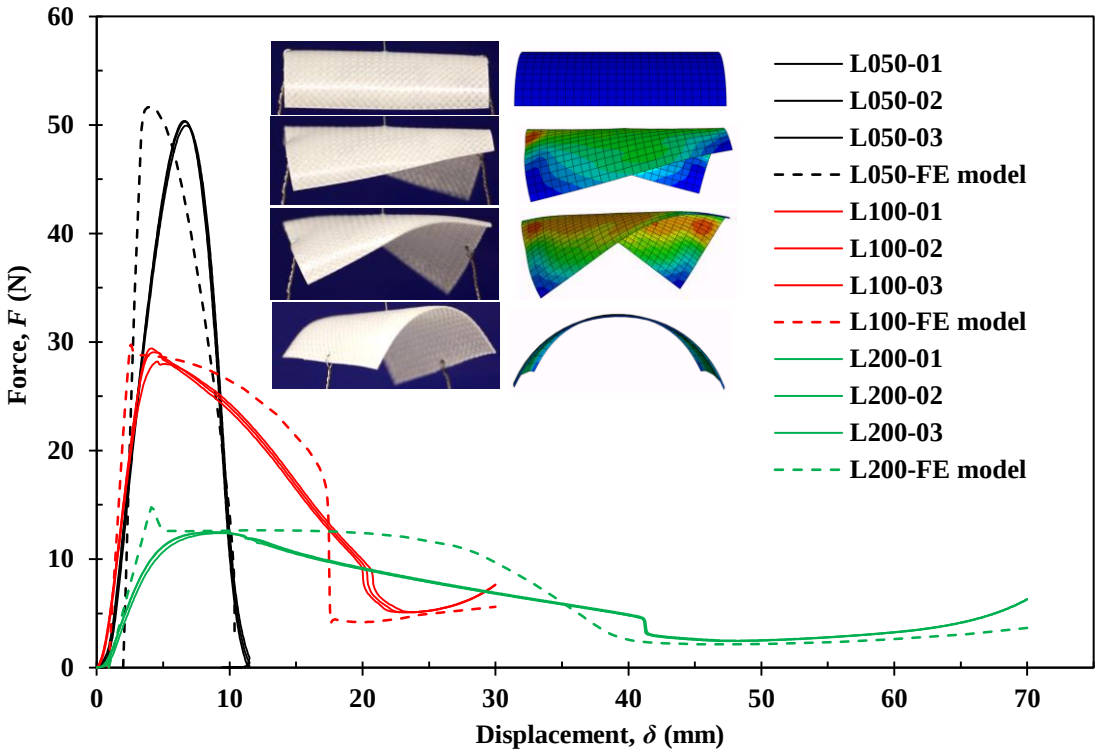

Figure 3-13 Force-displacement curves of the CTS samples with different sample length. The FE data are compared to those adopted from Figure 3-10; insets show shape changes at different stages for a CTS 50 mm in length.

3.4.4 Effect of subtended angle

We evaluate the effect of subtended angle for a fixed sample radius of 12.5 mm, where Figure 3-14 shows the force-displacement curves for different subtended angles. Clearly, the applied force magnitude increases with subtended angle, and various data points highlighted in Figure 3-14 are further plotted against subtended angle in Figure 3-15-a. First, Figure 3-15-a shows the change in critical buckling force; Figure 3-15-b then gives the initial slope and maximum force. Two data points are also adopted from the experimental curves in Figures 3-9 and 3-10.

By increasing the subtended angle, the critical buckling force as well as the maximum force increase linearly. The initial slope also increases as observed from both experiments and FE analysis, and then becomes stabilised beyond 230˚. This can be attributed to the increase in bending stiffness with subtended angle through the second moment of area [74].

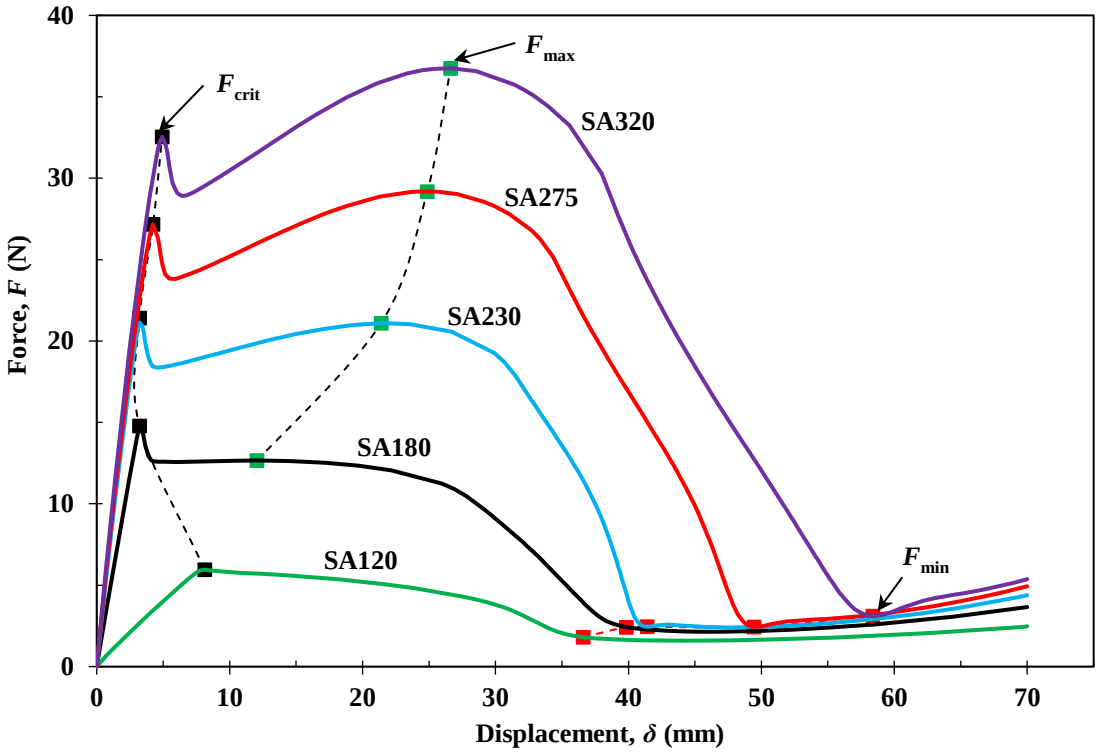

Figure 3-14 Force-displacement curves with different subtended angle obtained from the FE analysis with sample initial radius of 12.5 mm.

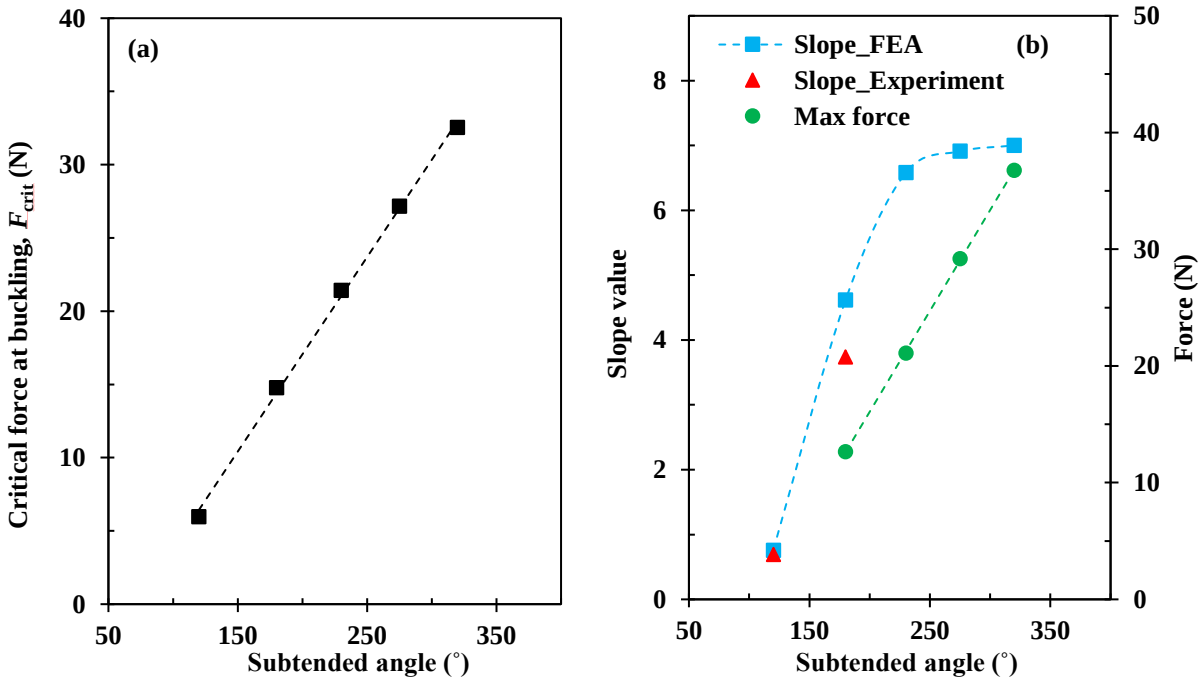

Figure 3-15 Changes of critical force at buckling, slope and maximum force with subtended angle. Initial radius is 12.5 mm and the length is 200 mm.

3.4.5 Effect of fibre angle

It is observed that the fibre angle profoundly affects the folding of a CTS, and FE analysis gives further insight. Figure 3-16 shows the evolution of the force profiles where the fibre angle clearly governs the shapes. Figure 3-17 details the changes of the buckling force, initial slope and maximum applied force: both the buckling and peak forces are maximised at a fibre angle of 45˚. The initial slope in each case reduces with increased fibre angle, which may be related to the modulus ratio in two-directions, requiring further investigation.

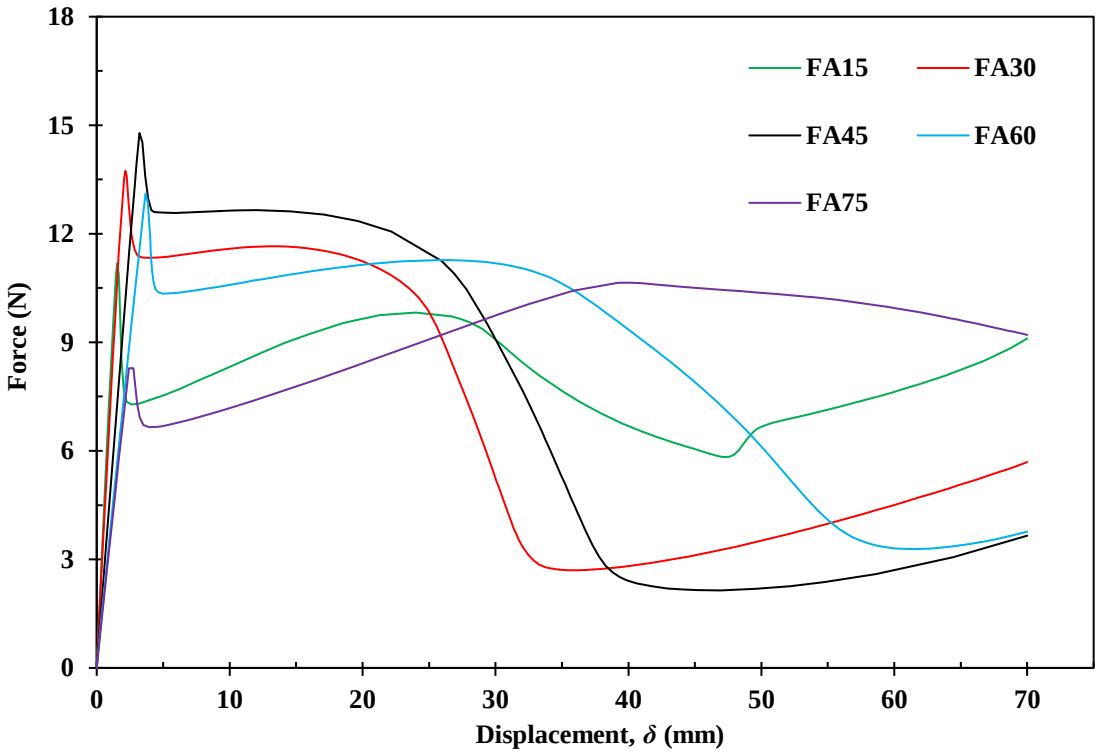

Figure 3-16 Force-displacement curves of the CTS samples with different fibre angle from FE analysis.

Experimental trials on folding a composite tube with a $[\pm 30F]_3$ layup gave a highly unstable twisted geometry. Finite element models also predict similar features: Figure 3-18 shows the twisting curvature at the central node for a folded tape shape with various fibre angles. It is noted that apart from the tape-spring with fibres oriented ±45˚, residual twisting of the samples are always observed.

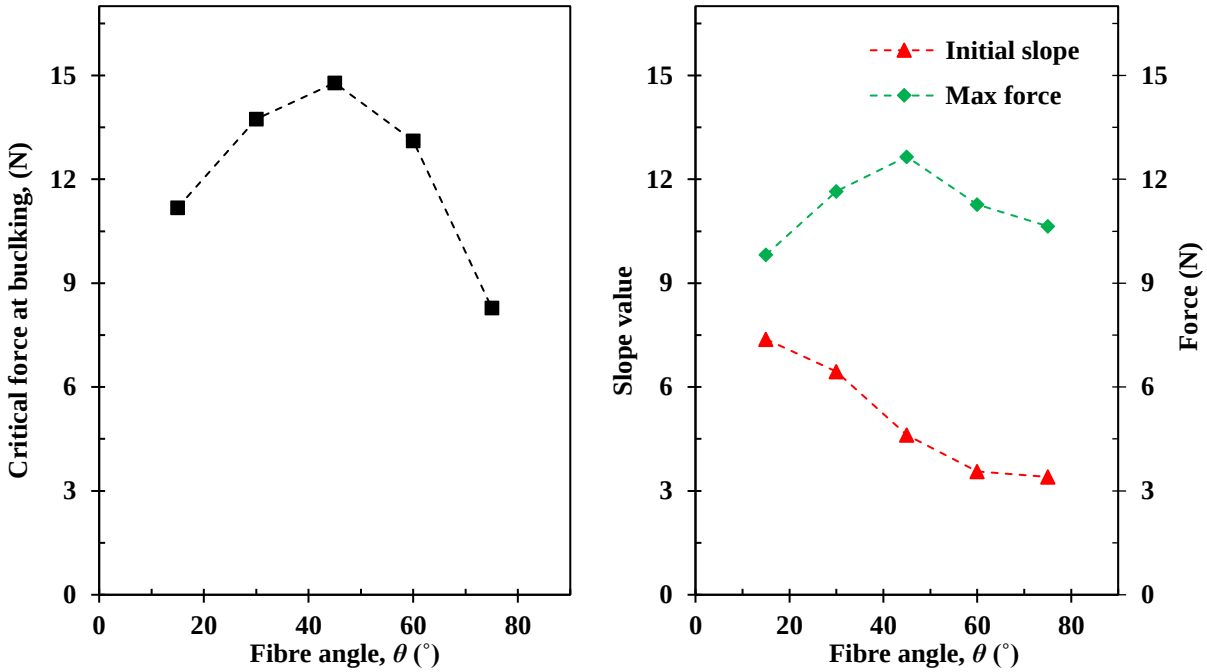

Figure 3-17 **Changes of critical force at buckling, initial slope and maximum force with fibre angle. Initial model radius is 12.5 mm, and length is 200 mm.**

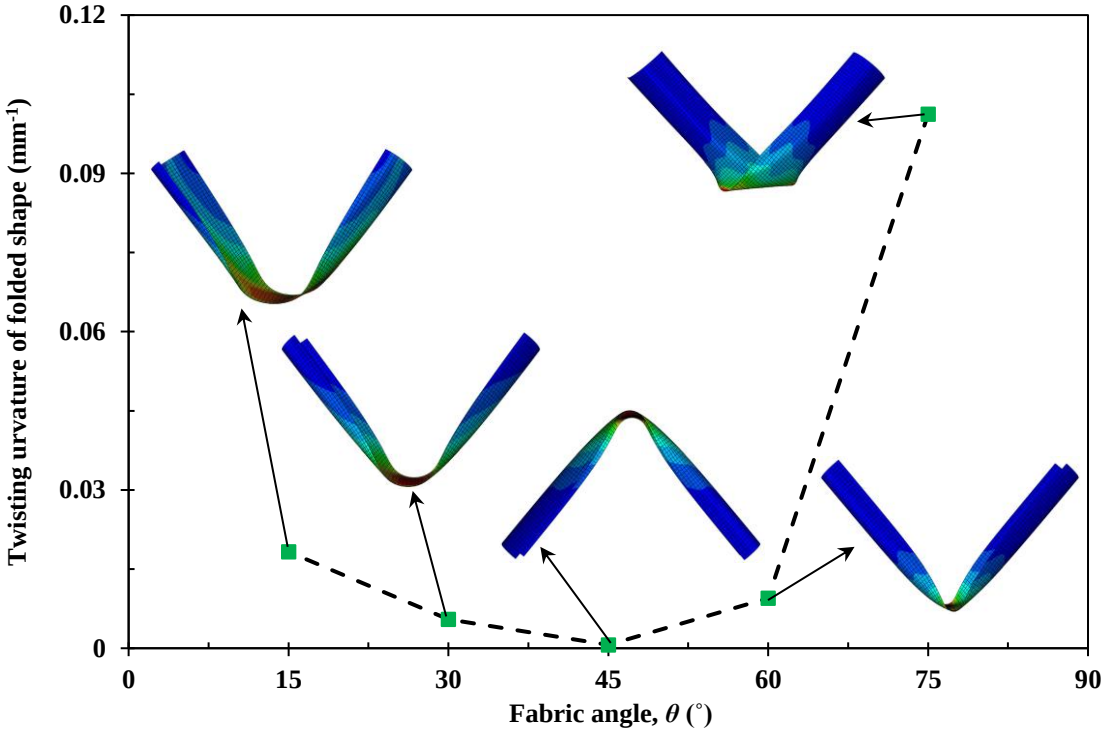

Figure 3-18 **Twisting curvature of the central node and the folded shape of a CTS, for different fibre angles.**

To evaluate the shape of the central folded region, each CTS with a different fibre angle was folded to around 180˚. The central circular region can be characterised by the longitudinal curvature change along the edge nodes, see Figure 3-19-a, and then by r and 2φ: see Figure 3-1-b. Figure 3-19-b shows the changes of r and 2φ, which all decrease with increased fibre angle. This implies that a CTS with a smaller fibre angle would have larger central fold radius.

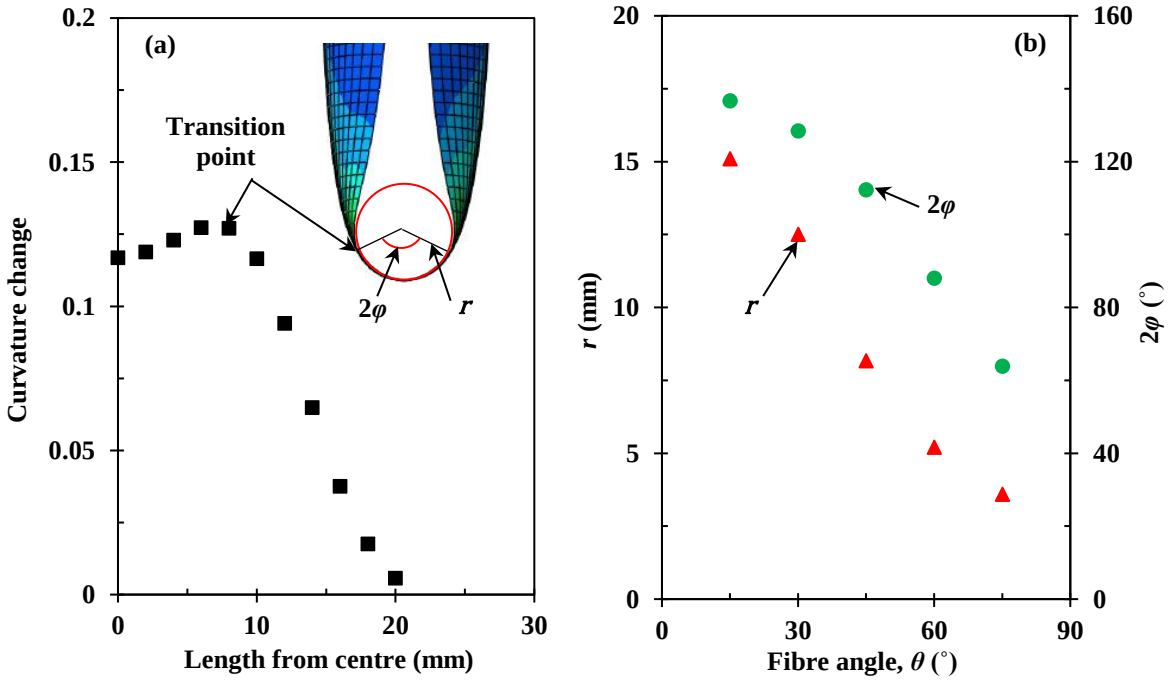

Figure 3-19 Characterisation of the central folded region: (a) longitudinal curvature change of a CTS with ±45˚ fibre angle; (b) changes of radius and central subtended angle with fibre angle.

3.5 FOLDING OF ISOTROPIC TAPE-SPRINGS

3.5.1 Folding behaviour

Figure 3-20 shows the force-displacement curves from the ESB cycles, where both the loading and unloading were monitored to a central displacement of 70 mm, corresponding to a relative folded angle of around 90˚. Different folding stages are characterised A to D as shown.

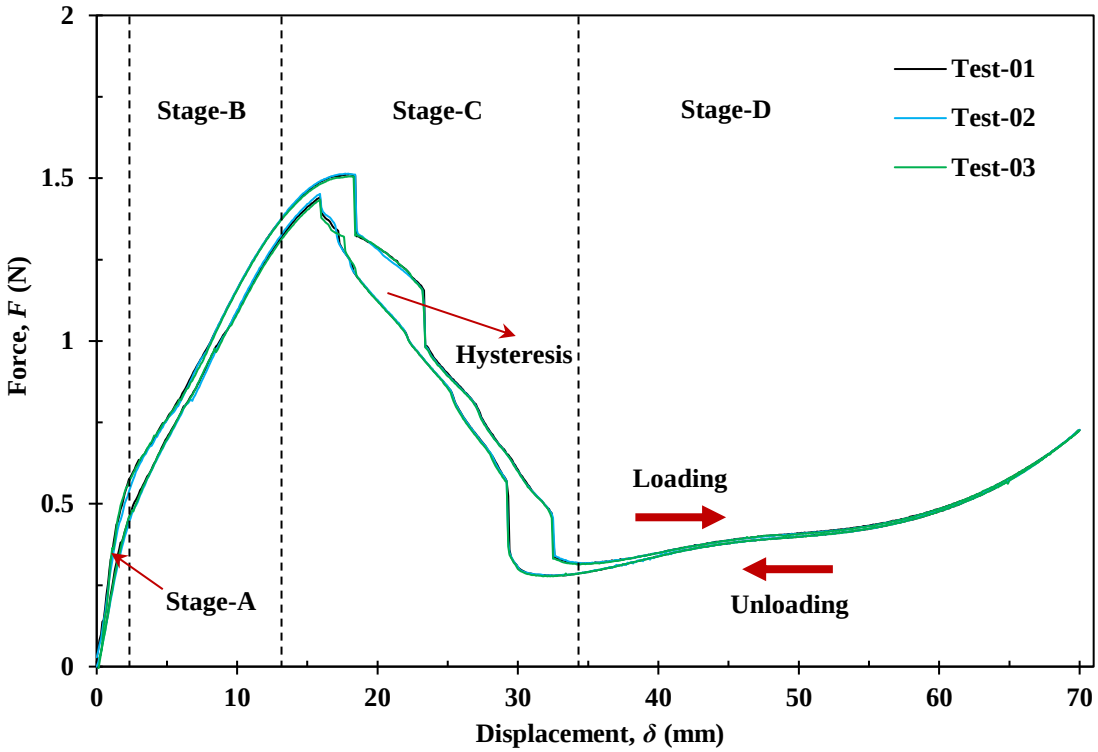

Figure 3-20 Experimental results of force versus displacement curves during ESB loading and unloading. Stages A-D characterise different deformation responses of the tape.

Similar to a CTS, torsional buckling develops with smooth and uniform deformation along the two tape edges in the longitudinal direction throughout Stage-A. Bending is accompanied by twisting deformation beyond the critical force, F_{crit}, at the onset of Stage-B, with a decrease in stiffness *i.e.* gradient. Stage-C is highly nonlinear where the twisting deformation becomes localised with a rapid reduction in applied force. Since experimental tests are not perfectly symmetric, the ‘‘kinks’’ form on one side of the tape before the other side, resulting in the step-like features in Figure 3-20. There is snapping when the two kinks then coalesce into one elastic fold as twisting reduces. The onset of Stage-D is characterised by a minimum force, a well-formed central fold with no twist, and a rising nonlinear profile. During unloading, the loading features are totally reversible, expect for some hysteresis where the loads are slightly lower. The loading process is thus our main focus: Stages-A and B can be treated as a small displacement regime, and Stage-D is regarded as large displacement. Detailed analysis is discussed later.

Opposite-sense bending (OSB) of an ITS is also evaluated using the same setup, and Figure 3-21 shows the force-displacement curves. Unlike the ESB, there is no bending-torsional buckling during OSB, but there is a major snap-through/snap-back peak as highlighted by the inset figures.

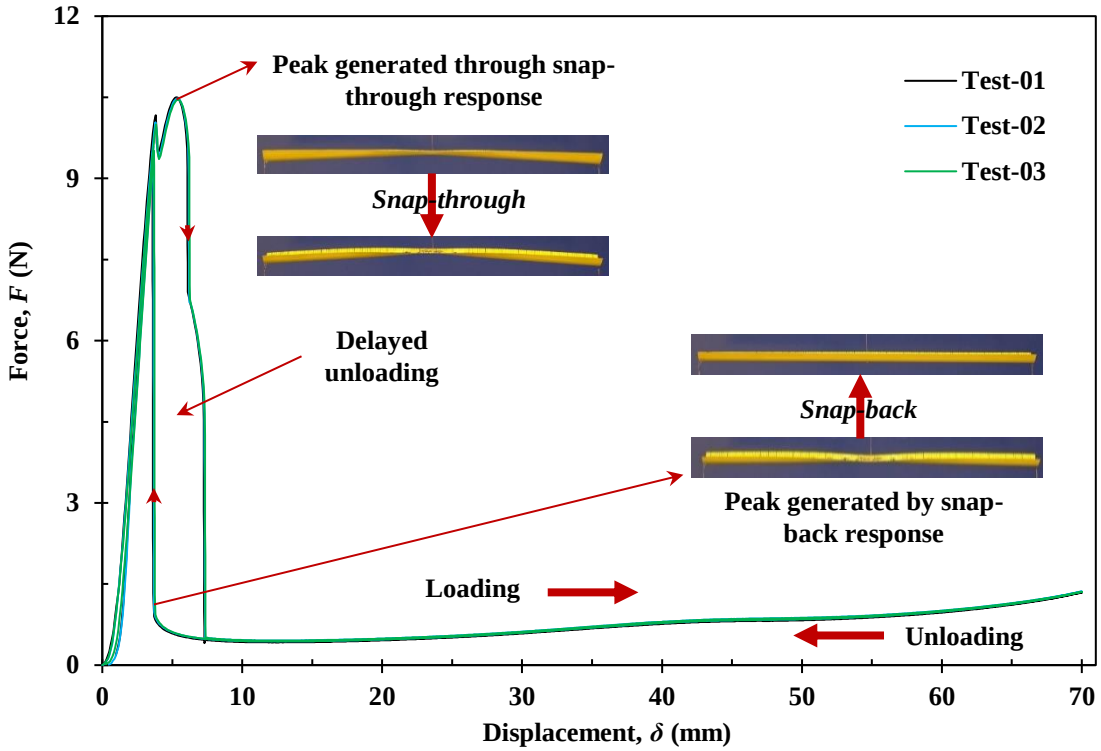

Figure 3-21 Force versus displacement curves during the OSB loading and unloading. Insets show corresponding tape shapes.

3.5.2 Validation of FE model

Figure 3-22 compares the FE analysis to experiments where, in general, there is good agreement. The major difference is a sharp peak at the onset of loading in the FE model during Stage-A, which corresponds to coupling of bending and torsion for perfectly symmetrical boundary conditions, which is not realised in experiments. By employing an offset (shifting the constrained node by an element size of 2.5 mm) to the boundary constraints in the model, the peak vanishes, and gives a nearly perfect fit to the experiments, see Figure 3-22. A minor difference appears in Stage-C where, unlike the step-like snap processes from Section 3.5.1, the simulated force gradually reduces and is followed by a major snap-through response. This is also caused by the perfect symmetry BCs in the model as the localised kinks occur simultaneously on both sides of the tape. The discrepancy can also be attributed to the differences in sample attachment methods between experiments and FE model, since the steel wires do not remain vertical under large displacements.

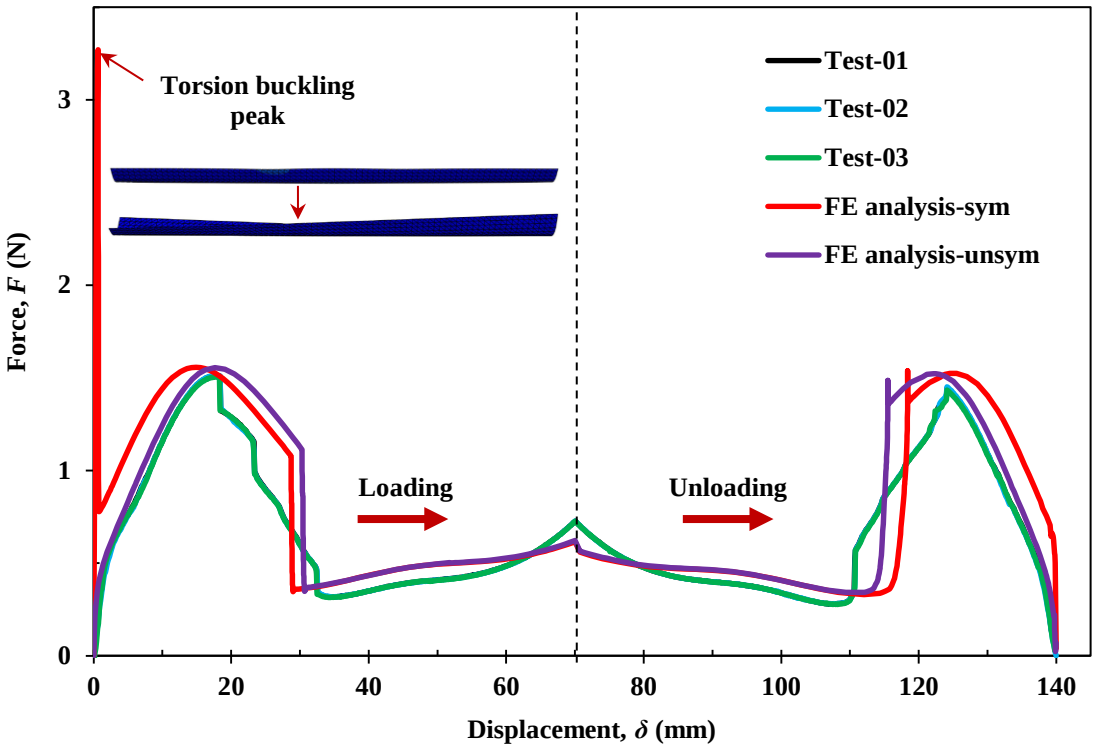

Figure 3-22 **Force versus displacement curves from FE during loading and unloading with and without the symmetrical boundary condition, compared to the experimental results.**

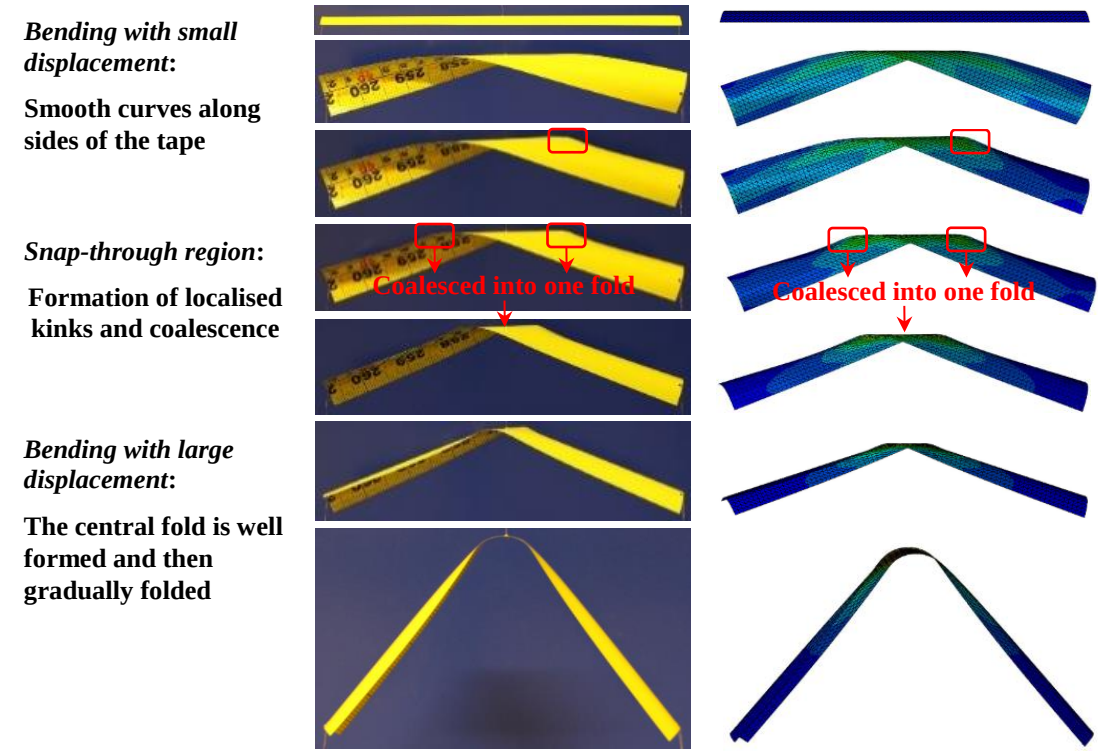

Figure 3-23 **Real tape-spring deformation compared to the deformed shapes from the FE model during ESB.**

Figure 3-23 also shows the actual deformed shapes at different stages, directly compared to the FE model. Figure 3-24 shows the results compared to experiments. It is clear that the FE model successfully captures the main features from both ESB and OSB processes.

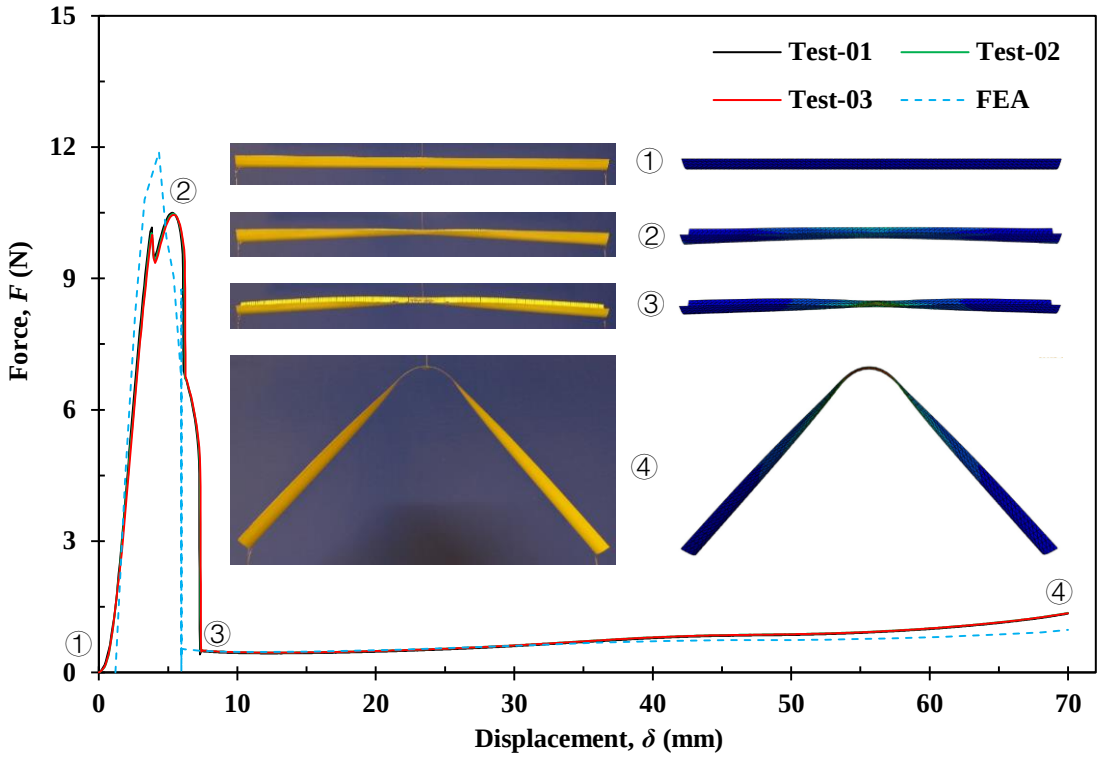

Figure 3-24 Force versus displacement curves during the OSB loading from the FE model, and experimental results.

3.5.3 Effect of tape length

Opposite-sense bending of an IST is analogous to previous findings [20], but ESB is quite different. To simulate the free ESB folding of an ITS, imperfections in the FE model are needed. Further experiments were conducted on IST samples with different lengths of 50 mm, 100 mm, and 200 mm, folded to an angle of around 80˚, and Figure 3-25 compares to FE results. Again, there is good agreement. In general, the maximum force occurs at a folded angle of around 20˚, then decreases with localisation along the edges. The tape snaps into a simple fold at the centre, where twisting buckling disappears and the folding region is considered as well formed with minimum force. The corresponding fold angle for minimum force increases as the length decreases, see Figure 3-25.

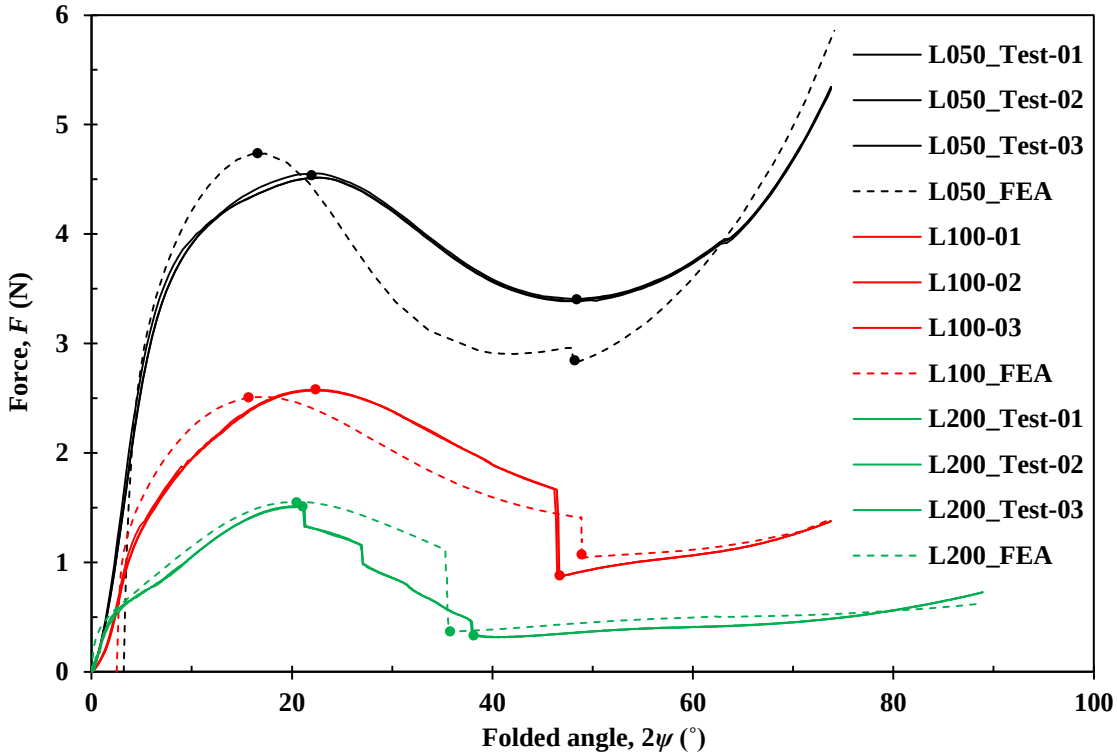

Figure 3-25 **Force-displacement curves of the isotropic tape-springs in ESB with different lengths. The FE data are compared to those adopted from Figure 3-22; dots show the maximum and minimum force locations.**

Table 3-5 **Maximum and minimum force positions extracted from the data dots highlighted in Figure 3-25.**

Length (mm)	Maximum force position		Minimum force position	
	F_{max} ± SE (N)	Folded angle (˚)	F_{min} ± SE (N)	Folded angle (˚)
200-ESB	1.512	20.75	0.334	38.19
	1.513	20.63	0.339	38.19
	1.505	20.75	0.330	38.19
Mean ± SE	1.511 ± 0.003	20.71 ± 0.04	0.334 ± 0.003	38.19 ± 0.00
FE model	1.554	20.35	0.347	35.78
100-ESB	2.577	22.15	0.870	46.66
	2.570	22.38	0.876	46.68
	2.575	22.38	0.873	46.68
Mean ± SE	2.574 ± 0.002	22.31 ± 0.08	0.873 ± 0.002	46.67 ± 0.01
FE model	2.511	17.60	1.019	48.94
50-ESB	4.51	22.76	3.384	48.33
	4.52	22.66	3.391	48.23
	4.55	22.52	3.405	48.08
Mean ± SE	4.53 ± 0.01	22.65 ± 0.07	3.394 ± 0.006	48.22 ± 0.07
FE model	4.735	17.36	2.821	48.08

To further characterise the effects induced by sample length, the maximum and minimum force data in Figure 3-25 were extracted and shown in Table 3-5. It gives a good agreement in predicting the peak positions but there is a larger variation in the minimum force positions.

3.6 CONCLUSIONS

We have evaluated the folding nature of tape-springs made from isotropic and orthotropic materials. The composite tape-springs were manufactured following Section 2; the isotropic tape springs were cut from a tape-measure. We have clearly observed torsional buckling and instability during folding for both. The FE model has been developed to study the folding in more detail, and has been calibrated by experimental results in each case. The model provides good agreement and captures the main features for both types of tapes. Torsional buckling occurs during equal-sense bending. The length and subtended angle control the load magnitudes, while the overall folding behaviour follows similar stages. From these observations for both isotropic and composite tape-springs, the structural behaviour of tape-springs is further discussed and analysed in Section 4.

Section 4

STRUCTURAL BEHAVIOUR

4.1 INTRODUCTION

The folding behaviour of a tape-spring structure is highly nonlinear and directionally dependent [20]. The analytical moment-rotation relationships for symmetrical tape bending have been developed by Rimrott [75], Calladine [52], Mansfield [76] and more recently by Seffen [67]. Unsymmetrical bending characterised by tape twisting has been studied also by Mansfield in consequence to uniform equal-sense bending and buckling in a torsional mode. These provide the basis for analysis of the folding observations in Section 3.

The elastic folding of an ITS is very well understood but there is little work on folding of a CTS. In folding of an ITS, it eventually buckles to form a localised folded region that is approximately curved uniformly in the longitudinal direction, with a radius of curvature almost equal to the transverse radius of the undeformed cross-section [21]. An alternative concern is the torsional buckling and instabilities observed in the bending of tape-springs. Coupled torsional-bending buckling of a tape-spring was first explained by Mansfield [77] for an ITS, while orthotropic was not covered.

For aircraft landing gear applications, we want to capture torsional buckling as this limits the applied force during initial folding; we then analyse the large displacement folding.

4.2 FOLDING OBSERVATIONS

Figure 4-1 schematically shows a typical force-displacement profile for ESB folding of a tape-spring structure, either isotropic or orthotropic. The tape ends are free to rotate and to approach one another but are restrained linearly against the centrally applied, vertical force, F. In summary, four stages of deformation are observed as demonstrated in Section 3, briefly: Stage-A is initial, symmetrical bending with smooth and uniform deformation along the tape; Stage-B commences when torsional buckling initiates with a critical force, F_{crit}, and twisting deformation gradually follows. Following a maximum force, F_{max}, twisting then diminishes

during Stage-C as the fold begins to localise and become well formed as the applied force drops. A minimum force, F_{min}, is then expressed at the onset of Stage-D where the curved fold is complete and central, and separated by transition, *i.e.* ploy regions (characterised in Section 5) on either side: "point-like" folding then proceeds under increasing force.

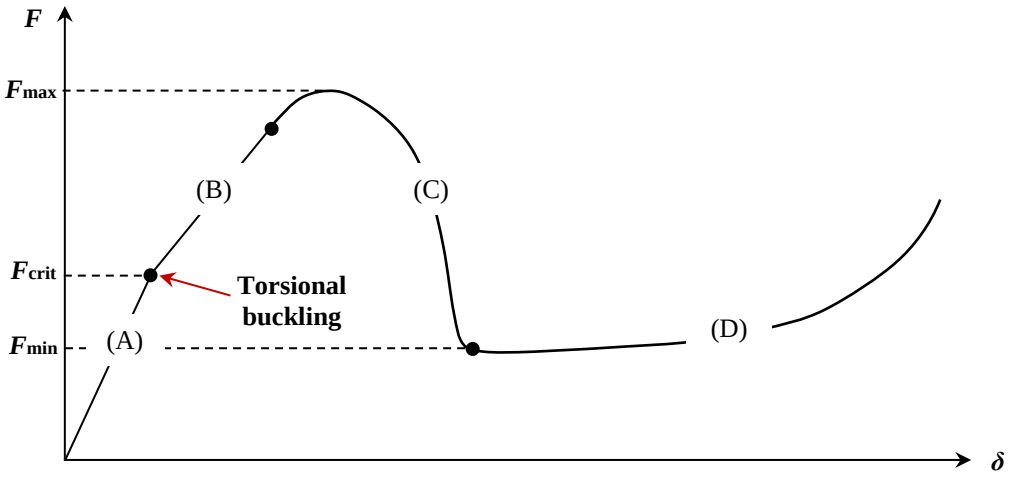

Figure 4-1 Schematic representation of force-displacement in equal-sense bending of a tape-spring structure.

4.3 TORSIONAL BUCKLING

4.3.1 Theoretical analysis

Coupled torsional-bending buckling of a tape-spring was first explained by Mansfield [77]. The tape has to be thin-walled and sufficiently curved initially, and carries a uniform bending moment along its length. The product of initial orthogonal curvatures, or Gaussian curvature, builds up as the original cross-section flattens, resulting in the well-known build-up of in-plane middle surface forces from Gauss's Theorema Egregium [52]. Sustaining ever larger in-plane forces is, however, not possible indefinitely, and buckling in a torsional mode enables a developable response for continued bending with no further change in Gaussian curvature. Mansfield predicts a constant applied moment during post-buckling even though the axial curvature increases; the level of twisting rises and then falls to zero as the tape loses more transverse curvature, before becoming cylindrically curved along its length - features we have seen in our three-point bending tests.

Mansfield's analysis assumes uniform twisting and axial curvatures in order to solve for the non-uniform transverse curvature change across the width of tape. He produces a fourth-order governing differential equation by considering transverse moment equilibrium and geometrical compatibility from the change in Gaussian curvature. Three-point bending here produces a length-wise bi-linear bending moment, which renders a closed-form solution intractable by the same approach. As a first approximation by analogy, we can set the peak bending moment in the middle of the tape equal to Mansfield's applied moment, thence his torsional buckling bending moment: setting peak stresses in thin-walled structures equal to known local buckling stresses, is often performed.

But we wish to consider orthotropic tape-springs, which Mansfield does not. They are studied by Giomi and Mahadevan [79] but they do not cover torsional buckling. To simplify matters, we remark that the onset of buckling is "early" in the loading cycle where the amount of transverse flattening is practically zero compared to the axial curvature change, χ_x. We therefore assume no initial flattening and no *y*-direction variation, with only uniform curvatures throughout, setting up an algebraic rather than a differential analysis. The simplest formulation is thus energetic, and considers bending and stretching components of strain energy, with the two becoming coupled by the change in Gaussian curvature; and because of uniform curving, the stored energy can be calculated per unit length of tape. The tape is already twisted and curved in order to find the initiation conditions for torsional buckling.

For current values of curvature equal to κ_x, κ_y and κ_{xy}, the Gaussian curvature is defined by $\kappa_x\kappa_y - \kappa_{xy}^2$ [52]. The initial transverse curvature is $\kappa_{y0} = 1/R$, which remains fixed, setting $\kappa_y = 1/R$ from $\chi_y = \kappa_y - \kappa_{y0} = 0$. Gauss's Theorema Egregium also yields the formal relationship between in-plane strains and the change in Gaussian curvature [52]:

$$-\frac{\partial^2 \epsilon_x}{\partial y^2} - \frac{\partial^2 \epsilon_y}{\partial x^2} + \frac{\partial^2 \gamma_{xy}}{\partial x \partial y} = \left(\kappa_x\kappa_y - \kappa_{xy}^2\right) - \left(\kappa_{x0}\kappa_{y0} - \kappa_{xy0}^2\right) \tag{4-1}$$

Axial strains, ϵ_x, are dominant, and the initial curvatures, κ_{x0} and κ_{xy0}, are zero. Integrating with respect to *y*, we therefore arrive at an expression for ϵ_x, including constants of integration. The net axial force due to stresses σ_x must be zero, dictating that $\int t\sigma_x \, dy = 0$ across the width

of cross-section. For a constant thickness *t*, then $\int \epsilon_x \, dy = 0$ is also true, enabling the constants to be found. The final strain expression is [53]:

$$\epsilon_x = -\frac{1}{2} \cdot \frac{\kappa_x}{R} \cdot \left(y^2 - \frac{b^2}{12} \right) + \frac{1}{2} \kappa_{xy}^2 \left(y^2 - \frac{b^2}{12} \right) \tag{4-2}$$

The right-hand side deliberately conveys two specific components. The first is the "beam" bending part, for a parabolic-shaped cross-section, which is the shallow shell approximation for being uniformly curved; there is compression in the outer fibres, at $y = \pm b/2$, and tensile strain in the middle. The second is due purely to twisting, resulting in tension this time in the outer fibres: if we imagine the edges of deformed tape gently modulating on a helical path, they must be longer than, say, the central fibre, which remains straight.

Twisting therefore offsets compressive strains on the edges, and vice versa in the middle of the tape; but also, the Gaussian curvature before twisting is initiated, κ_x/R, is defrayed by the action of κ_{xy}^2, which reduces ϵ_x. So we expect κ_{xy} to emerge as a buckling consequence and the Gaussian curvature at buckling to be conserved.

The strain energy in stretching per unit length, $\overline{U}_s$, is given by integrating Eq. 2-60 across the width after substituting for ϵ_x, all other strain terms being zero, *i.e.*:

$$\overline{U}_s = \int_{-b/2}^{b/2} \frac{Et}{2} \cdot \epsilon_x^2 dy = \frac{Etb^5}{1440} \left(\kappa_{xy}^2 - \frac{\kappa_x}{R} \right)^2 \tag{4-3}$$

For the equivalent in bending, $\overline{U}_B$, only κ_x and κ_{xy} contribute to Eq. 2-62; the parameter β is remiss, but the orthotropic torsional rigidity, α, now appears, with $\overline{U}_B = \int (D/2) \cdot (\kappa_x^2 + 2\alpha\kappa_{xy}^2) dx dy$. The total strain energy per unit length, $\overline{U}$, combines these terms, which can be written as [53]:

$$\overline{U} = \frac{Db}{2} \left[\kappa_x^2 + 2\alpha\kappa_{xy}^2 + \phi \left(\kappa_{xy}^2 - \frac{\kappa_x}{R} \right)^2 \right] \tag{4-4}$$

with

$$\phi = b^4(1 - v^2/\beta)/(60t^2) \tag{4-5}$$

Equilibrium configurations stem from energy minima with respect to the appropriate curvature [80]. Despite twisting curvature, no axial torque is applied and $\partial\overline{U}/\partial\kappa_{xy} = 0$, yielding two solutions:

$$\kappa_{xy} \cdot \left[\alpha + \phi\left(\kappa_{xy}^2 - \frac{\kappa_x}{R}\right)\right] = 0 \quad \rightarrow \quad \kappa_{xy} = 0, \qquad \kappa_{xy}^2 - \frac{\kappa_x}{R} = -\frac{\alpha}{\phi} \tag{4-6}$$

The first, $\kappa_{xy} = 0$, is initial bending; the second shows non-zero twisting and a fixed amount of positive Gaussian curvature, α/ϕ, provided $\kappa_x > R\alpha/\phi$.

The applied moment, *M*, (in the same direction as M_x) is equal to $\partial\overline{U}/\partial\kappa_x = 0$ because $\overline{U}$ is formulated per unit axial length [76], returning $Db \cdot \left[\kappa_x - (1/R) \cdot \phi \cdot \left(\kappa_{xy}^2 - \kappa_x/R\right)\right]$. Substituting for each solution captures the initial and buckled bending responses with:

$$M_A = Db \cdot [1 + \phi/R^2] \cdot \kappa_x \quad \text{or} \quad M_B = Db \cdot [\kappa_x + \alpha/R] \tag{4-7}$$

They are valid only when each configuration is strictly stable, which is assessed from the eigenvalues of the Hessian stiffness matrix for $\overline{U}$ [81]. As a result, the first *M* is valid up to $\kappa_x = R\alpha/\phi$, and the second for κ_x larger.

Both express linear curvature responses, with the second including an intercept. When plotted together we see a bi-linear profile with an abrupt change in gradient at $\kappa_x = R\alpha/\phi$; at this point, we have our critical buckling moment, $M = Db \cdot (R\alpha/\phi) \cdot [1 + \phi/R^2]$. This moment correlates to $F_{\text{crit}}L/4$ for our critical three-point loading force, F_{crit}, when applied centrally over span *L* [53]:

$$F_{\text{crit}} = \frac{4Db}{L} \cdot \frac{R\alpha}{\phi} \cdot [1 + \phi/R^2] \tag{4-8}$$

4.3.2 Material specification

The effectiveness of Eq. 4-8 is evaluated for both ITS and CTS. Torsional buckling is identified for experiments as the change in initial slope, for Stage-A to B, recall Figure 4-1. Figure 4-2 compares the resulting data. The correlation for ITS is nearly perfect; while for CTS, it is out by a factor of around 5. We suspect, the previous analysis for shallow shells should not apply to tapes curved transversely by π radians, which needs to be further addressed. The variance in data points may also be attributed to the difficulty in locating the switch between linear regimes in the experimental curves for CTS.

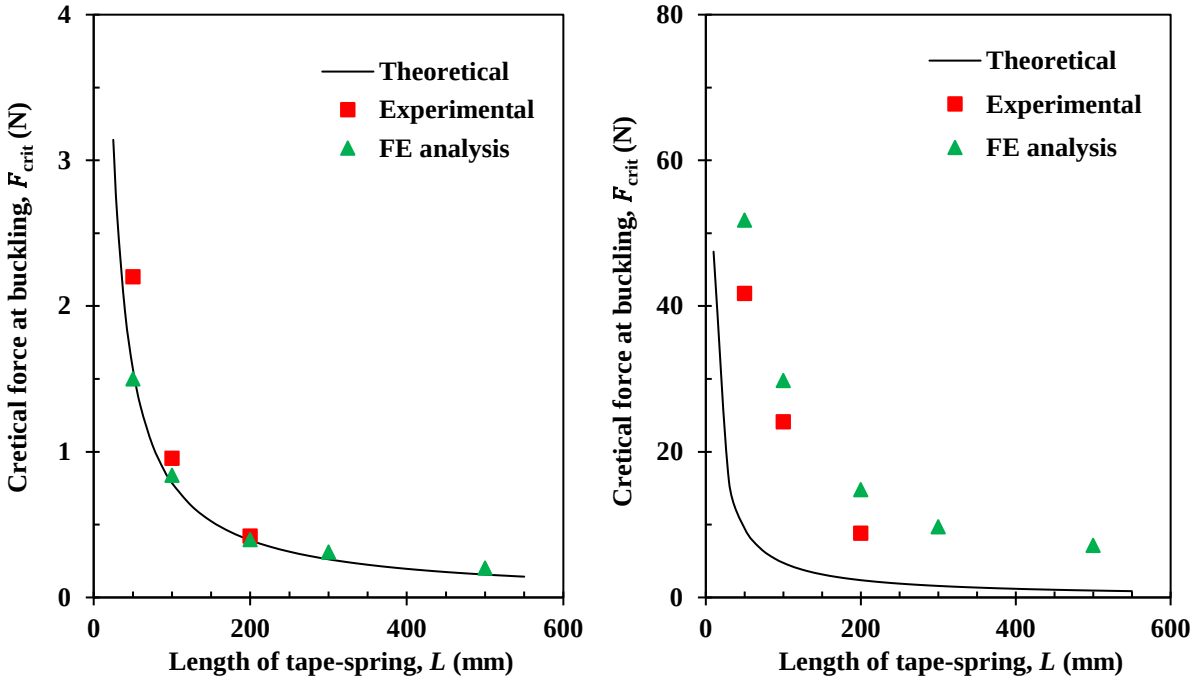

Figure 4-2 Critical force at torsional buckling, changing with tape length: (a) isotropic tape-spring; (b) composite tape-spring. Theoretical curves are fitted using Eq. 4-8.

4.4 LARGE DISPLACEMENT FOLD GEOMETRY

We now consider the large displacement untwisted folding of a tape-spring during Stage-D in Figure 4-1. For uniform bending, it is usual to assume that any changes in strain energy in a folded tape-spring are due to the fold alone and not to the ploy regions, which maintain a fixed

shape. Because the shape of fold has changed from one type of open cylinder to another, there is only developable bending deformation and negligible stretching [80].

The change in axial curvature, χ_x, is $1/r$, where r is the unknown uniform radius of the central fold: there is no twisting curvature, and $\chi_y = \pm 1/R$, where R is the original transverse radius of curvature: the $\pm$ sign accords opposite/equal-sense bending, respectively. The total strain energy in bending, $\bar{U}_B$, multiplies the energy density by the surface area of fold:

$$\bar{U}_B = 2r\psi b \cdot \frac{D}{2}\left[\chi_x^2 + \beta\chi_y^2 + 2\nu\chi_x\chi_y\right] = Db\psi\left[\frac{1}{r} + \frac{\beta}{R^2} \mp \frac{2\nu}{R}\right] \tag{4-9}$$

A minimal energy configuration sets $\partial\bar{U}_B/\partial r$ equal to zero, which returns $r = R/\sqrt{\beta}$ for bending in both directions [53].

Anywhere within the fold, the axial bending moment per unit width is M_x from Eq. 2-61. Multiplying by the flattened width b expresses the total moment, equal to the applied moment, $M_*^{\pm}$. Therefore:

$$M_*^{\pm} = \frac{bD}{R} \cdot \left(1 \pm \nu\sqrt{\beta}\right) \tag{4-10}$$

M_*^+ values from Eq. 4-10 are superposed onto the (M, θ) curves from FE analysis in Figure 4-3 over the same rotation range [53]. The correlation with Eq. 4-10 is very good throughout.

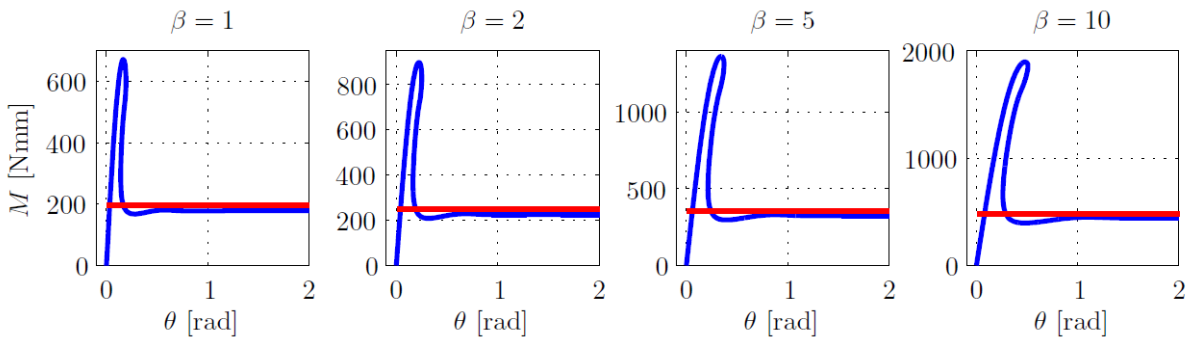

Figure 4-3 Opposite-sense orthotropic moment-rotation response from FE model. Red lines are constant M_*^+ prediction from Eq. 4-10.

4.5 CONCLUSIONS

We have developed a theoretical analysis for the folding observations from Section 3. The effects of geometrical non-linearity are considered with coupling between bending and stretching. We can predict the critical torsional buckling force for isotropic tape-springs, but not for composite tape-springs. When folded to a higher angle, a good correlation is obtained for orthotropic tapes.

Section 5

SHAPE OF PLOY REGION

5.1 INTRODUCTION

When designing the side-stay or link-stay hinge structures for aircraft landing gear, it is essential to understand the complete shape of folded tape-springs. As noted in earlier sections, we consider the folded shape to be defined by the uniform folded radius of curvature and the side ploy regions, whose length-wise boundary conditions must comply with the fold and the end casings. These ploy regions have a natural length scale of minimal deformation, L^*, just as the fold has radius r, see Figure 5-1. These lengths, however, may not be able to properly form if the connected tape is too short: it becomes over-confined and liable to damage during folding.

We have already calculated r for ITS and CTS structures, our aim now is to reliably calculate the natural ploy shape properties, and to compare them to experiments and FE simulation. A parametric study on the effects from initial geometry on the folded shape is also presented.

5.2 PLOY SHAPE – THEORY

The folded tape has three clear regions, which are shown for one half of a tape in Figure 5-1. The fold itself, Region-A, connects to the start of the ploy, Region-B, over which the change in transverse curvature decays before the undeformed straight end. At the connection between Region-A and B, $\kappa_x = 1/r$, $\kappa_y = 0$, which define the boundary conditions for the ploy shape.

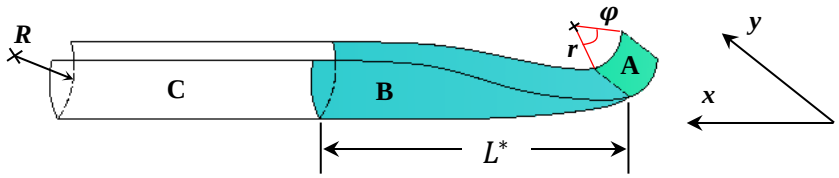

Figure 5-1 Schematic folded tape-spring: the shaded Region-B is the ploy region up to the start of the Region-A and the natural end Region-C. The length of the ploy region is L^* where the transverse curvature ranges from 0 to $1/R$.

The ploy region extends for a length many times larger than the shell thickness, *t*, and on the scale of the original transverse radius of curvature *R*. Such behaviour is purported to be a long-wave solution within the classical Donnell equations for deformation of an initially cylindrical shell [52]. The pair of variables in that case are the radial displacement, *w*, and the Airy Stress function, ϕ, tantamount to in-plane forces, which both vary in the *x* (axial) and *y* (circumferential) directions.

The cylindrical nature assumes a closed shell but our open cylindrical tape is governed equivalently. We reflect the same boundary conditions along its edges - as if having excised a strip from the original closed shell with no edge loading. The *w* and ϕ functions adopted in [52] both multiply an eigen function, $\sin(\pi y/b)$, by separate *x*-wise variations before being submitted to Donnell's equations: our strip conforms exactly to the required edge conditions if it has a transverse arc-length of *b*.

The long-wave solution is dominated by axial stretching and circumferential bending, which allows us to "switch off" certain parts within the Donnell set, as carefully laid out in [52]. The resulting pair of coupled differential equations in *w* and ϕ are simplified approximations of geometrical compatibility and equilibrium for bending and stretching together; similar forms have been obtained elsewhere, for example, when describing the "persistence" of end-wise pinching of an isotropic pipe [82]. If we repeat the long-wave derivation in [52], however, substituting for our orthotropic material laws from Section 2.2.3, we ultimately arrive at the equivalent pair of governing second-order differential equations:

$$\frac{\pi^4}{b^4}\cdot\phi-\frac{E}{R}\frac{d^2w}{dx^2}=0,\qquad D\beta\frac{\pi^4}{b^4}\cdot w+\frac{t}{R}\frac{d^2\phi}{dx^2}=0 \tag{5-1}$$

These differ from Donnell's original equations in two ways. The modular ratio, β, is now present and our ϕ is a stress function, differing from ϕ in [52], a force function, by a factor of thickness, *t*, which makes no difference to the outcome shortly. Substituting ϕ from the first equation into the second, and differentiating twice with respect to *x*, produces a fourth-order equation in *w* alone:

$$\frac{d^4w}{dx^4} + \frac{DR^2\beta\pi^8}{Etb^8} \cdot w = 0 \tag{5-2}$$

Writing the pre-factor of w as $4k^4$, we can establish a characteristic length scale, l, equal to π/k, from the general solution. Equating terms and re-arranging in terms of l, we arrive at [53]:

$$l = \frac{b^2}{\pi R^{1/2}} \cdot \left[\frac{4Et}{D\beta}\right]^{\frac{1}{4}} \quad \rightarrow \quad l = \frac{2}{\pi} \cdot \left[\frac{3(1-v^2/\beta)}{\beta}\right]^{1/4} \cdot \frac{b^2}{R^{1/2}t^{1/2}} \tag{5-3}$$

The particular boundary conditions at both ends of the ploy region ultimately dictate the numerical scale of this expression, making $2 \cdot 3^{\frac{1}{4}} .../\pi$ irrelevant for now. If $\beta >> v^2$, the essential dimensional variation of l goes with $b^2 \cdot R^{1/2} \cdot t^{1/2} \cdot \beta^{-1/4}$. For a fixed width and material, $l \sim 1/\sqrt{Rt}$, which is precisely the inverse relationship observed when dealing with "short-wave" solutions, *i.e.* boundary layer effects of Donnell's equations. We can of course shorten the expression by writing b as a proportion of R, setting $l \sim R^{3/2} \cdot t^{1/2} \cdot \beta^{-1/4}$, as in [82], giving fewer parameters to vary when characterising l experimentally.

The numerical pre-factor in Eq. 5-3 has a value close to unity, around 0.8 for $v = 0.3$ and $\beta = 1$. From finite element simulations shown momentarily, this tends to overshoot by some way. As ever, assuming that certain kinematic terms are dominant in Donnell's equations subtracts from the general application of the long-wave result; that the ploy length is somewhere between long and short.

A more general and direct analysis was originally produced by Jain and Rimrott in 1971 on the closely related subject of STEMS—Storable Tubular Extendable Members [83]. These are metal tape-spring slit tubes enveloping nearly 2π radians of cross-section, capable of being wound onto a drum and then deployed on a spacecraft for gravity compensation, instrument positioning etc. From the outset, they deal with changes of curvatures, χ, in the ploy region, assuming that one end has been completely flattened, the other being fully rounded and unstressed, *i.e.* ploy Region-B in Figure 5-1. Transverse moment equilibrium is simplified crucially by assuming that the double rate of change of transverse curvature along the STEM, $\partial^2\chi_y/\partial x^2$ dominates, as per Donnell; but that the equivalent rate for the change in curvature

along, $\partial^2\chi_x/\partial x^2$, is some fixed proportion, a, of the principal rate. Employing the Codazzi-Mainardi compatibility equations, they arrive at a final governing equation for χ_y:

$$\frac{\partial^2\chi_y}{\partial x^2} + k^2\frac{\partial^2\chi_y}{\partial y^2} = 0 \tag{5-4}$$

where $k = \sqrt{1+a}$ and ultimately is a decay parameter.

Jain and Rimrott [83] employ a Fourier series solution for χ_y, which sums to a uniform $-1/R$ at the flat end, and to zero at *x* equal to "infinity", for simplicity: only opposite sense flattening is dealt with but the result can be extended easily for $\chi_y = +1/R$ at $x = 0$. They are then able to find the corresponding changes in transverse curvature, χ_x, and twisting curvature, χ_{xy}.

If instead we take a leading order solution for χ_y, equal to $f(x)\cos\pi y/b$ and substitute into Eq. 5-4, then [53]:

$$\frac{d^2f}{dx^2} - \frac{k^2\pi^2}{b^2}f = 0 \;\rightarrow\; \chi_y = -\frac{1}{R}\cdot\exp\left(-\frac{k\pi x}{b}\right)\cos(\pi y/b) \tag{5-5}$$

which complies with the earlier boundary conditions. The other changes in curvature follow from the Codazzi-Mainardi equations again, with

$$\chi_{xy} = \frac{k}{R}\cdot\exp\left(-\frac{k\pi x}{b}\right)\sin(\pi y/b) \tag{5-6}$$

$$\chi_x = -\frac{k^2}{R}\cdot\exp\left(-\frac{k\pi x}{b}\right)[1-\cos(\pi y/b)] \tag{5-7}$$

Jain and Rimrott acknowledge that because the bending solution foists a change in Gaussian curvature, there is also in-plane stretching primarily along the ploy length, again, in the same direction in Donnell's cylinders.

The expression for the former in terms of curvature changes (rather than absolute terms, Eq. 4.1) is shown to be $-\chi_{xy}^2 + \chi_x\chi_y + \chi_x/R$ in [83]. Considering Eqs. 5-5 to 5-7, the order in

size of contributions from all changes in curvature are the same, and all must be included in the relationship to $\partial^2\epsilon_x/\partial y^2$. We may therefore write, substitute and calculate:

$$\frac{\partial^2\epsilon}{\partial y^2} = \chi_{xy}^2 - \chi_x\chi_y - \chi_x/R = \frac{k^2}{R^2}\left[\exp\left(-\frac{k\pi x}{b}\right) + \exp\left(-\frac{2k\pi x}{b}\right)\right]\cdot[1-\cos(\pi y/b)] \tag{5-8}$$

This expression is then integrated twice with respect to *y* to give the strain and thence axial stress. The constants of integration follow from setting the nett axial force to be zero, i.e. $\int \epsilon_x dy = 0$ between limits of $\pm b/2$. For our solution, it can be shown:

$$\epsilon_x = \frac{k^2}{R^2}\cdot\left[\exp\left(-\frac{k\pi x}{b}\right) + \exp\left(-\frac{2k\pi x}{b}\right)\right]\cdot\left[\frac{y^2}{2} + \frac{b^2}{\pi}\cdot\cos\left(\frac{\pi y}{b}\right) - \frac{b^2}{24} + \frac{2b^2}{\pi^3}\right] \tag{5-9}$$

To find *k*, the usual strain energy components from bending and stretching are assembled. In the case of bending (Eq. 2-62), the dominant product term is χ_y^2, which varies with $1/R^2$; for the others, $(\chi_{xy}^2, \chi_x\chi_y)\sim k^2R^2$ and $\chi_x^2\sim k^4R^2$, which are much smaller because *k* is usually less than unity. The finial total energy expression is thus [53]:

$$\bar{U} = \bar{U}_B + \bar{U}_s = \int\int U_B + U_S\, dxdy = \int_{-b/2}^{b/2}\int_0^{\inf}\frac{1}{2}\left(D\beta\chi_y^2 + Et\epsilon_x^2\right)dxdy \tag{5-10}$$

Substituting for χ_y and ϵ_x, and performing the integration, we arrive at:

$$\bar{U}_B = B\cdot\frac{D\beta b^2}{R^2k}, \qquad \bar{U}_s = S\cdot\frac{Etb^6k^3}{R^4} \tag{5-11}$$

where *B* is a constant equal to $1/8\pi \approx 0.039$, and $S = 9.18\times10^{-6}$. The proper value of *k* minimises $\bar{U}$ by differentiating with respect to *k* and setting equal to zero, i.e.

$$k^4 = \frac{B}{3S}\cdot\frac{D\beta}{E}\cdot\frac{R^2}{tb^4} \;\rightarrow\; k^4 = \frac{B}{36S}\cdot\frac{\beta}{1-v^2/\beta}\cdot\frac{t^2R^2}{b^4} \tag{5-12}$$

Returning to Eq. 5-5, the characteristic length of decay and thus ploy length, L^* from the ploy Region-B, is set by the index of the exponent. To compare directly with Donnell's solution, Eq. 5-3, we set $L^* = b/\pi k$ to give [53]:

$$L^* = \frac{b^2}{\pi}\left[\frac{1-\nu^2/\beta}{120\beta}\right]^{1/4}\sqrt{c/t} \tag{5-13}$$

For $\nu = 0.3$ and $\beta = 1$, the numerical pre-factor is around 0.093: this is considerably smaller than the prediction from Eq. 5-3, because all curvature terms now contribute to the level of Gaussian curvature. But it seems self-defeating to declare a specific ploy length in view of the decaying nature of the problem; an index equal to -1 lends a reduction in parameter values of only 63%. We can, of course, compare different predictions of L^* for the same measure, but it is better to compare the decaying variation due to *k* originally. Comfortingly, there is the same long-wave dependency of L^* on $b^2 \cdot R^{-1/2} \cdot t^{-1/2} \cdot \beta^{-1/4}$ as in *l* from Donnell.

5.3 PLOY SHAPE – CHARACTERISATION

5.3.1 Tape shape in folding

Figure 5-2 shows the curvature changes on nodes along the central line of the folded shape with a folded angle of around 90˚. There is a transition point T, which indicates the onset of exponential decay in χ_y, and is well-fitted by Eq. 5-5 when the decay parameter $k = 0.62$. In this region, χ_x and χ_{xy} are also close to zero, which correlates with our assumption for Eqs. 5-6 and 5-7 in the ploy Region-B. The fitting-curve is extended to $\chi_y = 1/R$, *i.e.* point N where $\chi_y = 1/R$, as indicated by the dashed line in Figure 5-2, which defines the theoretical boundary. Any differences between the theoretical analysis and real shape is considered to be minor compared to the complexity it would bring mathematically. The ploy length, L^*, is therefore characterised as the distance between points N and P. Consider the tape shape with χ_y less than 5% of the value of κ_{y0}, as in the natural Region-C: the ploy length $L^* = L_P - L_N$ is found to be 57 mm in this case. This correlates well with the prediction from Eq. 5-13 which gives the

value of 53.7 mm. Further studies on what dominates the shape of a CTS ploy region are now investigated using theory and FE analysis.

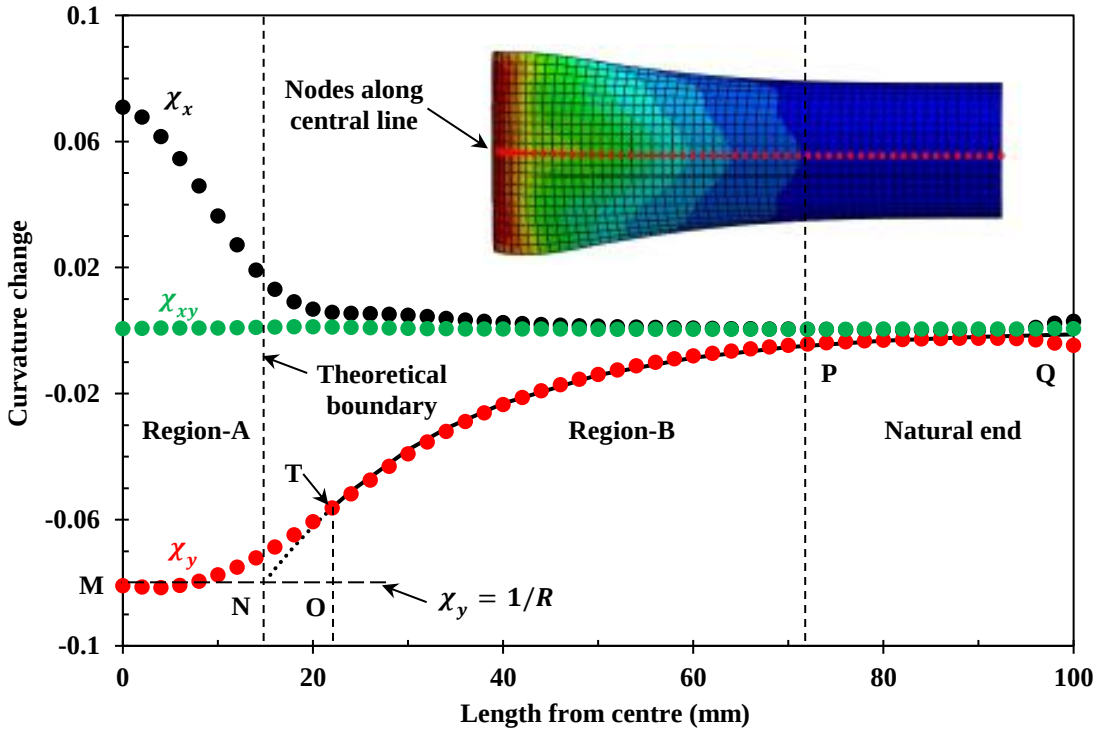

Figure 5-2 Curvature changes on nodes along central line of a folded tape. Solid curve is fitted by Eq. 5-5; dashed line shows an extension of exponential decay.

5.3.2 Folded tape shape

The folded ploy shape of a CTS is recorded using a zSnapper® vario 3D laser scanner shown schematically in Figure 5-3, with a resolution of 100 μm [84]. The laser projector emits stripes of laser light onto an object, which are deformed by its shape and captured by the camera. Calibration is made by measuring a calibration gauge (with reference points) in different positions using SnapCal software. The calibration data are imported into SingleZsn software, where all sample scans were recorded and constructed into a discrete point cloud [84]. All scans had a resolution of 640 × 480 pixels.

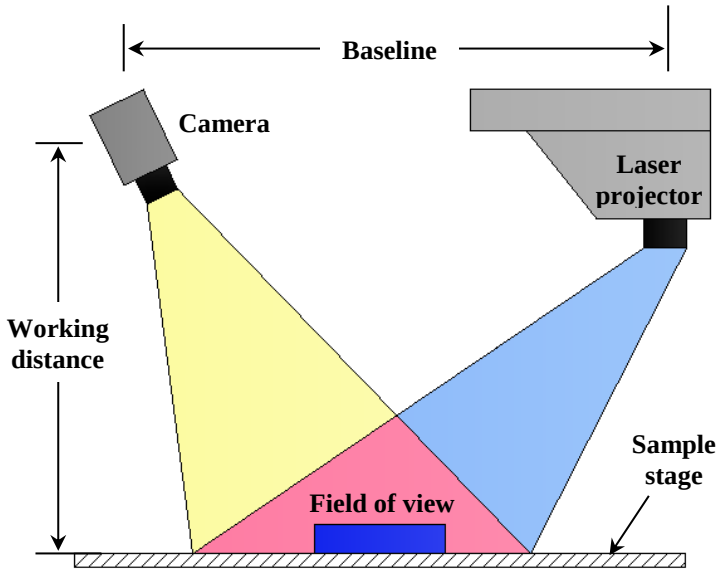

Figure 5-3 Schematic representation of 3D laser scanning setup.

The shape of a CTS with *L*=200 mm, folded to 180˚, is characterised by the 3D laser scanning and an FE analysis. It is noted that the quality of data near the sample edge are quite poor. The region of interest however are the ploy region of the folded circular Region-A and the onset of ploy Region-B from Figure 5-1.

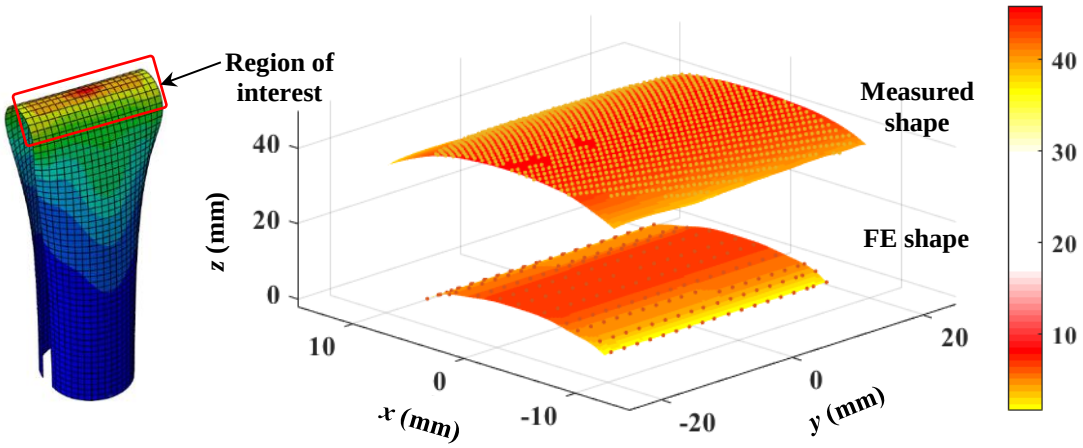

Figure 5-4 Comparison of the folded tape shape in the central fold region. Initial geometry of the CTS tape is 200 length and 180˚ subtended angle.

The scanned data were reconstructed using MATLAB [85]. Figure 5-4 compares the measured shape with the FE model in Region-A, with *x* values bounded between ± 8 mm, as discussed in Section 3.4.4 (Figure 3-19). In this region, the measured shape gives $\kappa_y = 0.00036$ mm^{-1}, with $\kappa_x = 0.054$ mm^{-1}. This indicates that it is slightly curved in transverse direction. The FE shape

provides $\kappa_y = 0.00039$ mm^{-1}, while $\kappa_x = 0.12$ mm^{-1}. The difference in the longitudinal direction can be attributed to the applied boundary conditions since the central fold region is quite sensitive to them [20]: to facilitate the 3D scanning, the two ends of the real tape sample is bonded together transversely, while for the FE shape, the whole model is constrained longitudinally.

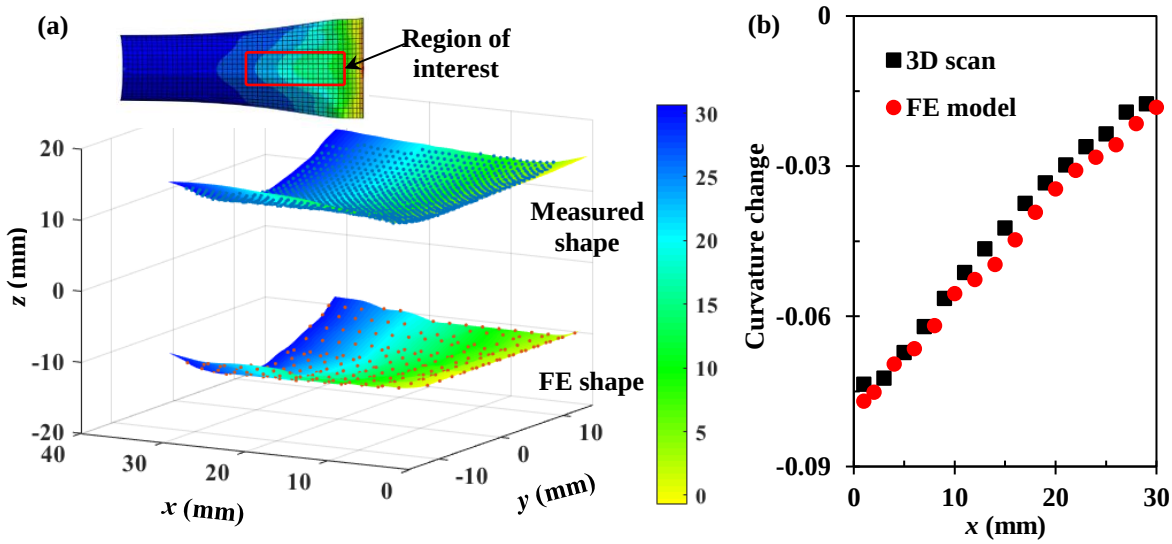

Figure 5-5 Comparison of (a) the folded tape shape in the ploy Region-B and (b) the transverse curvature change values through the region.

Figure 5-5-a shows the shapes in the ploy Region-B. The slight undulations in the FE shape are due to the relatively large element size compared to the resolution of the laser scanning system. The transverse curvature is calculated through the scanned region, and compared to the values from the FE shape in Figure 5-5-b, which shows good agreement. Therefore, the parametric study is focused on the ploy Region-B.

5.3.3 Parametric study

A parametric study on the governing factors of the folded tape shape is performed using the FE model alone. The ploy shape of the folded tape can still be characterised by the exponential decay (Eq. 5-12) even though it is formed by bending the entire strip and not flattening one end.

Figure 5-6 shows the decay parameter k (Eq. 5-12) and ploy length L^* (Eq. 5-13) as a function of sample width, initial radius, and thickness, separately: for each variable, the other parameters

are kept constant. With increasing width and radius, the value of k decreases, which implies that the ploy region B becomes longer. Increasing the thickness, the growth in k is accompanied by a reduction in L^*.

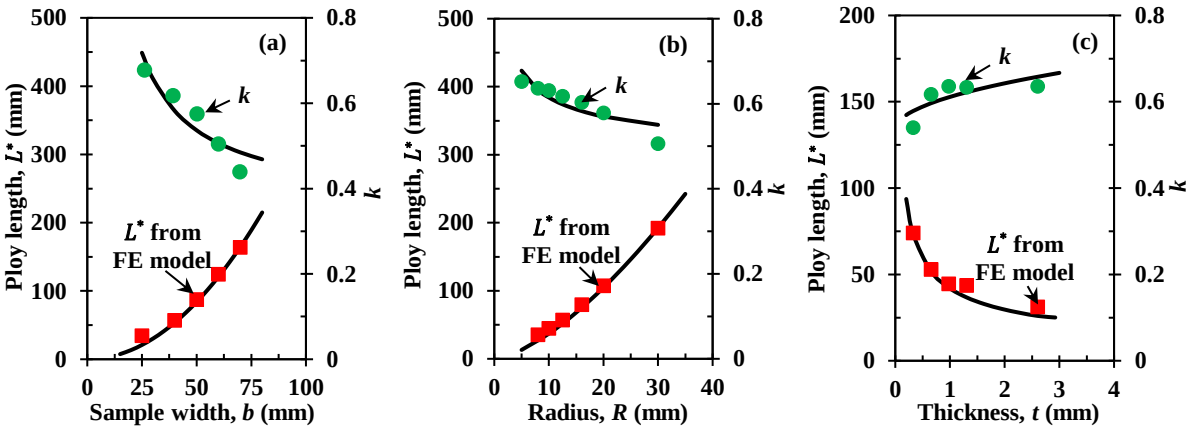

Figure 5-6 Effect of (a) sample width, (b) initial radius and (c) thickness on decay parameter, k, and ploy length, L^*.

Instead of $k \sim 1/b$ from Eq. 5-12, the fitting curve is adopted with $k = 2.49b^{-0.4}$. Equation 5-12 for b is also limited for predicting the effects of both R and t: in terms of $k \sim \sqrt{1/R}$ and $k \sim \sqrt{t}$, the fitting curves are implemented with $k = 0.82R^{-0.12}$ and $k = 0.62t^{0.07}$, respectively. This may suggest that the absolute value of k is very sensitive to the boundary conditions, and further study is needed.

In terms of ploy length (Eq. 5-13), the analytical model provides more effective predictions. In Figure 5-6-a and b, data points were extracted from the FE model by considering the χ_y value at point P (Figure 5-2) to be within ~5% of the original curvature; while for Figure 5-6-c, the analytical model is based on the thin-shell theory (typically $t/R < 1/20$ [73]). Its effectiveness reduces with increasing tape thickness and $\chi_y < 1/10R$ is adopted for $t \leq 1.3$ mm, with χ_y as 20% of the original curvature with $t = 2.6$ mm.

5.4 CONCLUSIONS

We have characterised the shape of folded tape-springs using compact but effective models. It is clear that the shape of the fold itself is developable; the ploy region is not but axial strains and transverse curvature changes are dominant. It is also clear that there are shortfalls in our models for different, possibly attractive combinations of geometry and material for alternative composite tape-springs. Rather than exclude these because we cannot predict their folded shapes accurately, we will re-explore our modelling assumptions and devise new insight. We must also return to the question of how these shapes are affected by the tape-spring being already bistable—which we have excluded here.

We have highlighted the more interesting shape parameters of our folded tapes, such as the exponential decay and ploy length in the ploy region. These govern the ability of the tape to be folded and stowed, as well as provide essential guidance to the design and implementation of bistable composite tubes. The tape will also have to bear compression when straight as part of its landing gear function. We will therefore be returning to "standard" structural testing of axially loaded, orthotropic thin-walled open tubes.

REFERENCES

[1] Lachenal X, Daynes S, Weaver PM. Review of morphing concepts and materials for wind turbine blade applications. Wind Energy 2013;16:283–307.

[2] Hull D, Clyne TW. An introduction to composite materials. Cambridge university press; 1996.

[3] Emam SA, Inman DJ. A Review on Bistable Composite Laminates for Morphing and Energy Harvesting. Appl Mech Rev 2015;67:60803–15.

[4] Sofla AYN, Meguid SA, Tan KT, Yeo WK. Shape morphing of aircraft wing: Status and challenges. Mater Des 2010;31:1284–92.

[5] Barbarino S, Bilgen O, Ajaj RM, Friswell MI, Inman DJ. A Review of Morphing Aircraft. J Intell Mater Syst Struct 2011;22:823–77.

[6] Daynes S, Weaver PM. Review of shape-morphing automobile structures: concepts and outlook. Proc Inst Mech Eng Part D J Automob Eng 2013;227:1603–22.

[7] Schmidt RK. Aircraft landing gear assembly. EP3069991B1, 2017.

[8] Hyer MW. Calculations of the Room-Temperature Shapes of Unsymmetric Laminates. J Compos Mater 1981;15:296–310.

[9] Lee AJ, Moosavian A, Inman DJ. A piezoelectrically generated bistable laminate for morphing. Mater Lett 2017;190:123–6.

[10] Daynes S, Potter KD, Weaver PM. Bistable prestressed buckled laminates. Compos Sci Technol 2008;68:3431–7.

[11] Wang B, Fancey KS. A bistable morphing composite using viscoelastically generated prestress. Mater Lett 2015;158:108–10.

[12] Guest SD, Pellegrino S. Analytical models for bistable cylindrical shells. Proc R Soc A Math Phys Eng Sci 2006;462:839–54.

[13] Dano M-L, Hyer MW. Thermally-induced deformation behavior of unsymmetric laminates. Int J Solids Struct 1998;35:2101–20.

[14] Chillara VSC, Dapino MJ. Stability considerations and actuation requirements in bistable laminated composites. Compos Struct 2018;184:1062–70.

[15] Daton-Lovett A. An extendible member. PCT/GB97/00839, 1996.

[16] Iqbal K, Pellegrino S. Bi-stable composite shells. Proceeding 41st AIAA/ASME/ASCE/AHS/ASC Struct. Struct. Dyn. Mater. Conf. Exhib., Atlanta: 2000, p. 1–8.

[17] Galletly DA, Guest SD. Bistable composite slit tubes. I. A beam model. Int J Solids Struct 2004;41:4517–33.

[18] Galletly DA, Guest SD. Bistable composite slit tubes. II. A shell model. Int J Solids Struct 2004;41:4503–16.

[19] Yee JCH, Soykasap O, Pellegrino S. Carbon Fibre Reinforced Plastic Tape Springs. 45th AIAA/ASME/ASCE/AHS/ASC Struct. Struct. Dyn. Mater. Conf., American Institute of Aeronautics and Astronautics; 2004.

[20] Seffen KA. On the Behavior of Folded Tape-Springs. J Appl Mech 2001;68:369–75.

[21] Yee JCH, Pellegrino S. Folding of woven composite structures. Compos Part A Appl Sci Manuf 2005;36:273–8.

[22] Yee JC, Pellegrino S. Composite tube hinges. J Aerosp Eng 2005;18:224–31.

[23] Mallikarachchi HMYC, Pellegrino S. Quasi-Static Folding and Deployment of Ultrathin Composite Tape-Spring Hinges. J Spacecr Rockets 2011;48:187–98.

[24] Murphey T, Jeon S, Biskner A, Sanford G. Deployable booms and antennas using bi-stable tape-springs. 24th Annu. AIAA/USU Conf. Small Satell., 2010, p. 1–7.

[25] Xiong C, Lei Y, Yao X. Dynamic Experimental Study of Deployable Composite Structure. Appl Compos Mater 2011;18:439–48.

[26] Costantine J, Tawk Y, Christodoulou CG, Banik J, Lane S. CubeSat Deployable Antenna Using Bistable Composite Tape-Springs. IEEE Antennas Wirel Propag Lett 2012;11:285–8.

[27] Wu C, Viquerat A. Natural frequency optimization of braided bistable carbon/epoxy tubes: Analysis of braid angles and stacking sequences. Compos Struct 2017;159:528–37.

[28] Mao H, Luigi GP, Michele G, Nickolay I, Gunnar T. Deployment of Bistable Self-Deployable Tape Spring Booms Using a Gravity Offloading System. J Aerosp Eng 2017;30:4017007.

[29] Kwok K, Pellegrino S. Shape Recovery of Viscoelastic Deployable Structures. 51st AIAA/ASME/ASCE/AHS/ASC Struct. Struct. Dyn. Mater. Conf., American Institute of Aeronautics and Astronautics; 2010.

[30] Brinkmeyer A, Pellegrino S, Weaver PM. Effects of long-term stowage on the

deployment of bistable tape springs. J Appl Mech 2016;83:11008.

[31] Kwok K, Pellegrino S. Micromechanics Models for Viscoelastic Plain-Weave Composite Tape Springs. AIAA J 2017;55:309–21.

[32] Khan AI, Borowski EC, Soliman EM, Reda Taha MM. Examining Energy Dissipation of Deployable Aerospace Composites Using Matrix Viscoelasticity. J Aerosp Eng 2017;30:4017040.

[33] Borowski EC, Soliman EM, Khan AI, Taha MMR. Stowage and Deployment of a Viscoelastic Orthotropic Carbon-Fiber Composite Tape Spring. J Spacecr Rockets 2018;55:829–40.

[34] Kwok K, Pellegrino S. Micromechanics Models for Viscoelastic Plain-Weave Composite Tape Springs. AIAA J 2017;55:309–21.

[35] Murphey T, Pellegrino S. A Novel Actuated Composite Tape-Spring for Deployable Structures. 45th AIAA/ASME/ASCE/AHS/ASC Struct. Struct. Dyn. Mater. Conf., American Institute of Aeronautics and Astronautics; 2004, p. 1–11.

[36] Schultz MR, Hulse MJ, Keller PN, Turse D. Neutrally stable behavior in fiber-reinforced composite tape springs. Compos Part A Appl Sci Manuf 2008;39:1012–7.

[37] Rimrott FPJ. Storable tubular extendible member: a unique machine element. Mach Des 1965;37:156–65.

[38] Prigent Y, Mallol P, Tibert G. A classical lamination model of bi-stable woven composite tape-springs. In: Kouhia JF and R, editor. Proceeding 24th Nord. Semin. Comput. Mech., Mechanics, School of Engineering Sciences (SCI), KTH: Department of Civil and Structural Engineering, Aalto University; 2011, p. 51–4.

[39] Mallol P, Mao H, Tibert G. Experiments and Simulations of the Deployment of a Bistable Composite Boom. J Spacecr Rockets 2017:1–11.

[40] Mao H, Shipsha A, Tibert G. Design and Analysis of Laminates for Self-Deployment of Viscoelastic Bistable Tape Springs After Long-Term Stowage. J Appl Mech 2017;84:71004–10.

[41] Hashin Z, Shtrikman S. A variational approach to the theory of the elastic behaviour of multiphase materials. J Mech Phys Solids 1963;11:127–40.

[42] Te Wu T. On the parametrization of the elastic moduli of two-phase materials. J Appl Mech 1965;32:211–4.

[43] Mansfield EH. On the elastic moduli of unidirectional fibre reinforced composites. London: 1976.

[44] Hashin Z. Analysis of composite materials - a survey. J Appl Mech 1983;50:481–505.

[45] Ravichandran KS. Elastic properties of two-phase composites. J Am Ceram Soc 1994;77:1178–84.

[46] Hill R. Elastic properties of reinforced solids: Some theoretical principles. J Mech Phys Solids 1963;11:357–72.

[47] Hyer MW. Stress analysis of fiber-reinforced composite materials. WCB/McGray-Hill Company; 1998.

[48] Jones RM. Mechanics of composite materials. 2 Edi. London: CRC Press; 1998.

[49] Naik NK, Shembekar PS. Elastic Behavior of Woven Fabric Composites: I—Lamina Analysis. J Compos Mater 1992;26:2196–225.

[50] Shembekar PS, Naik NK. Elastic Behavior of Woven Fabric Composites: II—Laminate Analysis. J Compos Mater 1992;26:2226–46.

[51] Lamers EAD, Wijskamp S, Akkerman R. Modelling the thermo-elastic properties of skewed woven fabric reinforced composites. 9th Eur. Conf. Compos. Mater. (ECCM 2000), 2000.

[52] Calladine CR. Theory of Shell Structures. Cambridge: Cambridge University Press; 1988.

[53] Seffen K, Wang B, Guest S. Folded Orthotropic Tape-Springs. J Mech Phys Solids 2019;123:138-48.

[54] Motra HB, Hildebrand J, Dimmig-Osburg A. Assessment of strain measurement techniques to characterise mechanical properties of structural steel. Eng Sci Technol an Int J 2014;17:260–9.

[55] Naik NK, Ganesh VK. An analytical method for plain weave fabric composites. Composites 1995;26:281–9.

[56] Tuttle ME, Brinson HF. Resistance-foil strain-gage technology as applied to composite materials. Exp Mech 1984;24:54–65.

[57] Jenkins CH. Manual on experimental methods for mechanical testing of composites. London: Fairmont Press Inc.; 1998.

[58] ASTM International. ASTM D3518 - Standard test method for in-plane shear response of polymer matrix composite materials by tensile test of a ±45° Laminate. 2013.

[59] Measurements G. Errors Due to Misalignment of Strain Gages. Exp Tech 1982;6:16–9.

[60] MatWeb Materials Information Database. E-Glass Fiber, General 2017. http://www.matweb.com/ (accessed November 13, 2017).

[61] MatWeb Materials Information Database. Overview of materials for polypropylene 2017. http://www.matweb.com/ (accessed November 15, 2017).

[62] ASTM International. ASTM D3039 - Standard Test Method for Tensile Properties of Polymer Matrix Composite Materials. 2017.

[63] Wang B, Seffen KA, Guest SD. Folding of a bistable tape-spring structure based on plain-woven composite. 26th Int. Conf. Coposites/Nano Eng., Paris: 2018.

[64] Schindelin J, Arganda-Carreras I, Frise E, Kaynig V, Longair M, Pietzsch T, et al. Fiji: an open-source platform for biological-image analysis. Nat Methods 2012;9:676.

[65] Sherburn M, Brown L. TexGen open source project V3.10.0 2017. http://texgen.sourceforge.net/.

[66] Manders PW, Chou T-W. Enchancement of Strength in Composites Reinforced with Previously Stressed Fibers. J Compos Mater 1983;17:26–44.

[67] Seffen KA. Analysis of structures deployed by tape-springs. University of Cambridge, 1997.

[68] Abaqus User Manual. Abaqus theory guide. Version 6.14. Dassault Syst Simulia Corp 2014.

[69] Ansar M, Xinwei W, Chouwei Z. Modeling strategies of 3D woven composites: A review. Compos Struct 2011;93:1947–63.

[70] Starkova O, Yang J, Zhang Z. Application of time–stress superposition to nonlinear creep of polyamide 66 filled with nanoparticles of various sizes. Compos Sci Technol 2007;67:2691–8.

[71] Tscharnuter D, Jerabek M, Major Z, Pinter G. Uniaxial nonlinear viscoelastic viscoplastic modeling of polypropylene. Mech Time-Dependent Mater 2012;16:275–86.

[72] Dassault S. DraftSight: professional-grade, free CAD software. DraftSight 2017. https://www.3ds.com/products-services/draftsight-cad-software/.

[73] Qatu MS, Sullivan RW, Wang W. Recent research advances on the dynamic analysis of composite shells: 2000–2009. Compos Struct 2010;93:14–31.

[74] Ashby MF. Overview No. 92: Materials and shape. Acta Metall Mater 1991;39:1025–39.

[75] Rimrott FPJ. Two Secondary Effects in Bending of Slit Thin-Walled Tubes. J Appl Mech 1966;33:75–8.

[76] Mansfield EH. The Bending and Stretching of Plates. 2nd ed. Cambridge: Cambridge University Press; 1989.

[77] Mansfield EH. Large-deflexion torsion and flexure of initially curved strips. Proc R Soc London A Math Phys Sci 1973;334:279–98.

[78] Kyriakides S. Propagating Instabilities in Structures. Adv Appl Mech 1994;30:67–189.

[79] Giomi L, Mahadevan L. Multi-stability of free spontaneously curved anisotropic strips. Proc R Soc A Math Phys Eng Sci 2011.

[80] Calladine CR. The theory of thin shell structures 1888–1988. Proc Inst Mech Eng Part A Power Process Eng 1988;202:141–9.

[81] Seffen KA. "Morphing" bistable orthotropic elliptical shallow shells. Proc R Soc A Math Phys Eng Sci 2007;463:67 LP-83.

[82] Mahadevan L, Vaziri A, Das M. Persistence of a pinch in a pipe. EPL (Europhysics Lett 2007;77:40003.

[83] Jain VK, Rimrott FPJ. The ploy region of a slit tube. CASI Trans 1971;4:140–4.

[84] EOS Technologies Inc. zSnapper manual (v3.2). 2011.

[85] The MathWorks Inc. MATLAB Release R2017b. Natick, Massachusetts, United States: 2017.